Towards Nanoscale Torque Revolution

Towards Nanoscale Torque Revolution - Highly anisotropic synthetic antiferromagnetic nanoplatelets for torque-related applications

PROEFSCHRIFT

ter verkrijging van de graad van doctor aan de Technische Universiteit Eindhoven, op gezag van de rector magnificus prof.dr. S.K. Lenaerts, voor een commissie aangewezen door het College voor Promoties, in het openbaar te verdedigen op dinsdag 2 april 2024 om 11:00 uur

door

Jianing Li

geboren te Wuxi, China

Dit proefschrift is goedgekeurd door de promotoren en de samenstelling van de promotiecommissie is als volgt:

voorzitter:	Prof.Dr. C. Storm
1e promotor:	Dr.Ir. R. Lavrijsen
2e promotor:	Prof.Dr. B. Koopmans
leden:	Prof.Dr. P. Zijlstra
	Prof.Dr. M. del Puerto Morales (ICMM Madrid)
	Prof.Dr. M. Rivas Ardisana (Universidad de Oviedo)
adviseur:	Dr. M. Efremova

Het onderzoek of ontwerp dat in dit proefschrift wordt beschreven is uitgevoerd in overeenstemming met de TU/e Gedragscode Wetenschapsbeoefening.

Towards Nanoscale Torque Revolution - Highly anisotropic synthetic antiferromagnetic nanoplatelets for torque-related applications

Jianing Li

A catalogue record is available from the Eindhoven University of Technology Library

ISBN: 978-90-386-6007-3

The work described in this thesis has been carried out at the group Physics of Nanostructures at the Department of Applied Physics and Science Education of the Eindhoven University of Technology.

Contents

1

Introduction

Magnetic nanoparticles (MNPs) are extensively utilized in the field of biomedicine. While most research has concentrated on spherical MNPs, which have proven effective in various biomedical applications, it's important to recognize their limitations, especially when it comes to torque-related applications. This thesis shifts its focus to a new type of MNPs known as synthetic antiferromagnetic nanoplatelets (SAF NPs) with perpendicular magnetic anisotropy (PMA), referred to as p-SAF NPs. These unique nanoparticles are specifically tailored for torque-related applications. In this chapter, we delve into the historical context of MNPs and the advantages of p-SAF NPs. We also address recent advancements of MNPs and the ongoing challenges within the field of p-SAF NPs.

1.1 Magnetic particles in biomedicine

Magnetism has long been associated with medicine. From ancient times, humanity recognized that certain stones could attract other stones. The mysterious and invisible forces between these stones were revered by ancient civilizations, notably the Greeks, Romans, and Chinese, who documented the therapeutic use of these stones for various ailments and overall well-being[1,2]. These historical records fostered cultural beliefs in the healing powers of lodestones, which persisted for centuries. Even today, a myriad of health products utilizing the cultural belief of magnetism continues to emerge. However, until the 19th century magnetic therapy largely remained outside the mainstream scientific consensus and was often perceived as a placebo effect.

By the 19th century, scientific advancements, including Ampere's law, Maxwell's equations, and Faraday's Law, elucidated the principles of magnetism, enabling the creation of tools that produce magnetic fields. Still, magnetic treatments were predominantly viewed as "pseudo-science," with many regarding them as mere magical amulets.

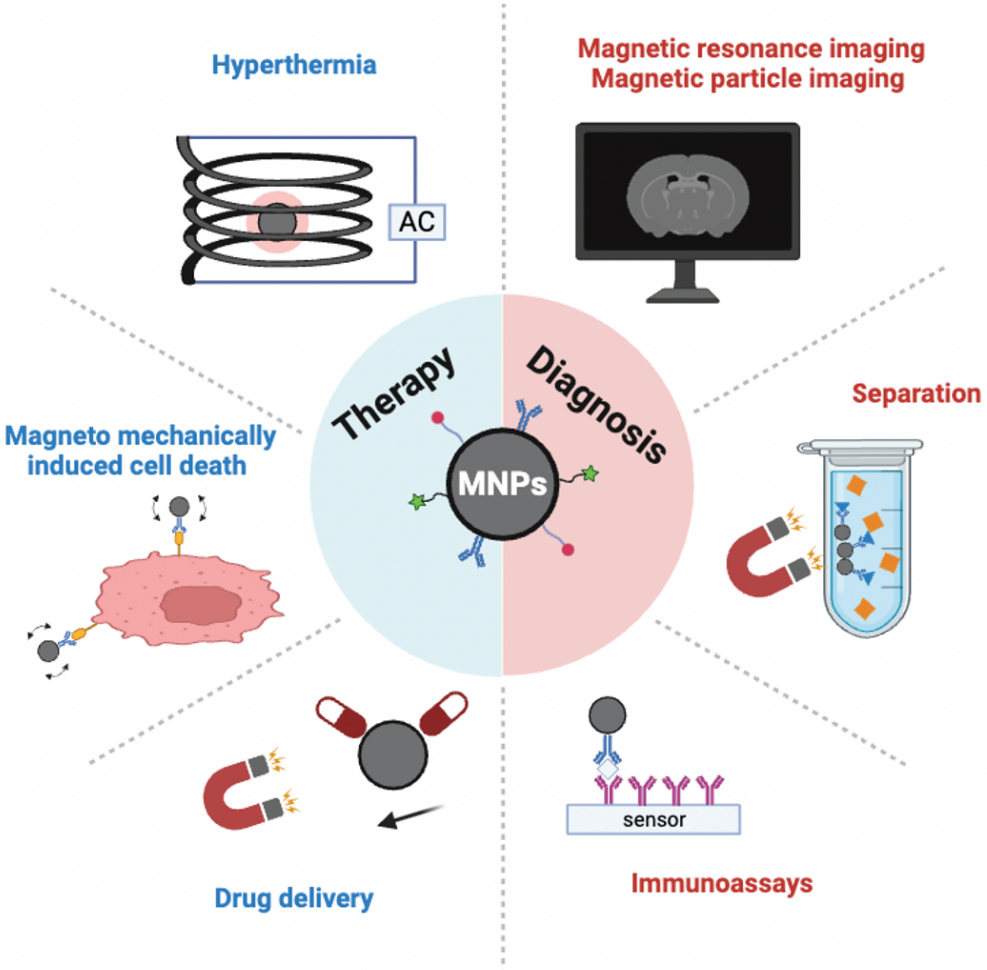

Figure 1.1: Diagram illustrating the utilization of magnetic particles. They can be categorized into two main groups: therapy (highlighted in blue) and diagnosis (highlighted in red).

A significant shift occurred in the late 19th century with the discovery of the heating effect of high-frequency electromagnetic fields[3]. This revelation set the stage for the development of magnetic hyperthermia treatments in the latter half of the 20th century[4]. These treatments employ AC magnetic fields to induce heat in magnetic particles, selectively targeting and damaging specific cells or tis-

sues. Concurrently, magnetic diagnostic techniques, such as magnetic resonance imaging (MRI), emerged in the late 20th century[5]. Integrating magnetism into both treatment and diagnostic procedures garnered increasing attention in modern medicine. Nevertheless, most of these applications remained elusive without advancements in nanotechnology.

In the 1980s, innovations in nanotechnology facilitated the synthesis and application of magnetic nanoparticles (MNPs), the size of which is below a hundred nanometers. This opened the possibility for a wider set of potential medical applications[6]. With appropriate surface functionalization, MNPs can bind to biomolecules, cells, and tissues, making these entities magnetically responsive and manipulable using external fields. By the 1990s, there had been an explosion of research seeking to develop diverse medical applications for MNPs in both diagnostics and therapy as shown in Fig. 1.1.

1.1.1 Magnetic particles

Let us first have a brief overview of the magnetic particles that are predominantly utilized in biomedical applications. Iron oxide nanoparticles, specifically Fe_3O_4 and Fe_2O_3, are the most commonly employed MNPs in biomedical fields, primarily due to the simplicity of synthesis and their biocompatibility[7,8]. The dimension of these iron oxide nanoparticles is intrinsically linked to their magnetic properties. This interdependence of size and magnetic behavior is depicted in Fig. 1.2a, illustrating both superparamagnetic and ferromagnetic (FM) states, which will be explained below, across varying nanoparticle diameters. Note that the relationship between size and magnetic properties is not limited to iron oxide nanoparticles. It is also applied to other MNPs. The hysteresis loops characterizing superparamagnetic and FM states are presented in Fig. 1.2(b-c). Within these loops, two parameters: coercivity (H_c) and remanence (M_r) are used to describe the loops. Specifically, H_c represents the propensity of a magnetic material to resist reversal of the magnetization. It is the field required to reduce the magnetization of a magnetic material to zero after being magnetized. M_r represents the residual magnetization in a material once an external field returns to zero from a saturated state.

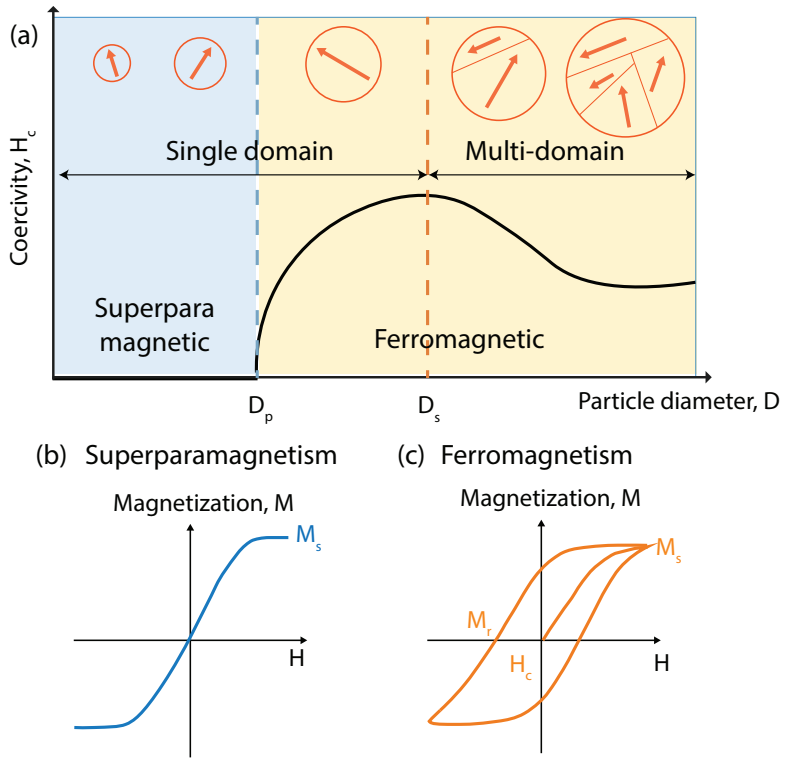

Figure 1.2: (a). Schematic diagram of the dependency of coercivity on the magnetic particle diameter. Typical hysteresis loop of (b) superparamagnetism and (c) ferromagnetism. Figure from[8].

When MNPs have a diameter less than D_p, the threshold diameter for the superparamagnetic state, they exhibit superparamagnetic characteristics. The H_c of these particles drops to zero, as shown in Fig. 1.2a. These particles do not exhibit magnetization without an external magnetic field at the timescale of seconds, and they can only be magnetized in the presence of an external magnetic field as illustrated in Fig. 1.2b. This superparamagnetic state materializes when thermal fluctuations supersede their inherent ferromagnetic tendencies. When the diameter surpasses D_p, MNPs transition to a FM state, characterized by non-zero values of both M_r and H_c, as displayed in Fig. 1.2c. When the diameter is larger than D_s, the critical diameter for a single domain state, MNPs evolve into a multi-domain state to reduce the overall energy.

Among the varied particle dimensions, superparamagnetic iron oxide nanoparticles (SPIONs) are preferred for biomedical applications. They have relatively small dimensions, typically on the order of tens of nanometers. Their zero M_r,

which prevents potential aggregation, makes them particularly advantageous for biomedical applications.

Given the strongly size dependent magnetic properties, achieving nanoparticles with consistent dimensions and shape becomes imperative to ensure uniform magnetic properties. Up to date, several popular methods including co-precipitation, microemulsion, thermal decomposition and so on have been reported for synthesis of MNPs with controllable shape and narrow size distribution[7,9,10].

1.1.2 Interactions between magnetic particles and magnetic field

The applications of MNPs are essentially based on the interactions between MNPs and magnetic fields, which can occur in various ways, as illustrated in Fig. 1.3. In this section, we discuss three distinct interaction mechanisms of MNPs with: an alternating current (AC) field, a gradient field, and a constant field, which generate heat, magnetic force, and magnetic torque respectively. We also explore how these interactions are utilized in applications.

Heat

One mechanism entails the utilization of an AC field, wherein MNPs harness energy from the field to generate heat (see Fig. 1.3a). This finds application in hyperthermia for cancer treatment (see Fig. 1.1), where localized heating of the MNPs raises temperatures to 42 - 44 °C, leading to cell destruction and tumor regression[11–15].

Magnetic force

Another significant application of MNPs involves mechanical movement, either through translational or rotational motion. The translational motion can be achieved by using a gradient field. As depicted in Fig. 1.3b, the gradient field exerts a force on the MNPs, causing them to move within a medium.

This control mode is commonly employed for the separation and concentration of

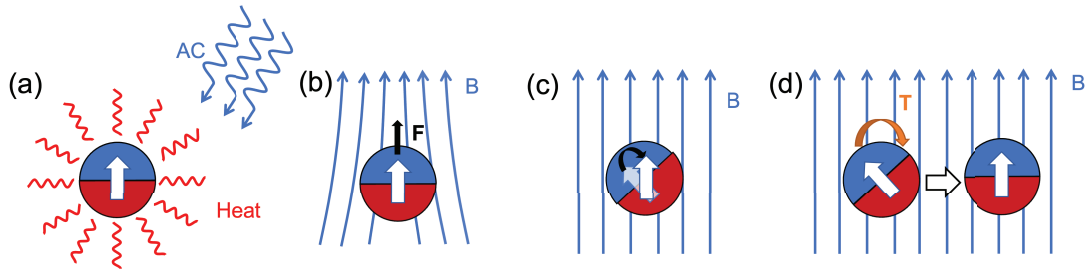

Figure 1.3: Different modes of interaction between MNPs and an external field: (a) MNPs under an AC field. MNPs absorb energy from the AC field and generate heat. (b) Under the gradient field, MNPs can feel a force that leads to translational movement. MNPs experience torque when the external field has an angle with the magnetization, leading to (c) magnetization rotation or (d) physical rotation of the MNPs to align with the external field. The white arrow represents the magnetization of the MNP. B is the magnetic field. T is the torque. F is the force.

targeted biomolecules, which is essential for quick and high-accuracy diagnosis. The targeted biomolecules are normally in a highly complex environment with the presence of multiple components, precise isolation of specific target biomolecules from raw samples prior to analysis is imperative. In this context, MNPs serve as markers, attached to targeted biomolecules such as cells, antibodies, proteins, nucleic acids, viruses, or bacteria. Subsequently, an external field is deployed to separate the targeted biomolecules from the unmarked ones[16–20]. Furthermore, this control mode exhibits potential in drug delivery, where MNPs, serving as vehicles, navigate drugs to disease sites subjected to substantial magnetic field gradients[21,22].

However, for clinical applications, a large gradient field is required, which, in turn, demands large magnets, efficient cooling systems for high fields, and increased costs. Moreover, the commonly used electromagnetic coils or permanent magnets only provide a gradient field to move the MNPs in one certain direction and can correspondingly create a gradient in the MNPs distribution. The precise control of MNPs to guide them to move in different directions into the targeted place requires a complex design of the gradient fields, which poses challenges, limiting their practical use[6].

Magnetic torque

An alternative approach involves employing torque rather than force, which inherently induces rotational motion. In this thesis, we target on torque-related applications, which utilize the rotational motion. When MNPs are exposed to an external field at an angle to their magnetization, magnetization alignment can occur through either Néel relaxation (involving intrinsic magnetization rotating to align with the external field without physical particle rotation) or Brownian relaxation (involving physical rotation of particles to align with the external field), as illustrated in Fig. 1.3(c-d). The magnetic torque that leads to alignment can be expressed as $\vec{\tau} = \mu_0 \vec{m} \times \vec{H}$, where H is the external magnetic field and m represents total magnetic moment. Notably, the torque is proportional to magnetic moment; thus, a greater magnetic moment yields a correspondingly larger torque.

Magnetic torque is not necessarily equal to mechanical torque. The type of rotation, whether magnetized rotation or physical rotation, to align with the external field depends on magnetic anisotropy. **Magnetic anisotropy** denotes the preferential direction in which magnetization aligns. Under high anisotropy, MNPs tend to physically rotate to align with the field. In contrast, lower anisotropy suggests a propensity for magnetization to self-rotate. For torque-related applications that employ physical rotation, high anisotropy is preferred to maximize mechanical torque transmission[23,24]. A more in-depth exploration of magnetic anisotropy is available in Section 1.2.1.

Compared to magnetic force, using torque can prevent the use of a complex magnetic field system. A uniformly rotating field is enough to control the MNPs instead of using gradient fields. The key of design is primarily on optimizing MNPs, such as enhancing their anisotropy, rather than on field generation.

Additionally, it is possible to transform the rotational motion of MNPs into translational motion through the strategic design of particles that disrupt symmetric hydrodynamic flows. For instance, attaching a rigid helical tail or a flexible flagellum to a magnetic core can induce directional movement under the influence of a rotating or oscillating field, as slender tails generate a net imbalance of drag along their lengths[25–29]. Employing nonspherical particles such as magnetic rods

or nanowires can lead to tumbling motion in the vicinity of a wall or surface under a rotating magnetic field[30,31].

There is growing interest in applications that exploit the rotational behavior itself, ranging from cancer treatment, which induces the magneto-mechanical destruction of cancer cells through MNPs[32,33], to magnetic tweezers capable of applying torques to individual molecules such as DNA, nucleic acid, and cells to characterize their mechanical properties[34–36]. Furthermore, the rotational behavior is becoming increasingly significant for lab-on-chip devices, enabling control over small volumes of liquid[37], facilitating fluid mixing[38], concentration detection[39,40] and biomarker detection[41]. These applications require the use of a rotating magnetic field to initiate rotation of individual MNPs or MNP assemblies.

To sum up, the growing attention in torque-related applications forms the basis of our thesis, which predominantly focuses on the rotational manipulation of magnetic particles. For such applications, high magnetic anisotropy and substantial total magnetic moment are essential for efficient torque transfer.

1.2 New type of particles for torque-related application

One pivotal challenge for torque-related applications is that the commonly utilized MNPs, such as SPIONs, are not explicitly designed for these specific applications. For these applications, it is vital to employ MNPs specifically designed with significant anisotropy and magnetic moment. This section will commence with an introduction to magnetic anisotropy, followed by a discussion on the fundamental requirements of MNPs for these applications. Subsequently, we will provide a concise overview of the current state of specially designed particles.

1.2.1 Magnetic anisotropy

As mentioned to previously, magnetic anisotropy denotes the preferential direction in which magnetization aligns. The magnetization tends to align in directions where the anisotropy energy reaches a minimum. Such directions are termed **easy axes**. Conversely, the directions that require more energy for magnetization alignment are termed **hard axes**. In general, the uniaxial anisotropy energy (E_k),

having only one preferred direction, can be expressed as:

$$E_k = K_1 \sin^2 \theta \tag{1.1}$$

where θ denotes the angle between magnetization and the anisotropy axis, and K_1 represents the anisotropy constant with unit Jm^{-3}. The origin of magnetic anisotropy can be traced back to two primary sources: crystal structure and shape[42].

Magnetocrystalline anisotropy

Magnetocrystalline anisotropy is an intrinsic property of crystalline ferromagnetic materials, which originates from the crystal structure. Note the magnitude and direction of magnetocrystalline anisotropy can vary greatly depending on the material and its crystal structure. For example, within a face-centered-cubic (fcc) structure, observed in materials like fcc-Co, the magnetic easy axis follow the <111> directions. On the other hand, in materials with a hexagonal-close-packed (hcp) crystal structure, typified by hcp-Co, the magnetic easy axis corresponds to the <0001> direction[43].

The underlying cause of magnetocrystalline anisotropy is the spin-orbit coupling. The electrostatic interaction between the electron orbitals and the potential created at the atomic site by the crystal stabilizes a specific orbital where the spin aligns favorably. Another contributor to this anisotropy is the dipole–dipole interaction[42].

Shape anisotropy

Distinct from the intrinsic properties described earlier, shape anisotropy depends on the shape of the sample. It derives from the demagnetizing field (H_d) within the material that is opposite to the magnetized direction, which is expressed through:

$$\vec{H}_d = -\mathcal{N}_d \vec{m}, \quad \mathcal{N}_d = \begin{bmatrix} N_{xx} & N_{xy} & N_{xz} \\ N_{yx} & N_{yy} & N_{yz} \\ N_{zx} & N_{zy} & N_{zz} \end{bmatrix} \tag{1.2}$$

Here, $\mathcal{N}_d$ represents the demagnetization tensor. For an ellipsoidal object, $\mathcal{N}_d$ can be described as a diagonal matrix with the demagnetization factors on the x, y, and z axis (N_x, N_y, and N_z) and $N_x + N_y + N_z = 1$. The magnetization tends to align in the direction with a lower demagnetizing field. In a spherical shape, the demagnetizing factors along all axes are equal, resulting in a net zero shape anisotropy. However, this is not the case for other structures, such as a long needle. In this structure, the demagnetizing factor along the needle is 0, and perpendicular to the needle it is 1/2. Shape anisotropy is induced along the needle. Further calculations of demagnetizing factors for different shapes are described in[42].

1.2.2 Basic requirements

Let us first discuss the drawbacks of the commonly used MNPs. SPIONs exhibit a superparamagnetic state and have zero anisotropy. Meanwhile, in order to maintain superparamagnetic state, the diameter of particles is limited, which results in a low total magnetic moment. These factors severely restrict their efficacy in mechanical torque transfer. Ferromagnetic iron oxide nanoparticles, on the other hand, have higher magnetic moment due to the larger size compared to SPIONs and exhibit magnetocrystalline anisotropy. However, their typically spherical shape results in zero shape anisotropy, leading to overall low anisotropy, which also limits torque transfer. Given these limitations, there is a clear need for specially designed MNPs. These MNPs should satisfy several key criteria:

- **Low remanence at zero field**: This characteristic is crucial to prevent the aggregation of MNPs in the absence of a magnetic field. Aggregation of MNPs inside the human body can lead to blood thrombosis, which must be avoided.

- **High total magnetic moment**: Both torque and force are directly proportional to magnetic moment. Higher magnetic moment results in a more robust response to magnetic fields and enables the application of greater torque.
- **Uniform magnetic properties among MNPs**: To ensure that particles respond uniformly to external magnetic fields, consistency in magnetic properties is essential. Various factors influence magnetic properties, with size and shape being prominent. Therefore, achieving uniform particle size and shape with minimal distribution is a requirement.
- **Biocompatibility**: MPNs need to be nontoxic to avoid damaging the attached biomolecules. This can be achieved either by ensuring that the MNPs themselves are biocompatible or by properly functionalizing the MNPs to prevent direct contact with biomolecules.
- **High magnetic anisotropy**: High anisotropy is beneficial for efficient mechanical torque transfer.

1.2.3 New types of particles

Considering these requirements, there is a compelling need for novel magnetic particles, particularly those exhibiting high anisotropy. Hence, we introduce synthetic antiferromagnetic (SAF) nanoplatelets (NPs) with perpendicular anisotropy (PMA), termed as p-SAF NPs. Before delving into our p-SAF NPs, let us briefly examine recent advancements in magnetic particles with high anisotropy.

Through the controlled modulation of surface energy and/or capping surfactants at specific temperatures during the wet chemical synthesis process, the morphology of MNPs can be tailored[44]. Various MNP shapes have been documented, including Fe_3O_4 nanowires[45–47], Fe_3O_4 and Ni nanorods[48,49], and Co and Ni nanoplatelets[50,51]. All of these configurations exhibit pronounced shape anisotropy. Additionally, methods based on aluminum oxide template-assisted deposition have been used to fabricate MNPs with great shape anisotropy, including Ni nanorods, Ni nanowires, Fe nanowires, NiFe nanodiscs, and nanorods[52–55]. These MNPs with anisotropy have been reported to induce cancer cell death through mechanical disruption

under low-frequency alternating magnetic fields[53–55]. Nevertheless, these MNPs still exhibit ferromagnetic properties that can lead to aggregation, necessitating stabilization methods to prevent agglomeration. Moreover, tuning the magnetic properties of these particles, especially shape anisotropy which is highly dependent on their shape, adds to the complexity of the synthesis.

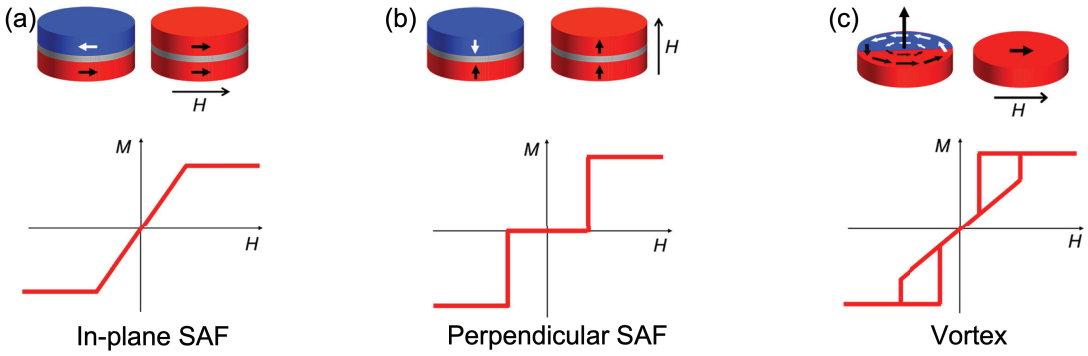

Figure 1.4: Three magnetic configurations of disc-shaped particles and their magnetization as a function of the applied magnetic field. (a) SAF with in-plane anisotropy (b) SAF with perpendicular (out-of-plane) anisotorpy. (c) Vortex disc. Taken from the paper[24].

With the development of microfabrication techniques, particularly lithography and sputtering[56], new avenues for physical fabrication methods to produce MNPs based on thin-film structures have emerged. In contrast to wet chemical synthesis methods, these particles exhibit narrower size distributions owing to precisely designed masks employed in lithography, offering the ability to fine-tune their shape and thickness. Among these, three types of magnetic discs/nanoplatelets have garnered attention for torque-related applications[23,57,58]: synthetic antiferromagnetic (SAF) discs with in-plane anisotropy (referred to as in-plane SAF)[59–61], SAF discs with perpendicular anisotropy (denoted as p-SAF and are the particles used in this thesis)[62–64], and permalloy vortex discs[65–67]. Figure 1.4 illustrates the magnetization configuration at zero field and in the saturation state, along with the hysteresis loops for these three nanodiscs.

The in-plane SAF discs consist of two FM layers separated by a nonmagnetic spacer layer, as depicted in Figure 1.4a. These two FM layers exhibit exchange coupling with opposite magnetization directions, effectively canceling each other and demonstrating antiferromagnetic behavior. This configuration results in what

is called "synthetic antiferromagnetic" behavior. Under an external magnetic field, the magnetic moments gradually align in the same direction until saturation. The p-SAF discs exhibit SAF properties similar to the in-plane SAF discs, but the magnetization is oriented perpendicular to the disc's plane, as shown in Fig. 1.4b. Vortex discs, illustrated in Fig. 1.4c, have magnetic moments primarily curled within the disc's plane to minimize magnetostatic energy. Only at the vortex's core do the magnetic moments project out of the plane, aligning perpendicularly. When an external field is applied, this perpendicular core migrates towards the disc's edge, culminating in the disc's saturation.

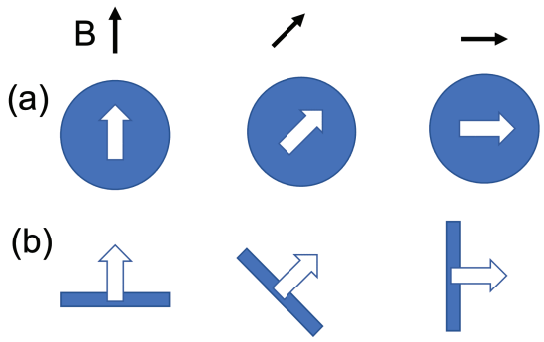

Figure 1.5: The orientation of (a) in-plane SAF and vortex discs exhibiting in-plane anisotropy, and (b) p-SAF discs which display out-of-plane anisotropy when under magnetic fields of varying directions.

All three types of particles exhibit zero remanence, thereby preventing aggregation. They can achieve higher magnetic moment compared to SPIONs, because their size is not constrained. While all three have higher anisotropy, either in-plane or out-of-plane, in comparison to SPIONs, p-SAF discs demonstrate superior torque transfer properties compared to the other two. This superiority arises from the easy-axis of p-SAF discs, which is perpendicular to the disc's plane. While for the other two types of discs, they have an easy-plane anisotropy, where the magnetization is aligned in the plane of the disc. As depicted in Fig. 1.5b, the disc's surface consistently aligns perpendicularly to the field direction, leading to a continuous torque. In contrast, as shown in Fig. 1.5a, the in-plane SAF and vortex discs, due to their intrinsic in-plane anisotropy, undergo magnetization rotation that does not generate additional torque once the disc's plane aligns with the rotation plane of the field[23,24]. Therefore, this thesis focuses on SAF structures with PMA, which can provide substantial anisotropy. In the following section, we provide a

brief introduction to p-SAF nanodiscs, also referred to as p-SAF nanoplatelets (NPs), and their challenges towards applications.

1.3 P-SAF nanoplatelets and their challenges

In this section, we will first introduce the fundamentals of the p-SAF stack and subsequently provide an overview of the current state of research in the field of SAF NPs. Lastly, we will discuss the challenges that p-SAF NPs face in their path towards application.

1.3.1 Basic p-SAF stack

The p-SAF system has been extensively researched and utilized in the field of spintronics, especially to enhance storage density, as its magnetization alignment can minimize the stray field of the device[68–70]. A typical p-SAF system is illustrated in Fig. 1.6a. Studies indicate that transition metals, such as Co, Fe, and Ni, when grown on heavy nonmagnetic metal layers like Pt, Pd, and Au, can exhibit PMA[71–73]. That is because at the interface, pronounced hybridization occurs between the 3d and 5d orbitals of the FM layer and heavy metal. This strengthens the spin-orbit interaction of the ferromagnet, leading to PMA[74–76]. The two FM layers are coupled by a spacer layer through the Ruderman-Kittel-Kasuya-Yosida (RKKY) interaction, ensuring their magnetization is antiparallel[77–79]. In this thesis we use a Ruthenium (Ru) space layer. A Ta seed layer is used to enhance the crystalline orientation of the subsequent layers grown on top of it[80].

A SAF stack with PMA presents an easy axis, oriented perpendicularly to the plane, and a hard plane parallel to the plane, as depicted in the insert of Fig. 1.6(b-c). Ideal hysteresis loops along the easy axis and hard plane are shown in Fig. 1.6(b-c). At zero field, when the field is aligned with the easy axis, the stack assumes an AF state, presenting zero net magnetization. As the field increases, the magnetization in one layer abruptly switches toward the field direction, leading to the saturation of the stack's magnetization. When the field decreases, the magnetization returns to the AF state. The opening in the hysteresis loop arises from the coercivity of the FM layer. Conversely, when the field is aligned with the

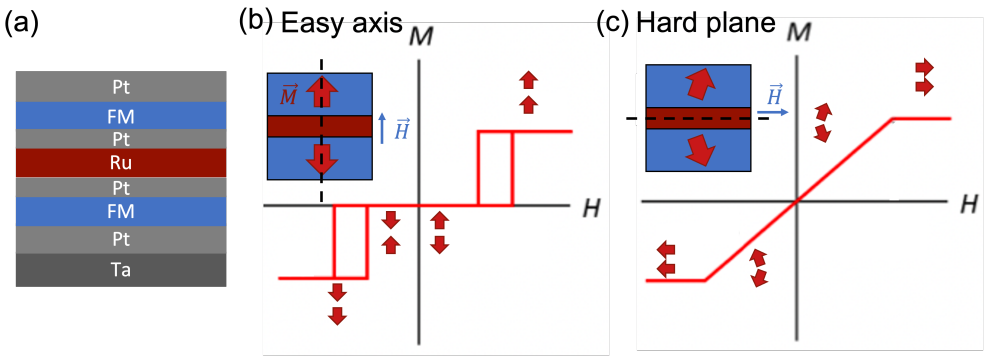

Figure 1.6: (a) The basic thin film stack of p-SAF system. The thickness of each layer is in nanometer. A typical hysteresis loop of p-SAF stack when the magnetic field is applied along (b) easy axis and (c) the hard plane. The inserts in (b) and (c) show the configuration of magnetization under magnetic field. The red arrows indicate the magnetization and the blue arrows indicate the magnetic field.

hard plane, a rising field induces the magnetization to tilt towards the external field. Due to RKKY coupling, the magnetizations of the two FM layers cancel with each other in the out-of-plane direction, maintaining a net component aligned with the hard plane. This leads to a gradual transformation of the magnetization, as illustrated in Fig. 1.6c. We are not the first to investigate SAF NPs, and in the following sections we introduce the progress of SAF NPs.

1.3.2 State of Art of SAF nanoplatelets

S. Wang *et al.* were the first to apply the in-plane SAF system to nanoparticles[59,60,81]. They successfully fabricated nanoparticles with a diameter of 120 nm using nanoimprint lithography, which were subsequently released into a solution. These particles comprised repeated stacks of Ta/Ru/CoFe/Ru/CoFe/Ru/Ta, exhibiting in-plane magnetic anisotropy. By adjusting the thickness of the stack, the susceptibility can be easily modulated, showing promise for multilevel separation[59]. They also showed that these in-plane SAF nanoparticles can be functionalized with silanes and protein[59,82]. Towards application, they have demonstrated the remarkable potential of these particles in separation processes of wastewater treatment[83].

In 2015, T. Vemulkar *et al.* first reported on 2 µm diameter microdiscs comprising

a p-SAF stack, fabricated through UV lithography[62]. They showed that the magnetic properties can be tuned through stack engineering and that the buffer Ta layer and Au underlayer have a drastic effect on the reversal properties of p-SAF stack[84]. Their findings revealed that SAF microdiscs can efficiently damage cancer cells when exposed to a low-frequency rotating field[23]. In such conditions, the microdiscs align with the field's rotation, exerting torque on the cell membrane. Additionally, the team conducted research on the alignment of these particles in a liquid environment under an external field[85], details of which will be elaborated upon in the subsequent Section 2.4.

In pursuit of SAF nanoparticles (NPs) of a smaller size, E. Welbourne *et al.* introduced a fabrication method based on nanosphere lithography, where polystyrene (PS) beads were used as masks for etching[64]. However, the size of the resultant particles is depended on the size of the PS beads, which can vary.

Further studies have explored methods to fine-tune the magnetic properties of such particles. For instance, utilizing multiple repetitions of FM/Pt has been proposed as a means to adjust the magnetic characteristics and boom the total magnetic moment[63]. In 2022, E. Welbourne *et al.* proposed a method to reduce the active field of SAF NPs by using a weaker RKKY coupling peak (second peak) rather than the stronger, first peak[86].

1.3.3 Challenges towards application

While p-SAF NPs exhibit promise for torque-related applications, several challenges remain unaddressed. These challenges encompass fabrication, magnetic properties, and characterization.

Fabrication. The first challenge involves the fabrication of p-SAF nanoparticles. Scaling up the production of these platelets to achieve uniform sizes at a low cost remains an unresolved issue. Optical lithography has been employed for fabricating micro-sized p-SAF NPs[62]. Spherical bead lithography has been utilized for both micro and nano-sized p-SAF NPs[61]. However, limitations persist in terms of throughput and size distribution. Innovative techniques for fabricating p-SAF NPs of varying sizes need to be devised and optimized. Furthermore,

their biocompatibility is also an issue, requiring appropriate functionalization to prevent direct contact with these potentially toxic nanoparticles. Although it is possible to cover these NPs with an Au surface, which is a well studied surface for functionalization in wet chemical synthesis[87], the process is still challenging due to differences between sputtered Au and the Au used in wet chemical synthesis. Regarding the challenge of fabrication, in Chapter 4, we propose a fabrication protocol of p-SAF NPs based on imprint lithography.

Magnetic properties. The second challenge revolves around understanding the magnetic properties of p-SAF NPs. After fabrication, these NPs often exhibit significantly increased coercivity fields[88], demanding substantial external fields for activation. Additionally, a distribution of switching fields emerges as the nanostructures form. The underlying physics is elaborated upon in Chapter 2. Tuning the magnetic properties, particularly to achieve lower activation fields, is crucial. Ensuring uniformity in the magnetic properties of p-SAF NPs from batch to batch is essential for achieving consistent magnetic responses. A more comprehensive understanding of their switching behavior and uniformity is required to customly engineered these p-SAF NPs. In Chapter 6, we investigate the effect of size on p-SAF NP's magnetic properties and show that inducing boron to FM layers is an efficient method to reduce the field to activate the NPs.

Characterization. Furthermore, characterizing particles batch by batch to assess uniformity, especially in the nanometer size range, is crucial. However, magnetic characterization of single MNPs at the nanometer scale is challenging. Complex techniques, such as differential phase contrast and electron holography in transmission electron microscopy[89,90], are required for characterizing these particles, which is often time-consuming and come with high costs. An easy and rapid method is needed to obtain the magnetic properties of these MNPs efficiently. To overcome the challenge, we present a solution for measuring individual p-SAF NPs using photothermal magnetic circular dichroism in Chapter 5.

Mechanical response. Lastly, it's important to note that magnetic torque does not directly equate to mechanical torque. As mentioned previously, when MNPs are introduced into a complex liquid system and are free to rotate, they can either mechanically align with the external magnetic field, or the magnetization

can rotate independently without causing physical rotation of the MNPs. This can lead to a reduction in mechanical torque compared to the magnetic torque. Methods for measuring the mechanical torque applied by p-SAF NPs are necessary to understand their mechanical response. Moreover, environmental factors, such as liquid viscosities and rotating field frequencies, can influence the rotation dynamics of MNPs[91–93]. While some literature has explored the mechanical response of p-SAF NPs to a constant external field[85], research on their response to dynamic rotating external fields is limited. The unique disc shape of p-SAF NPs adds complexity to simulating their mechanical response since most studies are based on spherical particles. To advance future applications, a thorough understanding of the mechanical response of p-SAF NPs, both experimentally and through modeling that takes into account their disc shape, is essential. In this thesis, Chapter 7, we specifically study the response of the assembly of p-SAF NPs, namely chains, to rotating magnetic fields.

1.4 Thesis outline

Based on the interest of p-SAF NPs and in view of their many unsolved challenges, the thesis is structured in the following manner.

Chapter 2 provides a detailed overview of the fundamental physics governing the behavior of p-SAF thin film stacks. This includes an exploration of the interfacial interactions within the stack, methods for simulating and fine-tuning magnetic properties, and an examination of the switching behavior of the p-SAF system. Additionally, the mechanical responses of p-SAF NPs to external fields is discussed.

Chapter 3 provides an overview of the various fabrication techniques employed in the production of p-SAF NPs. Furthermore, the magnetic characterization methods employed for measuring p-SAF NPs are described, including both single-particle measurements and collective measurements

Regarding the challenge of fabricating p-SAF NPs, Chapter 4 presents our top-down fabrication protocol for manufacturing these NPs. Our approach relies on substrate conformal imprint lithography (SCIL) in conjunction with other semiconductor industry fabrication techniques.

Chapter 5 outlines the use of Photothermal Magnetic Circular Dichroism (PT MCD) to investigate the switching behavior of 120 nm diameter p-SAF NPs. We observe a distribution of switching fields and confirm that the reversal process of p-SAF NPs is a thermally activated stochastic phenomenon. To gain deeper insights into the switching behavior, Chapter 6 explores the impact of NP size on coercivity and investigates methods to mitigate the substantial increase in coercivity, such as alloying.

Chapter 7 delves further into the mechanical responses of the assembly of p-SAF NPs when subjected to rotating magnetic fields.

Finally, Chapter 8 offers a comprehensive summary of the findings from the preceding chapters and discusses potential avenues for future research.

2

Background

In this chapter, we provide a comprehensive overview of p-SAF NPs, covering aspects from magnetic to mechanical properties, essential for understanding the subsequent sections of the thesis. Our discussion begins with the exploration of methods to tune the magnetic properties of p-SAF NPs. We then focus on the Stoner-Wohlfarth (SW) models employed for estimating the alignment of magnetization. Additionally, we discuss the switching behavior of the p-SAF system, an important feature that affect the activated fields of NPs in applications. Finally, the chapter also includes the mechanical response of p-SAF NPs when exposed to external magnetic fields, providing insights into their implications for practical use.

2.1 Tunable magnetic properties

The multilayer SAF structure encompasses a wealth of physics. One notable advantage of the SAF structure is its tunable magnetic properties achieved through stack engineering. By merely adjusting the thickness or materials of various thin layers, it is feasible to modify the anisotropy and RKKY interaction. In this section, we explore the potential to regulate magnetic properties, especially PMA and RKKY interaction, solely through stack engineering.

2.1.1 Perpendicular magnetic anisotropy

In the thin film stack, whose thickness is typically within the nanometer range, due to a high surface-to-volume ratio, surface anisotropy primarily contributes to the overall anisotropy. Other forms of bulk anisotropy, such as magnetocrystalline anisotropy, are neglected[94]. In our design, PMA arises from the interfacial phenomena associated with FM/Pt, as mentioned earlier. The anisotropy can be adeptly modulated by altering the FM layer's thickness[95 96]. The effective anisotropy constant (K_{eff}) can be expressed as:

$$K_{eff} = \frac{K_{surf}}{t} - \frac{1}{2} N M_s^2 \tag{2.1}$$

Where t represents the thickness of the thin film, K_{surf} denotes the surface anisotropy triggered by the interfacial phenomenon, N is the demagnetization factor, and M_s is the saturation magnetization. The second term in Eq. 2.1 represents the shape anisotropy of a thin film. By decreasing (or increasing) the thickness, the system's anisotropy can be enhanced (or diminished).

It is crucial to understand that there exists a specific range within which the PMA can be adjusted. If the FM layer's thickness is excessively thin, it may not form a continuous film, pushing the system closer to the percolation limit and skewing the hysteresis loop. Conversely, when FM layers become overly thick, the interface anisotropy lacks the capacity to maintain a perpendicular magnetization configuration, leading to a gradual spin-reorientation-transition towards in-plane[97]. To have an idea of the optimal tuning range, consider the CoFeB/Pt layers as an example. The percolation threshold stands at $t_{CoFeB} = 0.4$ nm, while the spin-reorientation-transition occurs around $t_{CoFeB} = 1.5$ nm[97].

2.1.2 RKKY interaction

The RKKY interaction represents an indirect exchange coupling between FM layers separated by a non-magnetic (NM) spacer layer. Depending on the spacer layer's thickness, e.g. in this thesis Ru layer, the adjacent FM layers might be

prompted to align either antiparallel or parallel to one another. Such alignment displays an oscillatory behavior in the sign of the exchange coupling along the space layer's thickness, as illustrated in Fig.2.1. This oscillatory phenomenon originates from the wave-like nature of conduction electrons in the spacer layer, which modifies the interaction between the FM layers. When the spacer layer's thickness varies, these electron waves undergo a phase shift, inducing fluctuations in the intensity and sign of the exchange coupling. By modifying the spacer layer's thickness, one can attain either AF coupling (represented by a negative sign) or FM coupling (symbolized by a positive sign) with different strengths as shown in Fig. 2.1. For instance, in a Co/Ru/Co system, the strongest AF coupling is achieved when the thickness of the Ru layer is approximately 0.7 nm. Although the most straightforward way to adjust the RKKY interaction involves altering the spacer layer's thickness, this adjustment is highly sensitive to thickness variations; even the sputtering of several monolayers can drastically change the coupling strength. An alternative approach involves exploiting the strongest AF-coupled peak while concurrently incorporating dusting layers to fine-tune the RKKY interaction's strength.

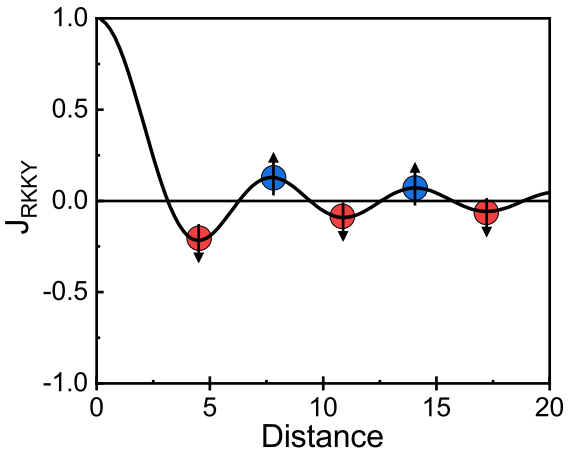

Figure 2.1: The normalized spin density as a function of the distance from the NM/FM interface. Figure from M. Lalieu[98]

Researchers have documented that introducing thin film Pt layers between the spacer and FM layers, e.g. culminating in a Pt/Ru/Pt sandwich structure (refer to Fig. 2.2a), can modulate the RKKY interaction[97]. Figure 2.2b plots the coupling

field as a function of the inserted Pt thickness. Notably, as the Pt layer's thickness grows, there is a corresponding reduction in the coupling field. When this thickness surpasses 1.3 nm, the RKKY coupling field approaches zero. The insertion of a Pt layer between the FM and Ru facilitates precise adjustments to the RKKY coupling's strength, while the FM/Pt interface also boosts the PMA.

Additionally, the FM layer's thickness can influence the RKKY coupling field as captured by the equation:

$$H_{RKKY} = \frac{J_{RKKY}}{\mu_0 M_s t} \tag{2.2}$$

where J_{RKKY} denotes the RKKY coupling constant, M_s is the magnetization, t is the thickness of the FM layer.

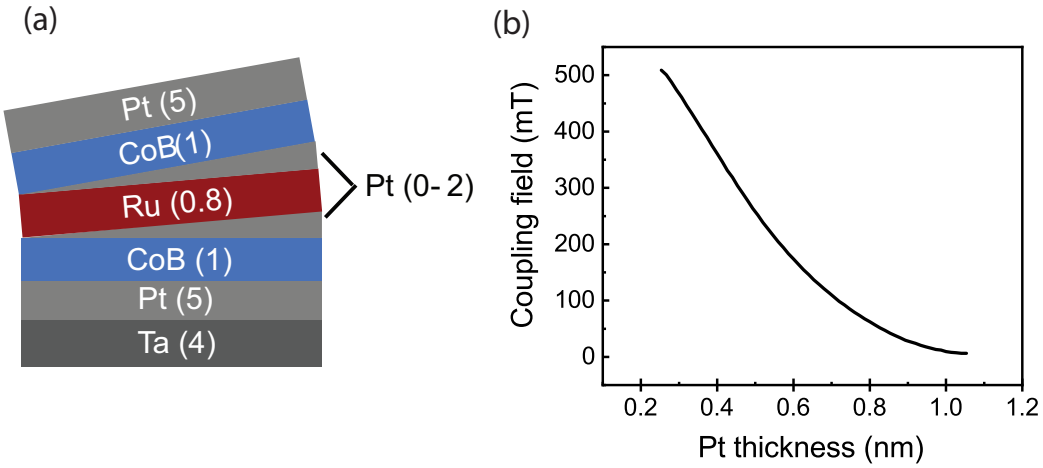

Figure 2.2: (a) SAF stack with a wedge of Pt layers around the Ru layer. (b) The RKKY coupling filed as a function of the insert Pt layer's thickness. The Ru layer's thickness is 0.8 nm, which is at the strongest antiferromagnetically coupled peak. Figure from R. Ernst[99]

2.2 Stoner-Wohlfarth model

When investigating the tuning of magnetic properties, the widely used Stoner-Wohlfarth (SW) model is often employed to predict the magnetization alignment and reversal process of the p-SAF NPs. The SW model operates on the macrospin assumption, suggesting that materials can be characterized by a single magnetic

moment that rotates coherently. Due to the uniaxial anisotropy of p-SAF stack, we can regard the magnetic moment of each FM layer as a single moment. However, in reality, this is not the case and more complicated magnetization reversal processes occur, which are explored further in Section 2.3.

Within the SW model, the system's energy is determined, and the alignment of magnetization can be defined through the energy minimum state. For the p-SAF structure, the energy terms include the anisotropy energy, the RKKY-coupling energy, and the Zeeman energy. Figure 2.3a presents a schematic illustration of the p-SAF NPs used in the SW model. Here, θ_1 and θ_2 denote the angles between the magnetization of the top and bottom FM layers relative to the easy axis, which is defined as the axis perpendicular to the NP's surface. α represents the angle between the external field and the easy axis.

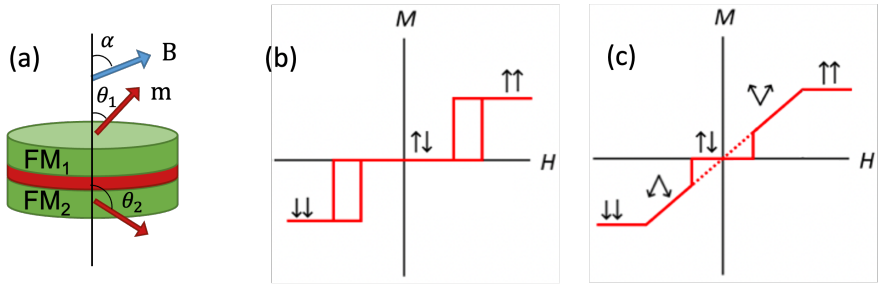

Figure 2.3: (a) A schematic representation of the p-SAF structure within the SW model. The red arrows represent the magnetization of the top and bottom FM layers. The blue arrow illustrats the external field. The hysteresis loop along the easy axis when (b) $\frac{J_{RKKY}}{t} \leq K$and (c) $\frac{J_{RKKY}}{t} > K$, predicted by SW model.

For p-SAF NPs, the anisotropy is uniaxial. The energy associated with this uniaxial anisotropy is given by:

$$E_a = K_{eff} V \sin^2(\theta) \tag{2.3}$$

Here, K_{eff} (with units of Jm^{-3}) denotes the effective anisotropy constant, V symbolizes the volume of magnetic materials, and θ refers to the angle of magnetization relative to the easy axis. K_{eff} arises from the interplay between the surface anisotropy PMA (K_s) and shape anisotropyK_{shape}, expressed as $K_{eff} = 2\frac{K_s}{t} - K_{shape}$; the factor "2" considers the effect of two interfaces of Pt/FM/Pt.

The Zeeman energy, E_{zeeman}, represents the potential energy of a magnetic moment in the presence of an external magnetic field. It is defined by:

$$E_{zeeman} = -\vec{m} \cdot \vec{B} = -M_s V B \cos(\alpha - \theta) \tag{2.4}$$

Here, B corresponds to the external magnetic field, while M_s stands for the saturation magnetization.

In the context of the p-SAF system, the RKKY interaction energy between the two FM layers can be calculated as:

$$E_{RKKY} = \frac{J_{RKKY}}{t} \cos(\theta_1 - \theta_2) V \tag{2.5}$$

where J_{RKKY} (in units Jm^{-2}) is the RKKY coupling energy per area and is defined as $J_{RKKY} = \mu_0 H_{RKKY} M_s t$. The parameter t is the thickness of the FM layer.

We assume that the thickness and the anisotropy of the top and bottom FM layers are the same in the p-SAF stack, the total energy per volume associated with the SAF stack can be expressed as:

$$\begin{aligned} \frac{E_{\text{total}}}{V} =& K\left(\sin^2(\theta_1) + \sin^2(\theta_2)\right) + \frac{J_{\text{RKKY}}}{t} \cos(\theta_1 - \theta_2) \\ & - BM_s \left(\cos(\alpha - \theta_1) + \cos(\alpha - \theta_2)\right) \end{aligned} \tag{2.6}$$

The magnetization tends to stabilize in a direction that minimizes the total energy; mathematically, this implies that $\frac{\partial E_{total}}{\partial \theta_1} = 0$ and $\frac{\partial E_{total}}{\partial \theta_2} = 0$. Solving these two equations enables the determination of θ_1 and θ_2, offering insights into the alignment of the magnetization under varying fields.

Beyond assessing magnetization alignment, the SW model can also be used to simulate the mechanical response of the p-SAF NP. This includes factors such as maximum torque and the p-SAF NPs' alignment relative to the external field, especially when these particles are suspended in a liquid environment. This topic will be further explored in section 2.4.

2.2.1 Competition of RKKY interaction and PMA

As mentioned in Section 2.1, the magnitude of the RKKY interaction and PMA can be precisely and easily adjusted by changing the layers' thickness. However, achieving the ideal sharp switching depicted in Fig. 2.3b, termed a spin-flip transition, is not always feasible. Such a sharp switch is the desired state for practical applications to have "on" and "off" states. Both the effective anisotropy (K_{eff}), primarily from PMA, and the RKKY interaction strength (J_{RKKY}) can affect the hysteresis loop.

When the anisotropy is smaller or comparable to the RKKY interaction ($\frac{J_{RKKY}}{t} \leq K$), the sharp switch can be observed as shown in Fig. 2.3b. When the RKKY interaction exceeds the PMA ($\frac{J_{RKKY}}{t} > K$), a spin-flop transition occurs, causing the magnetization to tilt toward the in-plane direction, as illustrated in Fig. 2.3c[97,100,101]. This behavior results in a slanted curve toward saturation in the hysteresis loop. To determine the spin-flip or spin-flop state, the SW model is a powerful tool to use. Based on this, we have to notice tuning the magnetic properties requires careful attention.

2.3 Switching behavior

As mentioned in Chapter 1, a decrease in the size of p-SAF NPs corresponds to an increase in coercivity. This change is related to the switching behavior of the PMA system. To understand and address this rise in coercivity, this section delves into the physics behind such switching.

In 1947, William Fuller Brown established that the coercivity of a homogeneous, uniformly magnetized ellipsoid should conform to the inequality based on the SW model prediction: $H_c \geq \frac{2K}{\mu_0 M_s} - NM_s$, where H_c represents the coercivity field and N denotes the demagnetization factor[42]. The first term is the anisotropy field, and the second term is the demagnetizing field. However, in real-life situations, the coercivity in materials rarely reaches these predicted levels. This divergence between theoretical predictions and actual measurements is known as Brown's paradox, which emerges because actual materials exhibit imperfections and inhomogeneous rotation of the magnetization. Magnetization reversal typically begins

within a minor nucleation volume surrounding a defect that has lower anisotropy or larger demagnetization field leading to lower coercivity.

In the case of thin film samples, the mechanism is the same. As depicted in Fig. 2.4, magnetization reversal starts with the reversal of a local nucleation center, which is a part with low anisotropy or strong local demagnetization. Following the reversal of the nucleation center, domain wall propagation ensues, expanding the reversed area. The field at which nucleation center reversal occurs is termed the nucleation field (H_n), and the point where the domain wall begins to propagate is termed the propagation field (H_p). When $H_n > H_p$, as soon as H_n is attained, the nucleation centers switch. Given that the field sufficiently supports domain wall propagation, the domain wall can propagate through the entire film switching the whole structure. The switching process is governed by H_n. Conversely, when $H_n < H_p$, even though the nucleation centers switch, the domain wall propagation still doesn't start until H_p is reached. Hence, the switching process is predominantly governed by H_p.

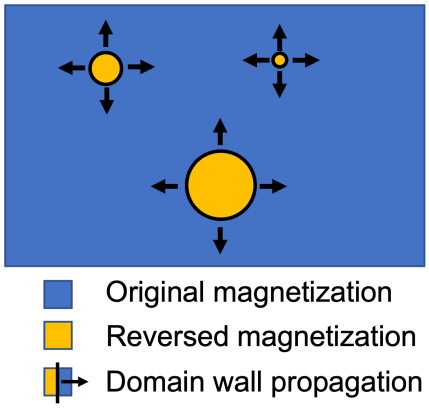

Figure 2.4: Illustration of the switching process of thin film layers, which starts with the reversal of the nucleation center, followed by domain wall propagation.

Regarding the PMA system explored in this thesis, there are reports indicating that, $H_n >> H_p$ [102,103]. This suggests that the critical step in magnetization reversal is the creation of nucleation centers, typically caused by a spontaneous fluctuation at a defect or weak point in the system. Once these nucleation centers are established, the domain wall expands, facilitating the switch of the entire sample. This dynamic sheds light on the observed increase in coercivity when the

size of the nanostructure diminishes. Specifically, as the size decreases, the number of nucleation centers with lower H_n values decreases, requiring a higher field to switch the nucleation center, thereby enhancing the coercivity. Furthermore, variations in nucleation centers across individual nanostructures contribute to the distribution of switching fields.

To quantitively characterize H_n, the SW model can be used to describe the reversal of the nucleation center, especially considering that nucleation is often viewed as a single domain state. The Sharrock formalism[104] then captures the nuances of the switching field as influenced by both time and temperature. Integrating these models yields the equation to describe H_n is[88,105]:

$$\mu_0 H_n = \frac{2K}{M_s}\left(1 - \sqrt{\frac{k_B T}{KV}\ln\left(\frac{f_0 t}{\ln 2}\right)}\right) \tag{2.7}$$

where k_B is the Boltzmann constant, T represents the temperature, f_0 denotes the attempt frequency, t is the measurement time at each applied field, and V corresponds to the nucleation volume. This equation allows us to quantitatively analyze and predict the switching field of nucleation in magnetic materials, taking into account factors such as temperature, time, and material properties. It is further used in Chapter 6 to model the switching fields of nanostructures of varying dimensions.

2.4 Mechanical response

In this section, we will discuss the mechanical rotation of p-SAF NPs under constant magnetic fields. This can help the reader to understand the assembly behavior of the NPs studied in Chapter 7.

T. Vemulkar *et al.* investigated the alignment of released p-SAF NPs in the presence of a constant magnetic field[85]. Depending on the magnitude of the external field, the NPs orient either perpendicular or parallel to it. Figure 2.5(a-b) present optical microscopy images of a suspension of 2 µm p-SAF NPs in liquid exposed

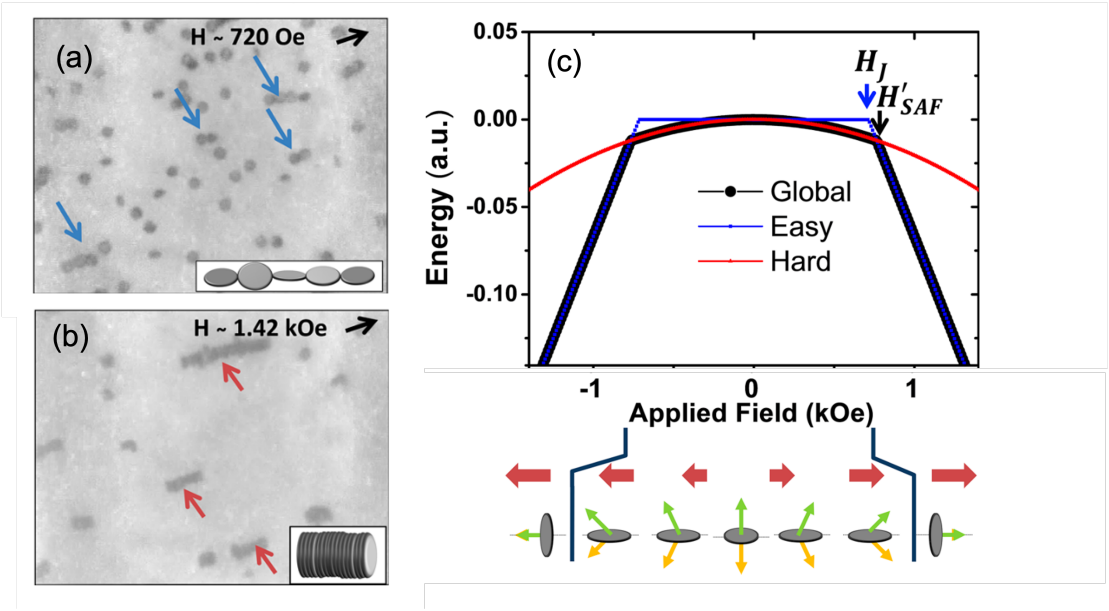

Figure 2.5: Optical microscopy images of the 2 µm SAF microdiscs suspended in water under applied fields of (a) ∼720 Oe and (b) ∼1.42 kOe. The SAF microdiscs comprise $[Ta(2)/Pt(2)]_3[Ta(2)/Pt(2)/CoFeB(1.2)/Pt(0.5)/Ru(0.9)Pt(0.5)/CoFeB(1.2)/Pt(2)]_2/Ta(2)/Pt(2)/[Ta(2)]_3$, with thickness in nm. (c) Minimum energy curves along the easy axis direction (blue), hard axis direction (red), and global (black) for the SAF structure. The figure below displays the disc alignment and the FM layer moment orientations across varying field values; red arrows depict the applied field, while the green and yellow arrows signify magnetization. This figure is adapted from [85].

to fields of 720 Oe and 1420 Oe*. At 720 Oe, the NP surfaces align parallel to the external field, with some NPs forming chains of discs in an edge-to-edge configuration. Conversely, at 1420 Oe, all NPs align perpendicularly, and some are connected face-to-face, forming chains.

The orientation of the NPs relative to the external field, whether parallel, perpendicular, or at any other angle, depends on the angle that minimizes the system's energy. This energy can be calculated from the SW model, as outlined in eq 2.6. Figure 2.5c shows the energy curves of the SAF NPs in relation to the external field, which is directed along both the easy axis and the hard plane. At field H_J, the RKKY coupling field in the easy-axis hysteresis loop, the SAF stack undergoes a switch and saturates. The energy curves for the easy axis and hard plane

*CGS units are used in the reference, however, SI units are used throughout the rest of the thesis.

intersect at $H_{SAF}^{'}$. Beneath $H_{SAF}^{'}$, hard-plane configurations have lower energy, prompting the NPs to align parallel to the external field and the net magnetic moment to align in-plane. Beyond $H_{SAF}^{'}$, the easy axis alignment holds the lowest energy, causing the NPs to rotate and align perpendicular to the external field. Note $H_{SAF}^{'}$ is normally larger than to H_J. With a small external field ($< H_{SAF}^{'}$), the revolving external field drives rotational motion of the particles within the NP plane. Due to its circular geometry, torque transfer to the surrounding environment is inefficient. To capitalize on the torque generated by p-SAF NP, a magnetic field surpassing $H_{SAF}^{'}$ is requisite, ensuring NP alignment perpendicular to the external field.

In this section we explored the minimum field strength $H_{SAF}^{'}$ required for rotating NPs in a liquid environment which is crucial for utilizing these NPs. This knowledge lays the groundwork for later discussions in Chapter 7 of the thesis, where we delve into the assembly of p-SAF NPs and their behavior under a rotating external field.

3

Methods

In this chapter, we present the various methods employed to generate the results, focusing primarily on two aspects: the fabrication techniques and the characterization techniques. Initially, we introduce all the fabrication techniques used to produce p-SAF NPs, including imprinting, magnetron sputtering deposition, ion beam milling, and reactive ion etching. In the second part, we describe different methods to characterize the magnetic properties of p-SAF NPs. This includes photothermal magnetic circular dichroism, which is utilized for measurements at the single-particle level. Additionally, we introduce conventional methods such as Magneto-Optical Kerr Effect (MOKE) and Superconducting Quantum Interference Device (SQUID) for characterizing static magnetic properties

3.1 Micro fabrication methods

Compared to wet chemical synthesis methods for producing nanoparticles, methods based on micro-fabrication techniques in the semiconductor industry, which typically employ lithography, offer a more uniform size distribution. This precision is largely due to the use of a mask that defines the pattern. In this section, we first describe the patterning methods used to create the pattern of NPs, focusing on substrate conformal imprint lithography (SCIL). We then discuss the processes for growing the desired material layers and various methods employed to etch these layers into disc-shaped NPs.

3.1.1 Substrate conformal imprint lithography

SCIL is used to create the disc shape, which can then be used as masks for subsequent etching. Imprint lithography is a technique that can quickly create repetitive structures at a low cost and on a large scale. The specific advantage of SCIL is its ability to achieve conformal contact on a large scale, as the name suggests, which enables precise pattern transfer even at nanometer resolution[106].

The process of SCIL is illustrated in Fig. 3.1. The imprint resist, which is a silicon-oxide based sol-gel, is first spin-coated on the wafer. The primary component of the resist comprises organically modified silicon precursors, alcohol, and water. These components react to form a stable Si-O-Si bond, which serves as the foundation for silicon oxide glass. During and after the resist is spin-coated, alcohol and water evaporate from the liquid, facilitating the formation of the silica network. A stamp is then pressed into the resist. Due to capillary forces, the resist fills the cavities in the stamp automatically. The stamp remains in contact until the resist layer solidifies through heating. Once the resist hardens, the stamp is removed, leaving behind the desired pattern.

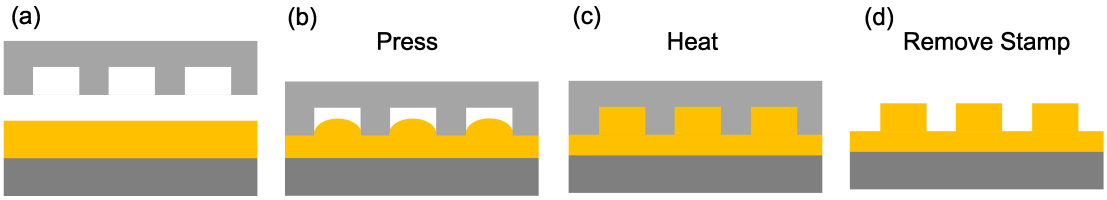

Figure 3.1: Schematic of the nanoimprint process: (a) Spin-coating of the resist. (b) Pressing the stamp into the resist. (c) Heating the resist to solidify it. (d) Removing the stamp.

The conformal contact is achieved through a specially-designed stamp and resist[106]. In the SCIL process, a composite stamp is specially designed as depicted in Fig. 3.2(a). It consists of two rubber layers: high-modulus PDMS and commercial PDMS, supported by a thin glass layer[107,108]. For successful imprinting, a low Young's modulus is essential to ensure conformal contact. However, a low Young's modulus might lead to the pattern collapsing after imprinting[109,110]. In SCIL, a combination of high-modulus PDMS and low-modulus PDMS is used[106]. High-modulus PDMS possesses a high Young's modulus and retains the pattern

structure, facilitating stable feature reproduction without deformation[111]. A softer PDMS is incorporated to maintain the conformal contact. The thin glass is flexible in the out-of-plane direction (refer to Fig. 3.2b), enabling consistent conformal contact. Furthermore, in-plane rigidity of the glass plate helps in minimizing pattern distortions[106].

The resist used in SCIL is also distinctively formulated. Typically, TMOS, characterized by the chemical formula $Si(OCH_3)_4$, is employed for imprinting. It undergoes hydrolysis (forming silicon hydroxyl groups ($(CH_3O)_3Si$-OH) upon reacting with water) and condensation (where two silicon hydroxyl groups interact, releasing water to form a Si-O-Si bond) to create Si-O-Si bonds, thereby cross-linking to form a thin film atop the substrate. However, both the hydrolysis and condensation reactions of TMOS can induce resist shrinkage, potentially distorting the original pattern[112,113]. To address this, organically-modified silicon precursors like methyl-tri-methoxy-silane (MTMS), represented by the chemical formula $CH_3Si(OCH_3)_3$, are introduced to partly replace TMOS. This modification allows tuning the degree of cross-linking in the resist, culminating in reduced shrinkage of the final structure[106]. A comprehensive explanation is beyond the scope of this section, but interested readers can delve deeper into the topic in the cited thesis[106].

3.1.2 Magnetron Sputtering

Magnetron sputter deposition is employed to deposit the p-SAF metallic layer. This physical vapor deposition technique offers precision control of the thin film thickness at the sub-nanometer level. Given its simplicity, high growth rate, and cost-effectiveness, sputtering is a prevalent choice in the industry for magnetic thin film deposition.

Figure 3.3 depicts the sputtering process. The substrate is positioned in an ultra-high-vacuum chamber, which maintains a base pressure of 10^{-9} mbar to avoid contamination, and is placed beneath the target. Ar gas is fed into the chamber, and a high voltage is established between the anode and the cathode target, leading to the formation of an Ar^+ plasma. The energized Ar^+ ions are propelled towards the cathode target by the negative electrical field potential. A magnet,

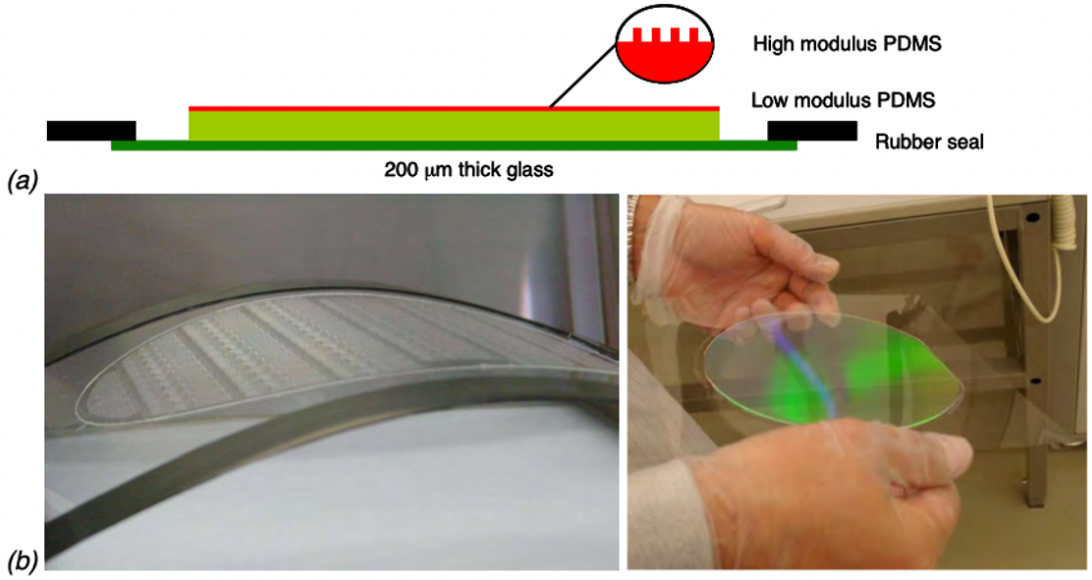

Figure 3.2: (a) Illustration of a SCIL composite stamp. (b) Images of SCIL stamps, demonstrating the flexibility in the out-of-plane direction by bending the stamp. In the image on the right, interference colors are visible, stemming from a repetitive pillar pattern. Image from [106]

positioned behind the target, establishes fields around it. This configuration helps in confining the plasma close to the target, thereby reducing background pressure and boosting the growth rate. Upon reaching the target, the energetic Ar^+ ions displace target atoms through momentum transfer. The released atoms then migrate to the substrate, resulting in thin film deposition.

3.1.3 Ion beam milling

Ion beam milling (IBM) is a prevalent non-selective physical etching technique that utilizes a beam of highly-accelerated ions to etch a sample. The sample is bombarded by the ion beam, and during this collision, the highly-energetic ions transfer their momentum to the surface atoms. This results in the removal of these atoms from the sample. IBM is commonly employed in metal etching for the magnetic random access memory (MRAM) industry.

The working principle of IBM is depicted in Fig. 3.4. The gas, in our instance, Ar, is introduced into the chamber and is subsequently ionized through radio

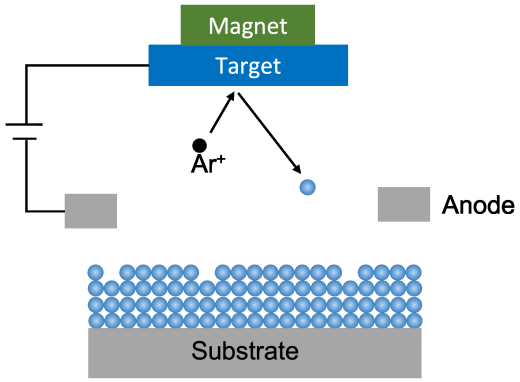

Figure 3.3: Schematic of the magnetron sputtering process. Ar^+ plasma is generated, and the Ar^+ ions bombard the target material. Atoms ejected from the target material attach to the substrate and form a thin film.

frequency plasma sources. The generated Ar^+ ions are then accelerated by an electric field, forming a high-energy ion beam. This ion beam is subsequently neutralized by electrons from a neutralizer to prevent the accumulation of charged particles on the sample. To ensure uniform etching, the sample holder can be adjusted both in tilt and rotation during the etching process. A secondary ion mass spectrometer (SIMS) is positioned near the sample. This serves as an end-point detector, monitoring the milling progress by analyzing the ejected secondary ions.

There are several phenomena that can lead to ill-defined structures after etching, such as faceting, trenching, and redeposition[114]. In our fabrication of NPs, redeposition can cause irregular shapes at the edges of NPs, which will affect their functionalization and subsequent applications. It is one of the primary issues we aim to address. Figure 3.5 illustrates the principle of redeposition. When the incident ions reach the sample and kick the atoms away from the sample surface, not all of these sputtered atoms manage to escape from the sample's vicinity. Some remain close to the sample's surface and can adhere back to it, leading to the phenomenon of redeposition.

To get rid of redeposition, one direct approach is to employ a thin and hard mask, which can reduce the area that sputtered atoms might attach to[115]. Wet chemical cleaning has also been reported to remove redeposition, but the chosen solution requires careful selection to ensure it does not adversely affect the material

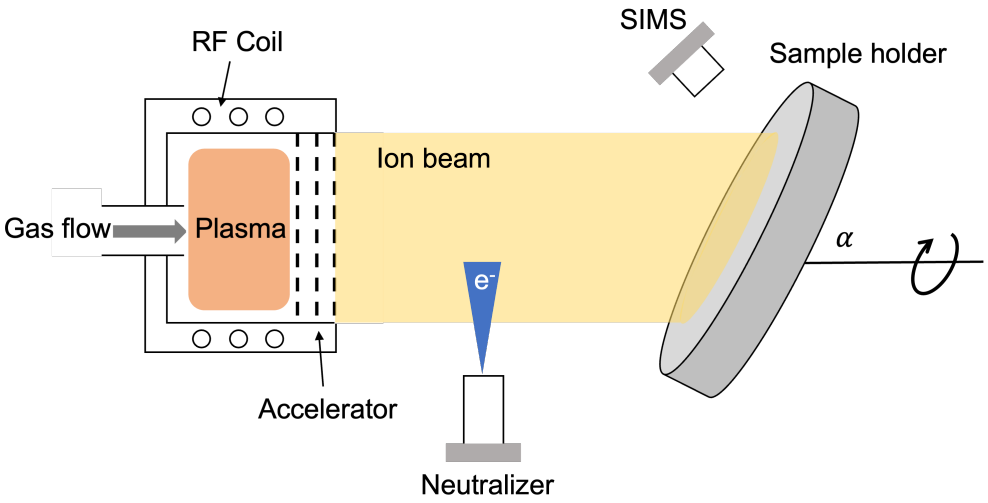

Figure 3.4: The schematic of an ion beam miller. The Ar gas flows into the chamber and is ionized by the radio frequency coil. The ionized Ar^+ is directed and accelerated to the target by the accelerator. A neutralizer is used to eject electrons to neutralize the ion beam before reaching the sample. An end-point detector, SIMS, is placed next to the sample to detect the outgoing atoms.

properties[116]. Another widely adopted method is multi-step milling[117,118]. The process begins with high-angle etching (denoted as α in Fig. 3.4), which offers a rapid etch rate and serves as the primary etching step. This is followed by a low-angle etching, mainly to remove the redeposition on the mask's sidewall. In our fabrication protocol, we combine the multi-step etching process with a post-fabrication sonication process, which physically removes the redeposited material from the edges. Further details are elaborated upon in Chapter 4.

3.1.4 Reactive ion etching

Reactive ion etching (RIE) is a prominent dry etching tool utilized in the semiconductor industry. It operates based on a selective etching process, driven by specific chemical reactions. Depending on the material targeted for etching, various reactive gases that can interact with the material are selected, such as O_2, Cl_2, CHF_3, and C_2F_6.

In this thesis, RIE is employed to etch SiO_2-based nanoimprint resist. A mixture of CHF_3 and O_2 gases is used. The reactions involved are[119]:

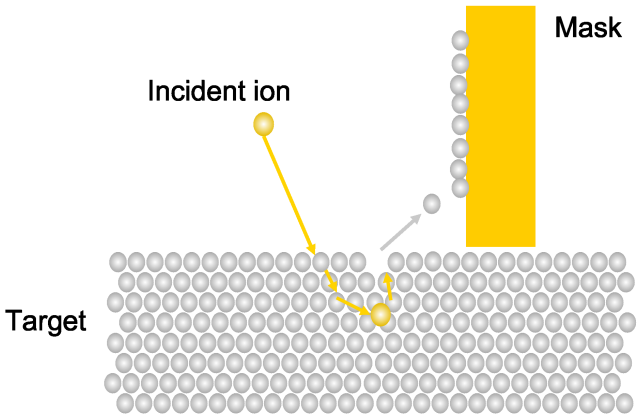

Figure 3.5: Schematic illustration of redeposition during ion beam milling. The sputtered atoms (shown in grey) attach to the mask (shown in yellow).

$$CHF_3 + e^- \rightarrow CHF_{3-i} + iF^- \tag{3.1}$$

$$SiO_2 + CHF_3 \rightarrow CO_2 + SiF_4 + H_2 \tag{3.2}$$

Under plasma conditions, CHF_3 dissociates to form fluorine ions (F^-), which react with SiO_2. The reaction byproduct, SiF_4, is gaseous and is evacuated from the chamber.

A schematic of the RIE etching process is depicted in Fig. 3.6. The chamber is filled with the reactive gases, wherein the sample is placed. A plasma forms between two charged plates, accelerating the formed F^- ions toward the positively charged plate where the sample resides. This ionized gas interacts with the sample, affecting the etching process, after which the reaction byproduct gases are evacuated from the chamber. It's important to note that due to the bombardment of ions, there is also a component of physical etching.

3.2 Magnetometry

In this section, we present the primary characterization methods employed in this thesis. We begin by explaining the principles behind the Magneto-Optical Kerr Effect (MOKE). Following this, we delve into the Photothermal magnetic circular dichroism (PT MCD) and MOKE measurement methods, both of which

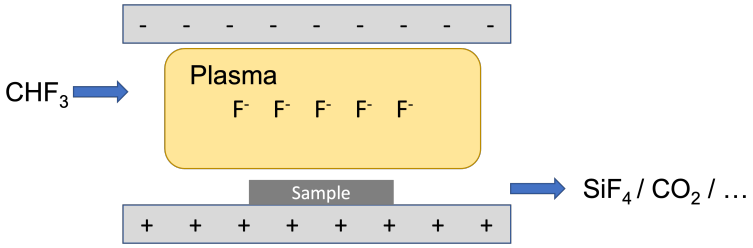

Figure 3.6: Schematic illustration of RIE process

derive from the MOKE effect. Lastly, a brief introduction to the Superconducting Quantum Interference Device (SQUID) is provided.

3.2.1 Magneto-optical effect

Magneto-optical (MO) effects refer to the phenomena in which the characteristics of an electromagnetic wave are changed upon interaction with a magnetized medium. An example of MO effects is the Faraday effect, discovered in 1845 by Michael Faraday. This effect demonstrates that the polarization axis of linearly polarized light rotates when it propagates through a transparent magnetized medium. Subsequently, in 1877, John Kerr observed a change in the polarization of light upon reflection, rather than transmission, from a magnetic material. This phenomenon is known as the MOKE[120].

The core principle behind the MO effect stems from the differential refractive indices that right-hand (RCP) and left-hand (LCP) circularly polarized light display when interacting with a magnetic material. Using the MOKE effect as an illustration, as depicted in Fig. 3.7a, linearly polarized light comprises a combination of RCP and LCP light. When this light reflects off a magnetic surface, it traverses the material. During this process, the LCP and RCP light undergo differing velocities and absorption rates. This creates a significant phase and amplitude difference between the two polarization modes, leading to a rotation of the polarization axis of the reflected light, termed Kerr rotation (θ), and a change in amplitude relative to the incoming light, referred to as Kerr ellipticity (ε), as illustrated in Fig. 3.7a. These effects are directly linked to the material's magnetization and can thus be employed to measure the magnetic properties of materials.

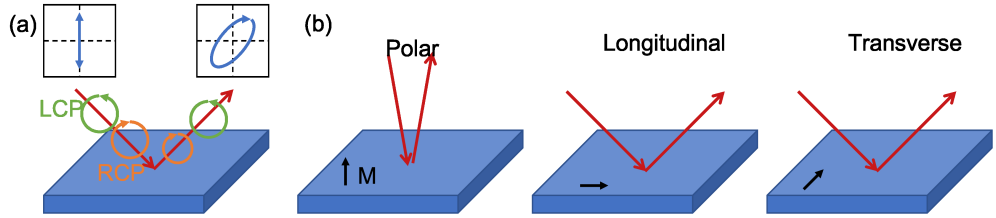

Figure 3.7: (a). Schematic illustration of the MOKE effect. The inserted linearly polarized laser (red arrow) changes in rotation and ellipticity when reflected from a magnetic surface. The green and orange circles represent left-handed (LCP) and right-handed (RCP) circularly polarized light. (b). Three different MOKE configurations: polar, longitudinal, and transverse. Each mode is defined by the alignment of the magnetization (black arrows) relative to the surface and the plane of the incident laser.

Three primary configurations exist for observing MOKE: longitudinal, transverse, and polar, as illustrated in Fig. 3.7b. Each configuration is distinguished by a specific alignment of magnetization relative to the incident laser beam's plane and the sample surface. Notably, the polar MOKE configuration is sensitive to out-of-plane magnetization, particularly when the laser beam is aligned with the magnetization axis. In practice, measurements for out-of-plane magnetized samples, the main subject of this thesis, are mostly performed using the polar MOKE configuration, where the laser beam is incident perpendicularly to the samples.

3.2.2 Photothermal magnetic circular dichroism

Photothermal magnetic circular dichroism (PT MCD) is an indirect measurement technique that allows for the magnetic characterization of single magnetic particles at the nanometer scale. In this thesis, we employ PT MCD to measure the hysteresis loop of a single 120 nm diameter p-SAF NP. The magnetic characterization builds upon the MOKE effect described in Section 3.2.1, which we then use photothermal microscopy to observe the MCD. In this section, we outline the fundamentals of magnetic circular dichroism and the photothermal effect, followed by a description of the PT MCD setup used for single p-SAF NP characterization.

Magnetic circular dichroism

Magnetic circular dichroism (MCD) refers to the differential absorption of LCP (σ_L) and RCP (σ_R) light in magnetic materials. This phenomenon shares the same microscopic origin as MOKE, as discussed in Section 3.2.1. The differential absorption ($\Delta\sigma$) can be expressed as:

$$\Delta\sigma = \sigma_L - \sigma_R \tag{3.3}$$

It is important to note that the geometric asymmetry of particles can also lead to circular dichroism (CD), manifesting as different absorption rates. However, MCD differs in that it is independent of geometry and arises solely from the magnetic properties, a characteristic present in magnetic materials with magnetization. In our measurements of p-SAF NPs, the particles exhibit a circular shape; therefore, no CD signal from the shape is expected. We predominantly utilize the polar MOKE configuration, depicted in Fig. 3.7.

Photothermal effect

The differential absorption of polarized light is measured using photothermal microscopy, an optical technique uniquely sensitive to absorption. A schematic illustration of the photothermal effect is displayed in Fig. 3.8. When a small nanoparticle submerged in a liquid medium is illuminated, it absorbs light. This absorbed energy is primarily converted into non-radiative pathways, leading to heat generation. This generated heat induces changes in the refractive index of the liquid surrounding the particle. This refractive index change results in a phenomenon referred to as the "thermal lens"[121]. The refractive index change can be monitored by a secondary laser, termed the probe beam, whose focal plane is affected by a thermal lens. It's essential to note that the wavelength of the probe beam is selected to be significantly distant from the absorption resonance of the particle, avoiding further heating. Through the thermal lens, differential absorption can be detected.

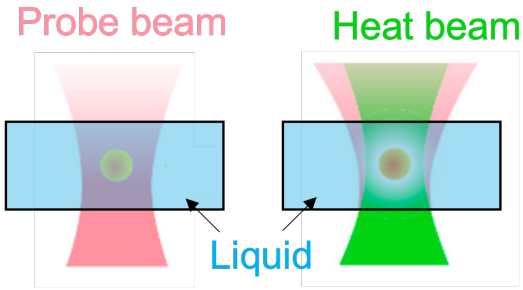

Figure 3.8: The photothermal effect of a nanoparticle (yellow ball) immersed in a liquid environment. When a heating beam (depicted in green) illuminates the particle, it generates heat in the surrounding area, leading to local changes in the refractive index. This change creates a thermal lens, which in turn affects the propagation of the probe beam (illustrated in pink).[122]

PT MCD setup

Combining the MCD technique with PT microscopy yields the PT MCD setup, whose schematic illustration is depicted in Fig. 3.9. A heating laser (illustrated in green) with a wavelength of 532 nm and a tightly focused probe beam (depicted in red) with a wavelength of 780 nm are employed. The heating laser illuminates the sample via the microscope objective, with its polarization state being periodically modulated between LCP and RCP at a specific frequency f_m. This polarization modulation is achieved using a suite of polarization optics. For instance, an electro-optical modulator (EOM) rotates the incoming linear horizontal polarization by 90 degrees, while a quarter-wave plate (QWP) converts these two orthogonal linear states into LCP and RCP. Further details on the optical components can be found in the publications[122–124]. The probe beam is directed onto the sample using the same microscope objective. To efficiently detect the back-scattered probe beam signal, a combination of a polarizing beam splitter (PBS) and QWP is employed. Before being focused onto the photodiode (PD) detector, the scattered probe beam undergoes filtration from the heating beam through a band-pass filter (BP780). Given that the PT signal is typically very small, a lock-in amplifier set to the modulation frequency f_m is incorporated to amplify the signal.

The measured NPs are immersed in an immersion medium. The change of the probe beam upon heating is linearly dependent on the thermorefractive coefficient

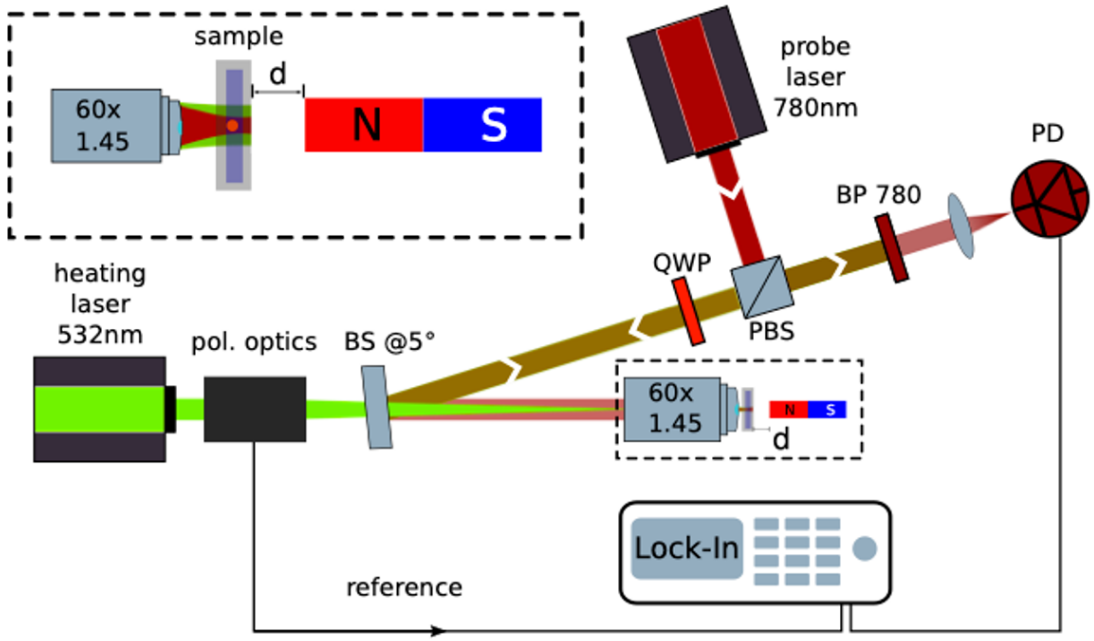

Figure 3.9: Schematic representation of the photothermal magnetic circular dichroism microscope setup. The 532 nm heating laser beam traverses a set of polarization optics, modulating its polarization between left- and right-circularly polarized states at a specific frequency. The 780 nm probe laser is directed through a combo of a polarizing beam-splitter (PBS) and a quarter-wave plate (QWP). It then merges with the heating beam at a beam-splitter (BS) at an approximate angle of 5°. The gathered probe light is filtered from the heating light using a band-pass filter (BP 780). The photothermal signal is extracted using a lock-in amplifier. A cylindrical permanent magnet, positioned perpendicular to the sample plane, can be adjusted to a distance to exert a magnetic field on the sample. The inset provides a magnified perspective of the dashed box. This figure is sourced from the paper[124].

$\partial n/\partial T$ of the enveloping medium, where n is the refractive index and T represents the temperature[125]. To attain a stronger PT signal, a medium with a high thermorefractive coefficient should be chosen. An external magnetic field is generated by a cylindrical NdFeB magnet positioned perpendicular to the sample plane. Adjusting the magnet's position relative to the sample allows for changes in the applied magnetic field. Figure 3.10 shows an example of a PT MCD measurement performed on magnetite (Fe_3O_4) particles with a diameter of 400 nm. The particles are marked with circles. When exposed to opposing magnetic fields, they exhibit opposite signals, indicating the reversal of magnetic moment alignment. By collecting the signal variations from individual particles under an applied external

magnetic field, we can obtain the hysteresis loop for a single particle.

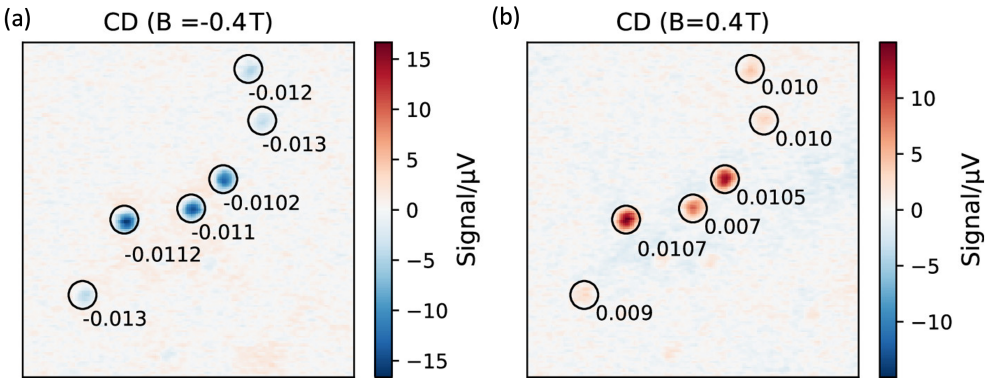

Figure 3.10: An example of the PT MCD measurements of 400 nm diameter magnetite (Fe_3O_4) particles in hexadecane exposed to (a) -0.4 and (b) 0.4 T external fieldin hexadecane. Individual particles exhibiting considerable MCD are marked with circles and numbers to indicate their g factors. This figure is sourced from the ref[124].

3.2.3 MOKE

Static polar MOKE (refer to Fig. 3.7b for the configuration), sensitive to out-of-plane magnetization, serves to measure the magnetization switching of our p-SAF NPs. Note the technique is not used for single NP measurement. The experimental setup of MOKE is depicted in Fig. 3.11. The laser beam traverses the polarizer (P1) and is linear polarized. Subsequent to this polarization, the laser beam is focused on the sample, engaging with the magnetic material, which results in Kerr rotation. After reflection from the sample's surface, the beam navigates through a second polarizer (P2), termed the analyzer. The analyzer P2 is purposefully aligned nearly orthogonal to the initial polarizer P1 to enhance the signal. The intensity of this reflected beam is subsequently detected by a photodetector.

To obtain an optimal signal-to-noise ratio, a combination of a photo-elastic modulator (PEM) and a lock-in amplifier is employed. The PEM, situated post P1, uses the photo-elastic effect to cause a consistent oscillation in the light's polarization state. The captured signal is synchronized to the PEM's driving frequency (set at 50 kHz for this thesis). Through the lock-in amplifier, the arrangement distinguishes and measures the laser's ellipticity or rotation, separating it from other effects. Both the change in ellipticity, measured at the first harmonic of the

PEM frequency, and rotation, measured at the second harmonic, can be used to reflect the change of magnetization, more details are described in the ref[98].

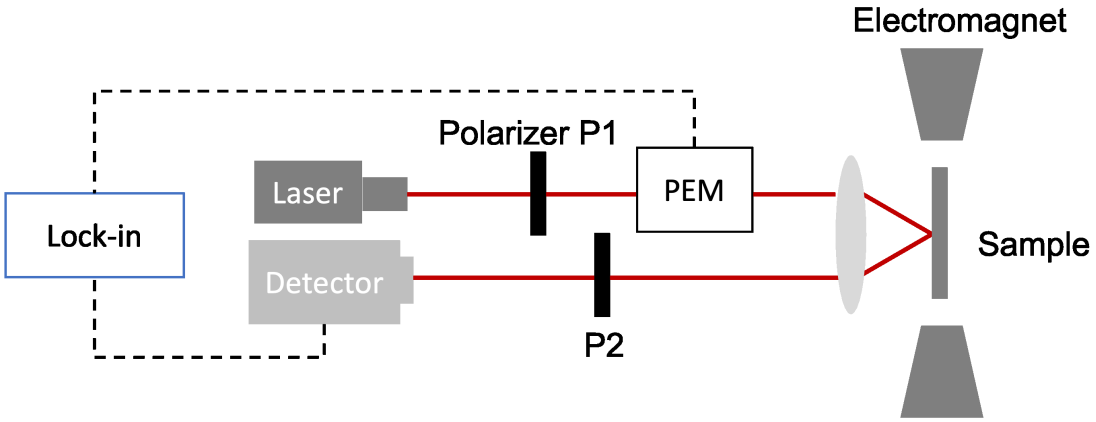

Figure 3.11: Schematic of the MOKE measurement setup.

3.2.4 SQUID

Superconducting Quantum Interference Device with a Vibrating Sample Magnetometer (SQUID-VSM) is a typical technique used to quantitatively characterize the static magnetic properties, such as the magnetic moment, of a sample. The principle of the technique is based on VSM, where the sample is situated between two coils and is set to vibrate. This vibration generates an oscillating magnetic field emanating from the sample's inherent magnetic moment. The coils, being sensitive to these fluctuations, detect this oscillating field through the current induced. By measuring this induced electrical signal, the local magnetic moment of the sample can be determined.

In SQUID-VSM, the coils are replaced with superconducting coils containing Josephson junctions. The vibration can induce a current flow, which induces an asymmetry in the Josephson junctions, causing a potential difference between two junctions. From this difference, the magnetic moment can be recalculated. More details of the working principle of SQUID can be found in the literature[126]. Compared to VSM, SQUID-VSM offers a remarkable detection resolution reaching 10^{-11} Am^2. Such high sensitivity makes SQUID-VSM exceptionally suitable for probing SAF stacks which have low magnetization at small fields. In this the-

sis, we use SQUID-VSM to measure the hysteresis loop of our p-SAF NPs. For measuring 120 nm diameter NPs, approximately 5×10^6 NPs are required to reach the sensitivity.

4

Substrate conformal imprint fabrication process of synthetic antiferromagnetic nanoplatelets

Methods to fabricate and characterize monodisperse magnetic nanoplatelets for fluid/bio-based applications based on spintronic thin-film principles are a challenge. This is due to the required top-down approach where the transfer of optimized blanket films to free particles in a fluid while preserving the magnetic properties is an uncharted field. Here, we explore the use of substrate conformal imprint lithography (SCIL) as a fast and cost-effective fabrication route. We analyze the size distribution of nominal 1.8 µm and 120 nm diameter platelets and show the effect of the fabrication steps on the magnetic properties which we explain through changes in the dominant magnetization reversal mechanism as the size decreases. We show that SCIL allows for efficient large-scale platelet fabrication and discuss how application-specific requirements can be solved via process and material engineering.[*]

4.1 Introduction

Magnetic particles have been widely used in bio-applications due to their ability to mechanically manipulate their surroundings remotely via externally applied magnetic fields. In particular, the utilization of magnetic torques induced via

[*]This chapter has been published in *Applied Physics Letters*: **Li, J.** *et. al.*[127]

an externally rotating magnetic field is of interest for applications such as micro mixing[128], cancer treatment[129,130] and the manipulation of cells[131]. Superparamagnetic nanoparticles (SPNs) have traditionally been used in torque-related applications[132]. However, due to their limited magnetic anisotropy and spherical shape, the translation of magnetic torque to mechanical torque is limited. To overcome these limitations, particles with enhanced shape or magnetic anisotropy have been studied, e.g. NiFe nanodiscs with a vortex spin configuration[133,134], and magnetic nanorods[135]. Synthetic antiferromagnetic (SAF) nanoplatelets (NPs) with high perpendicular magnetic anisotropy (PMA) are among the most promising candidates[23,62,63,85].

SAF NPs with PMA typically consist of a multilayer stack: Ta/Pt/Co/Pt/Ru/Pt/Co/Pt. The strong hybridization of the 3d-5d orbitals at Co and Pt interfaces induces a large PMA[74,75]. This large anisotropy and the fact that PMA induces a *hard-plane* anisotropy (the plane of the disc) and an *easy-axis* perpendicular to the the disc, are the key factors for effective magnetic-mechanical torque transduction[23]. The two ferromagnetic layers are antiferromagnetically coupled by the Ru layer through the Ruderman-Kittel-Kasuya-Yoshida (RKKY) interaction[77–79]. The SAF stack exhibits a zero net magnetic moment at zero applied magnetic field, preventing the aggregation of particles in liquid at zero field; a key requisite for applications. The Pt layers around the Ru layer tune the RKKY interaction and increase the PMA[97]. The high tunability of the PMA and RKKY and the freedom in shape and size of the platelets using top-down lithography methods make SAF NPs fascinating for remotely induced nanoscale torque applications.

However, one of the major issues is to fabricate monodisperse SAF NPs of different size, especially in nanometer range with high throughput and low cost. UV-lithography with a lift-off process has been reported to pattern 1.8 µm diameter SAF NPs[62]. However, due to the diffraction limit, it is hard to reach the sub-micron meter with conventional UV-lithography. Nanoimprint was used to fabricate SAF NPs with in-plane anisotropy at much smaller diameters down to 122 nm[81,136]. Although smaller size can be achieved, the additive lift-off process has its native problem, i.e. it is difficult to obtain a uniform thickness when the critical dimensions reach the resist thickness. As the PMA-SAF system requires Ångstrom scale control of the layer thickness to stabilize the magnetic behavior,

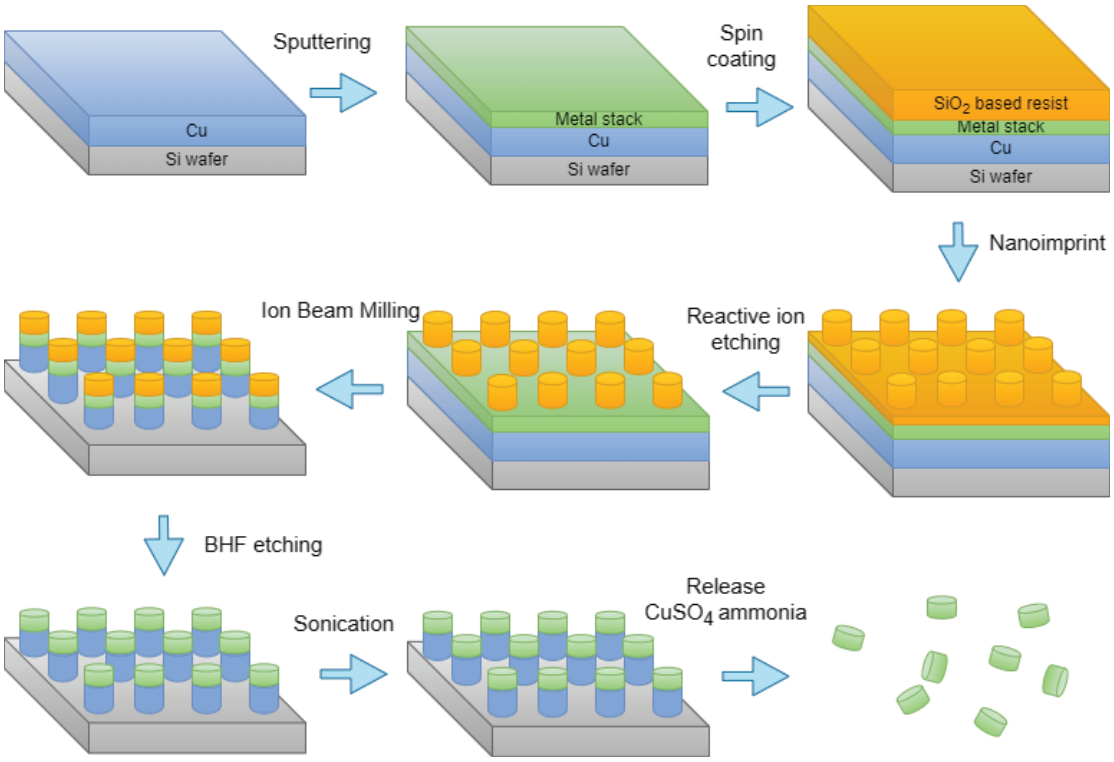

Figure 4.1: The schematic of the fabrication process of PMA-SAF NPs. (1) A sacrificial layer of Cu is sputtered on the Si wafer. (2) The SAF stack is sputtered on the Cu layer. (3) Spin-coat the resist. (4) Imprint. (5) Reactive ion etching (RIE) is used to etch the resist. (6) The metal layers are etched by ion beam milling (IBM). (7) The remaining resist is removed by buffered hydrogen fluoride (BHF) solution. (8) The re-deposition caused by the IBM process is removed by sonication. (9) Finally, the NPs are released by dissolving the Cu layer in $CuSO_4$-ammonia solution

such additive methods cannot be used. Hence, a subtractive method is preferred where one can start with a blanket film on a wafer. Recently, nanosphere lithography; where polystyrene (PS) beads were used as hard masks, combined with an ion milling process was reported to produce NPs with different sizes[64,137,138]. Nevertheless, this method suffers from non-uniform PS bead size and moreover, the yield depends on the distribution of the beads over a large area.

In this paper, we present a subtractive method based on substrate conformal imprint lithography (SCIL) to fabricate monodisperse SAF NPs in the micrometer and nanometer range. The stamp used in SCIL is composed of two rubber layers on a thin glass support (see Fig. 3.2). The SCIL technique is based on a difference between the in-plane stiffness of the glass which avoids pattern deformation

over large areas, while the out-of-plane flexibility from the rubber layers allows conformal contact to underlying surface features[139]. With these properties, SCIL can be used to pattern large wafers up to 300 mm while keeping a uniform size of the features. In addition, this technique can be used to fabricate NPs from the nanometer to micrometer range and different shapes of the platelets can be thought of as the stamp used for the process can be custom made. Here we focus on two sizes of SAF NPs - 120 nm diameter NPs, which are within the range suitable for in vivo circulation and thus ideal for nanotherapeutics[140], and 1.8 µm diameter NPs, which are designed to manipulate their surroundings in the micrometer range. The magnetic properties of the discs after fabrication are studied and compared to literature, indicating that the SCIL fabrication route is a good candidate for large-scale PMA-SAF production.

4.2 Methods

The SCIL based fabrication process for the PMA-SAF platelets is outlined in Fig. 4.1. We start with depositing a 2" Si wafer with a 30 nm sacrificial Cu layer and the SAF stack using DC magnetron sputtering.[†] The basic SAF stack is [Ta(4)Pt(2)/CoB(0.8)/Pt(0.3)/Ru(0.8)/Pt(0.3)/CoB(0.8)/Pt(2)] with thickness in nanometers. For 1.8 µm SAF NPs we use 5 repetitions of the basic stack and for 120 nm NPs we use one repetition. Here 5 repetitions are used for 1.8 µm SAF NPs to increase the total thickness and prevent roll-up of the thin film during release (see Fig. A.1). Then, we spin-coat the SCIL sol-gel resist and manually imprint the pillar structure using a custom SCIL imprint station, followed by sol-gel dependent hot plate bake and stamp removal. After transfer, the masks are etched by selective reactive ion etching (RIE) to open the area around the pillars. The metal stack is then etched by a non-selective Ar ion beam milling (IBM) step and followed by buffered HF (BHF) dip to remove the residual sol-gel resist on top of the nanoplatelets. During the IBM process, re-deposition on the masks can cause irregular side walls to grow around the NPs (see Fig. A.3(e-f)). To remove the re-deposited material, the sample is immersed in deionized (DI) water and sonicated for 20 minutes. Finally, the NPs are released in solution by dissolving the Cu layer in 1.5% $CuSO_4$- 10% ammonia solution[81].

[†]More details of the fabrication process are in Appendix A.1

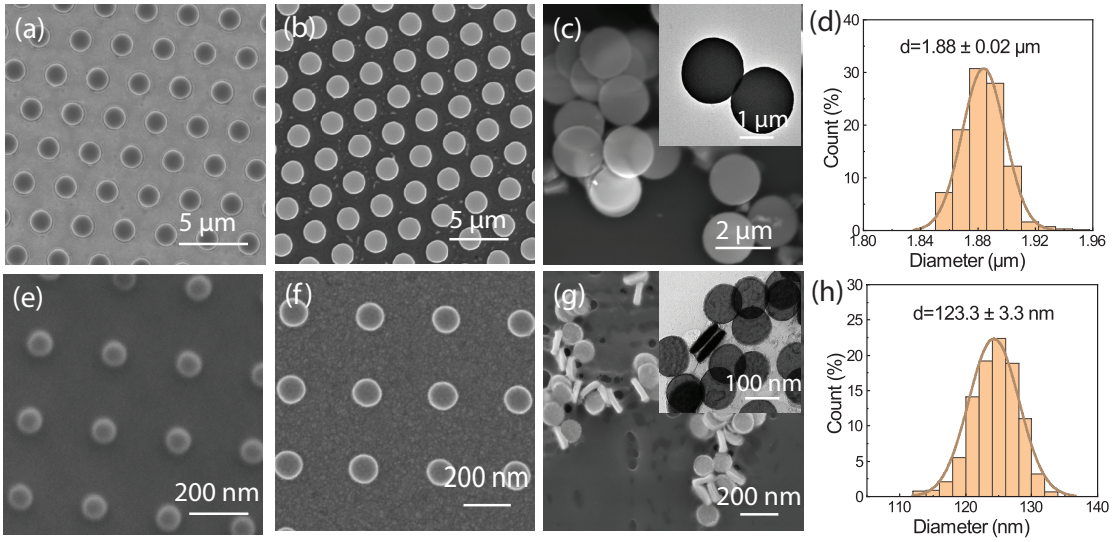

Figure 4.2: SEM images of 1.8 µm diameter and 120 nm diameter SAF NPs (a, e)after imprinting, (b, f)before release, and (c, g)after release and dried on a Si substrate. The insert of (c) and (g) is the TEM image of 1.8 µm and 120 nm diameter SAF NPs. (d) and (h) is the size distribution of released 1.8 µm diameter and 120 nm diameter SAF nanoplatelets calculated from NPs before released.

4.3 Results

The patterns of 1.8 µm and 120 nm diameter NPs after nanoimprint, before release, and after release, were observed using scanning electron microscopy (SEM) as shown in Fig. 4.2. More details can be found in Fig. A.3. After imprinting, monodisperse disc-shaped patterns are transferred for both 1.8 µm and 120 nm diameter NPs shown in Fig. 4.2(a) and 4.2(e). From Fig. 4.2(b-c) and Fig. 4.2(f-g), we see that the disc patterns are transferred into the metallic layer with uniform size after different etching processes and the NPs can be released without damaging the shape. The extracted size of the SAF NPs is shown in Fig. 4.2(d) and Fig. 4.2(h), which is 1.88 ± 0.02 µm and 123.3 ± 3.3 nm, indicating a highly reproducible SCIL pattern transfer over the full 2" wafer area, with the size distribution approximately 1.1% and 2.6%.[‡]

Here, our used stamps have a packing density of 34 % and 11% for 1.8 µm and 120 nm NPs respectively (see Appendix A.2 for details). This packing density is not as high as the reported value of 50% for 1 µm discs and of 31% for 100 nm discs

[‡]The method to obtain size distribution is shown in Appendix A.4

fabricated through nanosphere lithography[64]. However, the yield of SCIL which is determined by the specific stamp used for imprint can easily be increased by using a higher-packed mask and is not further addressed here.

To investigate the change in magnetic response due to the fabrication, the hysteresis loops of 1.8 µm and 120 nm SAF NPs were measured by SQUID magnetometry as shown in Fig. 4.3 and Fig. 4.4. The left and right column of the figures show the hysteresis loops measured with the applied magnetic field perpendicular (easy-axis) and parallel (hard-plane) to the film plane respectively. To obtain the minor loop, the samples were first saturated in a positive field, then the magnetic field was decreased to zero and swept back to the positive saturation field. From the minor loop, the RKKY coupling field ($\mu_0 H_{rkky}$) is defined as $\frac{\mu_0 H_1 + \mu_0 H_2}{2}$ and the coercivity ($\mu_0 H_c$) is defined by $\frac{\mu_0 H_2 - \mu_0 H_1}{2}$ as shown in Fig 4.3(b)[97]. The standard deviation of $\mu_0 H_1$ and $\mu_0 H_2$ is defined as the switching field distribution (SFD) (More details are in Appendix A.4).

Let us first discuss the magnetic properties of 1.8 µm NPs. The as-deposited blanket thin film is shown in Fig. 4.3(a). At a low magnetic field, the total magnetization is approximately zero, which is expected from the antiferromagnetic coupling of the top and bottom CoB layers in the basic stack and nearly equal magnetic moment of the two CoB layers. A small remnant moment at zero field can be observed in the inset Fig. 4.3(a), this is due to a slight thickness difference of the CoB layers during sequential growth[64]. Increasing the external field leads to a abrupt magnetization switch of the layer as expected from PMA-SAF samples in the spin-flip regime (i.e. where the PMA is much larger than the RKKY coupling) when the field is applied along the easy-axis[97]. This field we term the switching field, which depends on $\mu_0 H_{rkky}$ and $\mu_0 H_c$. From the minor loop we can extract $\mu_0 H_{rkky} = 208 \pm 10$ mT and $\mu_0 H_c = 6 \pm 1$ mT for the blanket film.[§]

Let us now turn to the switching behavior of the patterned film of 1.8 µm NPs before release as shown in Fig. 4.3(b). Ideally, the magnetic properties of the blanket film are propagated to the patterned NPs, however, two main differences can be observed; (1) $\mu_0 H_c$ has increased from 6 mT to 102 mT, and the switches are smeared out in the field, where the SFD has increased from 11 mT to 19 mT. (2)

[§]The method to determine the error of $\mu_0 H_c$ is described in Appendix A.5

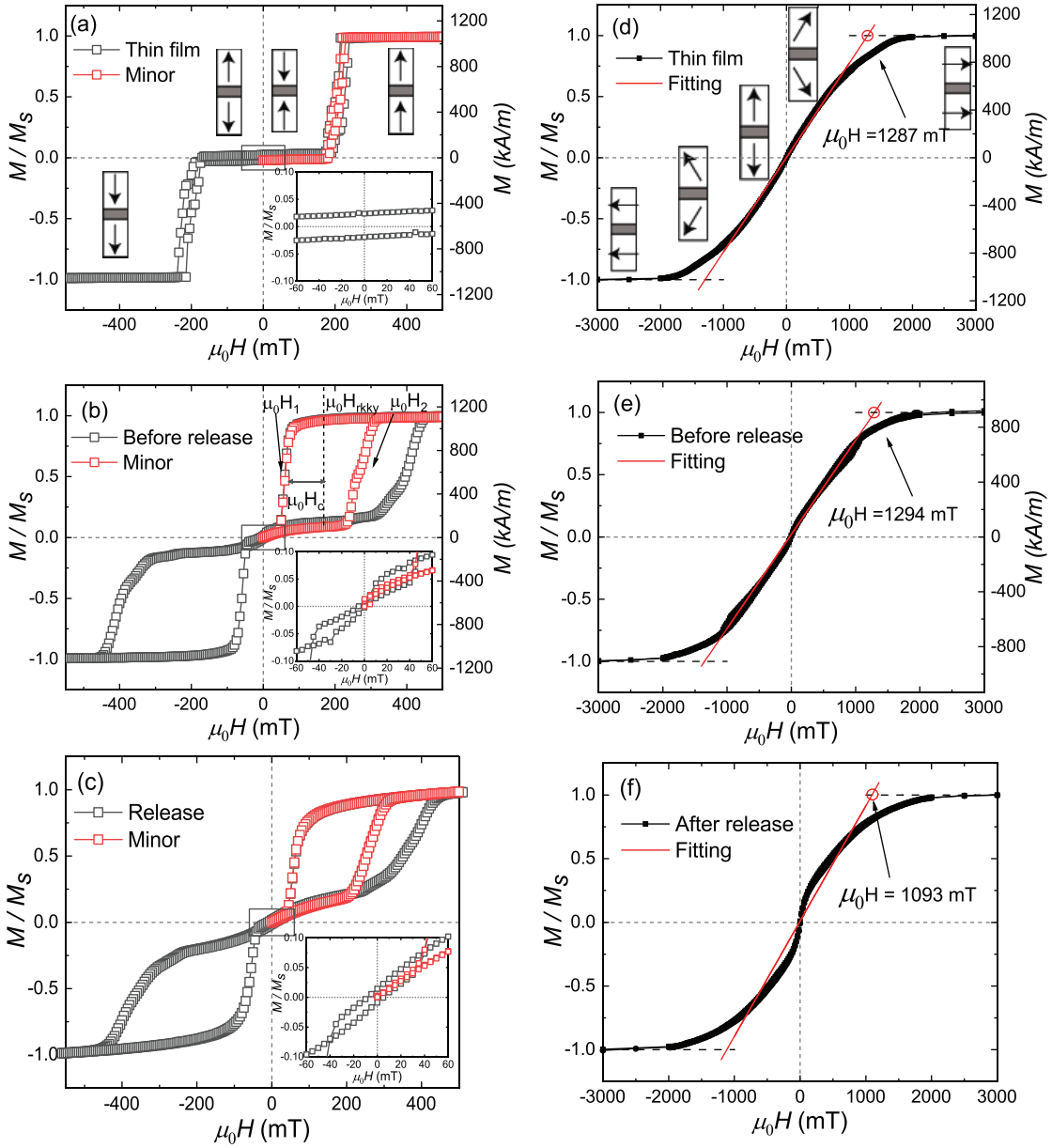

Figure 4.3: Hysteresis loops of the 1.8 µm NPs measured through SQUID. The left column contains the hysteresis loops measured along the easy axis for (a) the as-deposited thin film (b) before release and (c) release in water and dried on a Si substrate. The inserts in (a-c) show the zoom-in region of the black box near the origin of the loop. The right column includes the hysteresis loops along the hard plane for (d) the as-deposited thin film (e) before release, and (f) after release. The arrows indicate the direction of the magnetization of the top and bottom ferromagnetic layers.

The coupling field $\mu_0 H_{rkky}$ has reduced from 208 mT to 165 mT. The first observation can be explained by the dominant magnetic reversal mechanism (nucleation vs domain wall propagation[102,103]) which for these PMA-SAF films typically depends on the number of defects per surface area. Reducing the area of the object (patterning), the chance of finding a defect per platelet reduces, hence this leads to the increase of the $\mu_0 H_c$. Moreover, the sample area probed in the SQUID is around 4x4 mm^2 containing $\sim 1.5\times 10^6$ particles. The hysteresis observed is an ensemble response of all the NPs in the sample, from which the distribution of switching fields can be explained. The change in coupling field $\mu_0 H_{rkky}$ has been observed before and is attributed to processing induced changes[86]. Despite these differences, the typical SAF properties namely two distinctive switches and the well defined antiferromagnetic state at zero applied field are observed, which are similar to the blanket thin film. The saturation magnetization (M_s) of the platelets is 1067 kA/m and 1118 kA/m for the blanket and patterned film, respectively (see Fig. 4.3(a) and 4.3(b)). The similar values indicate that the fabrication process does not change the magnetic properties significantly.

Let us now concentrate on the hysteresis loop measured on the released platelets as shown in Fig. 4.3(c).[¶] Note the value of magnetization is not included in Fig. 4.3(c) and (f), as we cannot determine the magnetization without knowing the exact volume of magnetic materials. Overall the observed response is similar to the NPs before release. However, the hysteresis loop becomes more slanted and there is a slight increase in the SFD from 19 mT to 22 mT, which is speculatively attributed to a distribution in the angle of alignment of the dried-in platelets relative to the applied field direction and possibly stray fields of piled up platelets (see also Fig. 4.2(c) where many platelets piled on top of each other). Overall, it is clear that the 1.8 µm NPs before and after release keep their antiferromagnetic state at a low magnetic field and switch at high applied fields. The similar $\mu_0 H_{rkky}$ and $\mu_0 H_c$ indicate that the final release step does not degrade the SAF properties (more details are in Appendix A.3). On comparing the blanket film to the final released particles, a significant increase of the coercive field $\mu_0 H_c$ and a broader SFD are observed, which we attribute to the well-known size effect of patterning PMA films[88].

[¶]The details of SQUID measurement are shown in Appendix A.4

We will now move on to discuss the PMA of the NPs, which is the key factor of effective torque transduction[132]. To demonstrate the PMA of the NPs, the hard-plane hysteresis loops are shown in the right column of Fig. 4.3. In Fig. 4.3(d) a well defined hard-plane loop is observed typically for a PMA-SAF full film. At zero field, the magnetization of the layers points antiparallel to each other leading to zero net magnetization. With increasing absolute field, the magnetization of the top and bottom CoB layers are tilted towards the applied field. Further increasing the field, the magnetizations tilt more and finally saturate. In Fig. 4.3(e) a shoulder appears around 1 T and a more hysteretic behavior is found, which we speculatively attribute to edge tilting of the magnetization of the individual islands (NPs) on the surface. In Fig. 4.3(f) the measurement is taken on an ensemble of redispersed NPs on a wafer, in this process the hard-plane relative to the field is not well defined as platelets are not all flat on the surface as can be seen in the inset of Fig. 4.2(g). Hence, as expected a high slope around zero field and a more curved approach to saturation is observed due to the different field-alignments to the hard-axis of individual NPs in the ensemble. Here we define $\mu_0 H_{sat}$ as the saturation field, which is the crossing point of the saturated state ($\frac{M}{M_s} = 1$) and a linear fit of the data from -1000 mT to 1000 mT. To achieve the saturated state, the applied field should be large enough to overcome both the PMA and the RKKY interaction, from which $\mu_0 H_{sat}$ can be defined as $\mu_0 H_{sat} = \mu_0 H_k + 2\mu_0 H_{rkky}$, where $\mu_0 H_k$ is the effective PMA field of the magnetic layer[23]. The effective perpendicular anisotropy energy (K) is given by $K = \frac{H_k M_s}{2}$. Both $\mu_0 H_{rkky}$ and M_s are obtained from the easy-axis hysteresis loops. From the equation above, the K for the thin film sample, the NPs before release and after release are $(4.7 \pm 0.4) \times 10^5$, $(5.4 \pm 0.5) \times 10^5$ and $(4.3 \pm 0.4) \times 10^5$ J/m^3, respectively. We attribute the difference in K of NPs before and after release to a spread in the alignment of the NPs relative to the applied magnetic field after drop-casting and drying. This directly affects the shape of the hysteresis loop where a reduced saturation field is to be expected. Overall the relatively small spread of $K \approx 15\%$ denotes that the PMA is maintained during fabrication.

After discussing 1.8 µm SAF NPs, let's now examine the magnetic properties of 120 nm NPs depicted in Fig. 4.4. First, we observe that all three samples exhibit SAF properties (see Fig. 4.4(a-c)). The $\mu_0 H_{rkky}$ is 197 ± 6 mT for blanket film and

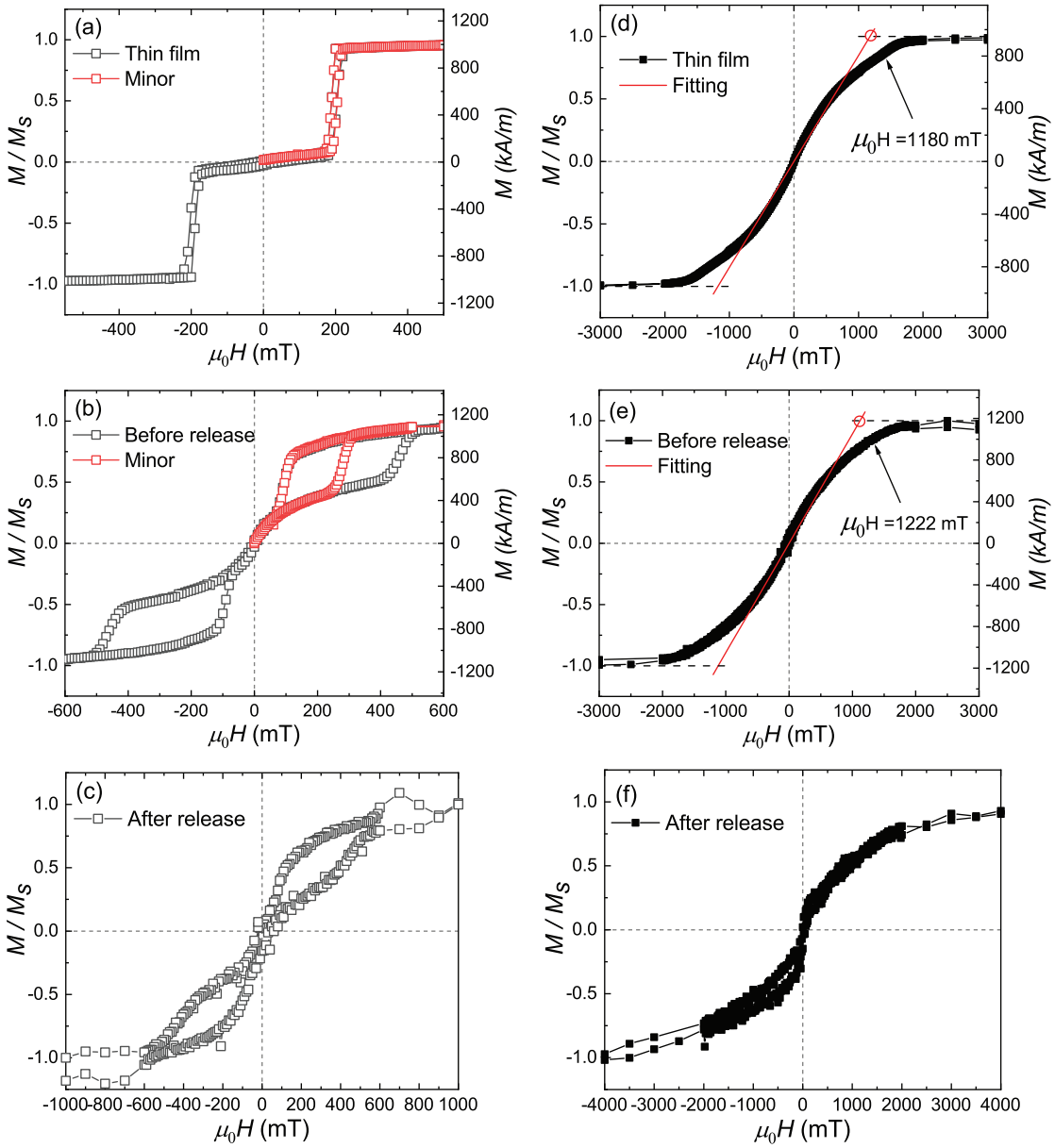

Figure 4.4: Hysteresis loops of the 120 nm NPs measured through SQUID. The left column contains the hysteresis loops measured along the easy axis for (a) the as-deposited thin film (b) before release and (c) after release. The right column includes the hysteresis loops along the hard plane for (d) the as-deposited thin film (e) before release, and (f) after release.

189 ± 8 mT for NPs before release. After patterning, the $\mu_0 H_c$ increased from 8 mT (blanket film) to 94 mT (before release). It is clear that the $\mu_0 H_{rkky}$ and $\mu_0 H_c$ of 120 nm NPs have similar values compared to the 1.8 µm NPs, and their changes

follow the same trend. The main difference is observed in the hysteresis loop of the released sample (see Fig. 4.4(c)), where the switching fields are observed to be slanted and have a wider spread. This is due to the ill defined arrangement of dried NPs on the substrate (see Fig. 4.2(g)). This phenomenon is also reflected in the hard-plane hysteresis loop of released 120 NPs as shown in Fig. 4.4(f), where the embedded switching behavior can be observed. Due to the misalignment, it is hard to quantitatively determine the $\mu_0 H_{rkky}$, $\mu_0 H_c$ and K of released 120 nm NPs. Moving now on to consider the PMA of 120 nm NPs during fabrication, which we calculate from the hard-plane hysteresis loop shown in Fig. 4.4(d-f). Here we do not include the K of the released NPs. The K values for the thin film sample and the NPs before release are $(4.1 \pm 0.4) \times 10^5$ and $(4.7 \pm 0.4) \times 10^5$ J/m^3, respectively, which are comparable to the values of 1.8 µm SAF NPs. Based on the hard-plane loop and the fact that the released step does not degrade the magnetic properties, although we cannot directly obtain the K of released NPs, we can conclude that the PMA of 120 nm NPs remains at a high value before release and we expect that the high PMA remains even after the release step, which we will address in future work. In summary, after fabrication 120 NPs show SAF properties and the PMA does not decrease .

4.4 Summary

In conclusion, we show that SCIL can be used to fabricate PMA-SAF based disc-shaped platelets with a uniform diameter in the micrometer and sub-micrometer range. After fabrication, both 1.8 µm and 120 nm NPs maintain their high PMA for high torque applications. A change in the magnetic response is observed which can be explained by the well-known change in the magnetic switching behavior when the area of PMA-SAF films changes. Our results pave the way for using SCIL imprint for the large-scale production of magnetic nanoplatelets using a subtractive method.

5

Optical Monitoring of the Magnetization Switching of Single Synthetic Antiferromagnetic Nanoplatelets with Perpendicular Magnetic Anisotropy

Synthetic antiferromagnetic nanoplatelets (NPs) with large perpendicular magnetic anisotropy (SAF-PMA NPs) hold significant promise for future applications in local mechanical torque-transfer, such as in biomedicine. Despite their potential, the nanoscale mechanisms governing their magnetization switching remain poorly understood. In this study, we employ a rapid, single-particle optical technique that transcends the diffraction limit to measure photothermal magnetic circular dichroism (PT MCD). Utilizing this method, we investigate the magnetization switching behavior of individual SAF-PMA NPs, each with a diameter of 122 nm and a thickness of 15 nm, as a function of the applied magnetic field. Our analysis delineates the disparities between the switching field distributions of large NP ensembles and single NPs. Notably, single-particle PT MCD enables us to examine the spatial and temporal heterogeneity of the magnetic switching fields at the level of individual NPs. The insights garnered from this research are anticipated to enhance our understanding of dynamic torque transfer in biomedical and microfluidic applications.[*]

[*]This chapter has been accepted for publication in *ACS Photonics*: Adhikari, S., **Li, J.** and *et. al.*[141]

5.1 Introduction

Magnetic nanoparticles have shown promising applications in biomedicine.[11,63,64,127,130] Among magnetic nanoparticles, synthetic antiferromagnetic (SAF) systems with a large perpendicular anisotropy (PMA) are of interest in various nanoscale torque-transfer related applications[23,62] due to their large magnetic and shape anisotropy. The SAF structure is composed of two ferromagnetic layers which are antiferromagnetically coupled by a spacer layer through the Ruderman-Kittel-Kasuya-Yoshida (RKKY) interaction.[77–79] In this case, the structure shows a zero net magnetic moment at low applied magnetic fields. This specific feature of the SAF-PMA system prevents aggregation of nanoparticles in solution. With varying magnetic field, the NPs switch from antiparallel (AP) to parallel (P), which we term the "on" field B_{on} switch or vice-versa, which we term the "off switch" B_{off} (see Fig. 5.1c). Note that, by magnetization switching, we refer to magnetization switching under an applied magnetic field, and not to optical switching of the magnetization.

Knowing the switching fields (B_{on} and B_{off}), which consist of the RKKY coupling field B_{rkky} and a stochastic coercive field B_c, needed to magnetically (de-)activate the NPs is a key requirement. Several reports[86,127] have found that ensembles of PMA-SAF nanostructures are characterized by large switching field distributions (SFD) reflecting the degree of particle-to-particle heterogeneity of their magnetic properties, where a well-defined B_{on} and B_{off} and narrow SFDs are preferred for applications. The broad SFDs are understood by considering the switching mechanism of ultrathin PMA nanostructures, assigned to stochastic thermally activated nucleation of a small magnetic domain followed by fast domain wall propagation.[102,142,143] These nucleation centers, which have variable density and broaden the SFD, are typically defects in the nanostructure and fabrication-induced defects. Moreover, here we speculate that the dipolar field contribution to B_{on} is different and large, compared to its contribution to B_{off}, leading to differently distributed B_{on} and B_{off} magnetic switching fields which we can conveniently probe at the single-particle level using PT MCD.

To understand the switching mechanism and broad SFDs of PMA nanostructures, measurements on a single-particle level are essential. However, most easy ac-

cessible characterization techniques which address the SFD are so far based on analyzing hysteresis loops measured on millions of particles simultaneously, so as to attain a sufficient signal-to-noise ratio.[144–147] There are a few techniques, e.g. micro-SQUID,[148,149] differential phase contrast and electron holography in transmission electron microscopy[89,90], which have been reported to measure SFDs at the nanometer scale. However, these techniques require demanding experimental conditions which are costly and/or complex in design. Recently, Spaeth *et al.*[124] reported a simple optical technique, photothermal magnetic circular dichroism microscopy (PT MCD), which presents the sensitivity required to measure the magnetization of single magnetite nanoclusters with a diameter of about 400 nm. PT MCD is based on the polar magneto-optical Kerr effect (MOKE)[42] and related to the imaginary part of the dielectric susceptibility. It measures the differential absorption of left- and right-circularly polarized light by a single magnetic nanoparticle. Very recently, the sensitivity of PT MCD was improved sufficiently to measure the hysteresis loops of single 20 nm magnetite nanoparticles.[150]

In contrast to previous reports on single synthetic magnetic nanoparticles, in this report, we use PT MCD to study the switching behavior of 32 individual single top-down nano-fabricated PMA-SAF NPs with a diameter of 122 nm and a thickness of 15 nm. We compare these signals with ensemble-based SQUID measurements to provide detailed insight into the variation of magnetic properties from NP to NP. Previously the polar-MOKE effect on a single-particle level was reported on NPs with 2 µm diameter[62], which are more than two orders of magnitude larger in volume than our particles. Due to the high sensitivity of our PT MCD technique, we are able to measure the full magnetization-switching curve on each individual 122 nm particle using optical microscopy. We then compare the statistics of the switching events at the single-NP level, and observe a difference between upon AP→P (on-switching) and P→AP (off-switching). This difference is washed-out in the ensemble measurement. We speculatively attribute this difference to the presence of a dipole field contribution in the on-switching which is not present in the off-switching. The switching fields are also found to be broadly distributed among individual nanoplatelets indicating spatial heterogeneity. Moreover, a small difference is expected due to the temporal character of the data acquisition; here the SQUID measurement was slow (~hour) compared to PT MCD (~minute) (See

details in Appendix B.4). To address these differences further, we compare 15 successive loops on one NP to study the temporal heterogeneity (stochasticity) of the switching process. We again observe a difference between the on- and off-switch, although it is less pronounced. Such a distinction between spatial and temporal heterogeneity can only be obtained from single-particle measurements, because these two sources or heterogeneity are averaged out in ensemble measurements.

In this report, we show that single-particle PT MCD enables us to study magnetization properties of single magnetic nanoplatelets. We have found that magnetic switching fields are broadly distributed among individual nanoplatelets and also stochastic in nature, indicating spatial and temporal heterogeneity. In addition, the distribution of on- and off-switching fields are different, which we speculatively attribute to a dipolar contribution.

5.2 Methods

The NPs used in the study consist of the following film stack: Ta(4)/Pt(2)/$Co_{80}B_{20}$(0.8)/Pt(0.4)/Ru(0.8)/Pt(0.4)/$Co_{80}B_{20}$(0.8)/Pt(2)/Ta(4) with thickness in nm indicated between parentheses (total thickness 15.2 nm). The stack was fabricated through magnetron sputter deposition on Si substrates and patterned via substrate conformal imprint lithography (SCIL) and a lift-off procedure into a liquid environment (see Appendix B.1). The NPs dispersed in solution are termed "released" and the NPs which are still attached to the substrate, i.e., before release, are termed "unreleased".

SQUID magnetometry was used to obtain the hysteresis loop of unreleased NPs (Fig. 5.1b), where an ensemble average of a total of $\sim 10^6$ SAF NPs was measured (see Appendix B.3). Note that the sample of unreleased NPs was used only for SQUID, not for the single-particle PT MCD measurements. During the measurement, a magnetic field was applied along the normal of the NPs at 400 K (the temperature of 400 K is chosen to match the temperature of single-particle PT MCD measurements). A minor loop (see the red data set in Fig. 5.1c) was measured, where the samples were first saturated in a positive field, the magnetic field was then decreased to zero and swept back to the positive saturation field. From the minor loop, the RKKY coupling field (B_{rkky}) is defined as $\frac{B_{on}+B_{off}}{2}$ and the

coercivity (B_c) is defined by $\frac{B_{on}-B_{off}}{2}$. B_{on} and B_{off} are the switching fields from AP to P (on-switch) and from P to AP (off-switch), respectively, as depicted in Fig. 5.1c.

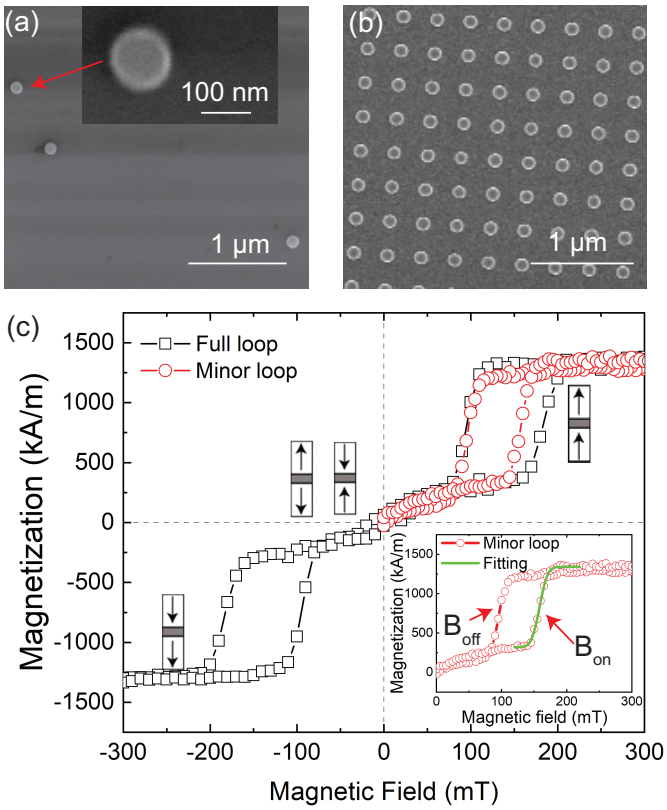

Figure 5.1: (a) SEM image of the released SAF NPs spin-coated on a silicon substrate. The released SAF NPs were used in PT MCD measurements. (b) SEM image of unreleased SAF NPs on the silicon wafer used for fabrication. The unreleased sample was used in SQUID measurements. The bright ring at the edge of each single particle in the SEM image is due to redeposition during fabrication and is an artifact due to an inclined electron exposure leading to enhanced secondary electron generation. (c) Hysteresis loops of the NPs measured with a SQUID at 400 K. The black squares represent the full hysteresis loop (i.e., major loop). The inset shows the fitting of the minor loop through an error function, from which we obtain the switching field and SFD (for details, see Appendix B.4). The red data set represents the minor loop. The black arrows indicate the direction of the magnetization of the top and bottom ferromagnetic layers constituting the SAF. The red arrows indicate on- (B_{on}) and off- (B_{off}) switching fields of the minor loop. The difference between the major and minor loops is due to the hysteretic effect of magnetization switching.

In PT MCD measurements, a heating laser was used to illuminate the NPs. The

released NPs were dispersed on a glass substrate by spin-coating (see Fig. 5.1a) and immersed in hexadecane, which was the contrast medium for photothermal imaging.[122] The difference in the absorption of the left- and right-circularly polarized light leads to a change of the refractive index of the medium which is detected by the probe beam. The measured circular dichroism (CD) signal is defined as $\sigma_L - \sigma_R$, where σ_L and σ_R are the absorption cross sections of the NP for left- and right-circularly polarized light, respectively.[151] The magnetic Circular Dichroism (MCD) signal is the CD signal due to the polar magneto-optical Kerr effect. Therefore, it reports on the particle's absorption and its changes with magnetic field, and it depends only on the imaginary part of the optical susceptibility. The so-called g_{CD} factor is defined as the CD signal normalized by the photothermal signal (see Appendix B.6). Minor loops in both negative and positive fields are measured (more details are in Appendix B.11). As the particles were heated with light, their temperature was estimated to be about 390 K (see further details in Appendix B.7).

5.3 Results and Discussion

SEM images of released and unreleased NPs are shown in Fig. 5.1a and b, respectively. The NPs have an average diameter of 122 ± 4 nm (see Fig. B.1). The unreleased NPs are used for the ensemble SQUID measurements and the released NPs for the PT MCD measurements. The SQUID measurements of major and minor loops in Fig. 5.1c show the typical SAF behavior.[63,64,78,127] At a low magnetic field, the total magnetization is zero, due to the antiferromagnetic coupling of the top and bottom CoB layers of nearly equal magnetic moments. Increasing the external field leads to an on-switch at B_{on} of one of the CoB layers, giving $B_{rkky} = 127$ mT and $B_c = 32$ mT, calculated from the minor loop. We observe a gradual switch in both the major and the minor loops. This gradual switch reflects the SFD of ~10^6 single NPs. By fitting the (minor) hysteresis loop with an error function (see Fig. 5.1c), we extract the SFD of the ensemble (more details are in Appendix B.4). The center value of the fits represent the switching fields B_{on} and B_{off}, (158 ± 10) mT and (95 ± 10) mT, respectively (see Table 5.1). Note that the difference between the major and minor loops as shown in Fig. 5.1c is due to hysteresis.

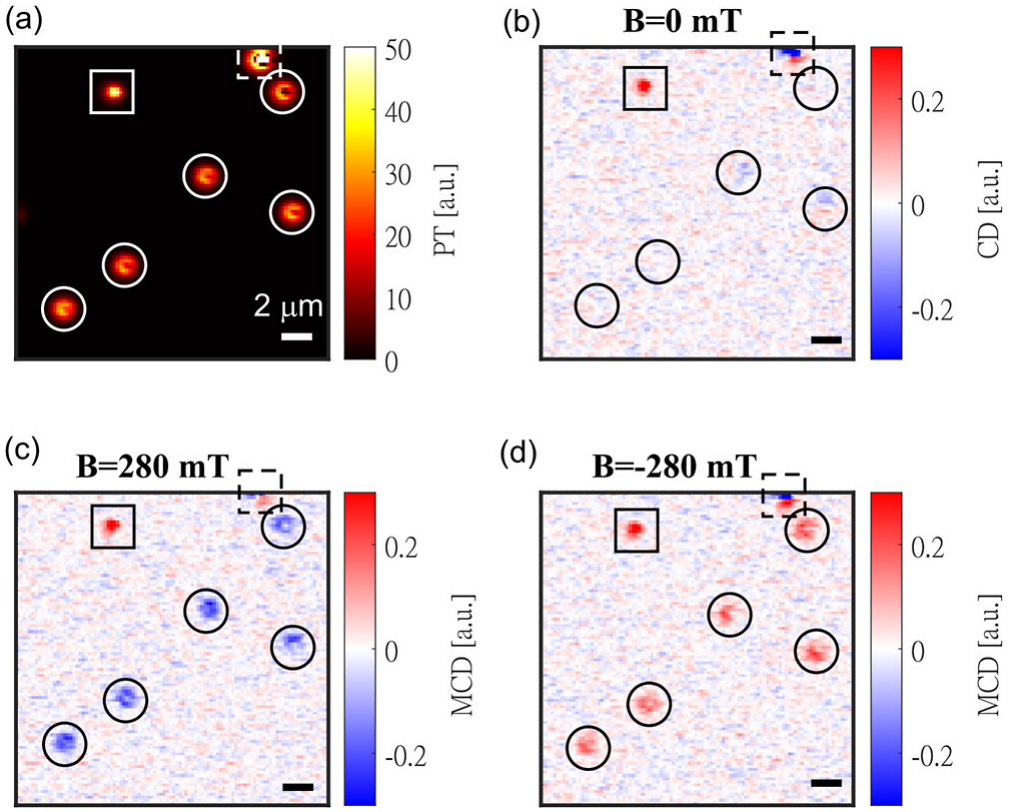

Figure 5.2: (a) PT imaging of magnetic NPs. Single NPs are identified by the homogeneous magnitude of their PT signals (solid circles). An aggregate, marked with a dashed square, has much stronger PT signal. (b) CD imaging of magnetic NPs in the absence of an applied magnetic field (B = 0). Single NPs show very weak CD signals at $B = 0$ mT. MCD imaging of magnetic NPs at (c) $B = 280$ mT and (d) $B = -280$ mT. The MCD signal flips sign upon inversion of the magnetic field's orientation. The particle marked with a solid square shows no flip of MCD signal with flip of magnetic field orientation. This particle is probably not a SAF particle. The scale bars are 2 µm.

Figure 5.2a shows a PT image of single released magnetic NPs spin-coated on a glass substrate. Single magnetic NPs are identified by the magnitude of their PT signals, which falls in a very narrow range (see histogram of photothermal signals in Fig. B.3). These single NPs are marked with solid circles in Fig. 5.2. Their point-spread-functions (PSF) are very similar for all NPs measured, as expected from their narrow size distribution. We attribute the complex shape of the PSF of a single platelet to interference between probe waves scattered by the thermal lens and by the particle itself.[122] We found a few aggregates of NPs, which we identified by their stronger PT signals, as indicated in Fig. 5.2a with a dashed

Table 5.1: Switching ields (B_{on} and B_{off}) and their distribution, B_{rkky} and B_{c}, measured by SQUID and PT MCD

	SQUID at 400 K	PT MCD at ∼390 K
B_{on} (mT)	158	114
SFD of B_{on} (mT)	10	25
B_{off} (mT)	95	61
SFD of B_{off} (mT)	10	5
B_{rkyy}	127	88
B_{c}	32	27

square. Such aggregates were not considered in the analysis of our results. MCD images of the same NPs in applied magnetic fields of $B = 0$ mT, $B = 280 \pm 6$ mT and $B = -280 \pm 6$ mT, are shown in Fig. 5.2(b-d), respectively. Single NPs show weak CD signals in zero applied magnetic field (see Fig. 5.2b), indicating that they are structurally symmetric and present zero net magnetization. Under a high magnetic field where NPs are saturated ($B = 280 \pm 6$ mT and $B = -280 \pm 6$ mT), a strong MCD signal is observed as shown in Fig. 5.2(c-d). The MCD signal of the NP changes in sign upon inversion of the magnetic field, which distinguishes it from CD originating from shape and/or composition defects. The MCD sign depends on the wavelength of the light. At 532 nm, it is negative for a positive applied field, in our sign convention (see Section 5.2). We also observe few particles (e.g., marked by a solid square in Fig. 5.2) which show strong CD signals in the absence of an applied magnetic field but do not show any reversal of the CD signal with magnetic field. These particles were probably not single SAF NPs and were not considered in our later analysis. Identification and distinguishing of single SAF NPs from aggregates and other types of magnetic nanoparticles are advantages of the single-particle technique. The variation of the MCD signal with the applied field opens up the possibility to measure hysteresis loops on a single-particle level.

We now consider the hysteresis loops of single magnetic NPs, as shown in Fig. 5.3(a-d). A total of 32 single magnetic NPs were measured (see Fig. B.6 and Fig. B.7). The first thing we observe is that all 32 single NPs show characteristic PMA-SAF behavior i.e., the AP to P switch at B_{on} and from P to AP at B_{off} and zero MCD around zero applied field. In contrast to the ensemble hysteresis

loop, we now find that all switching events observed are sharp as observed in the blanket films samples (see Fig. B.2), in agreement with the proposed switching mechanism of a single NP, which starts with domain nucleation, and is followed by propagation of the domain wall.[86] This is a new insight compared to the SQUID measurements, where the broad SFD reflected the distribution of the ensemble (i.e., particle to particle SFD), but provided no clear indication as to the sharpness of each individual switching event (i.e., of the single-particle SFD). Such a distinct information is only possible to obtain from single-particle measurements. The apparently higher noise observed at low fields in the hysteresis loop is a measurement artefact due to the denser sampling at low fields than at high fields (for details see Appendix B.13, Appendix B.14 Figs. B.8 and B.9).

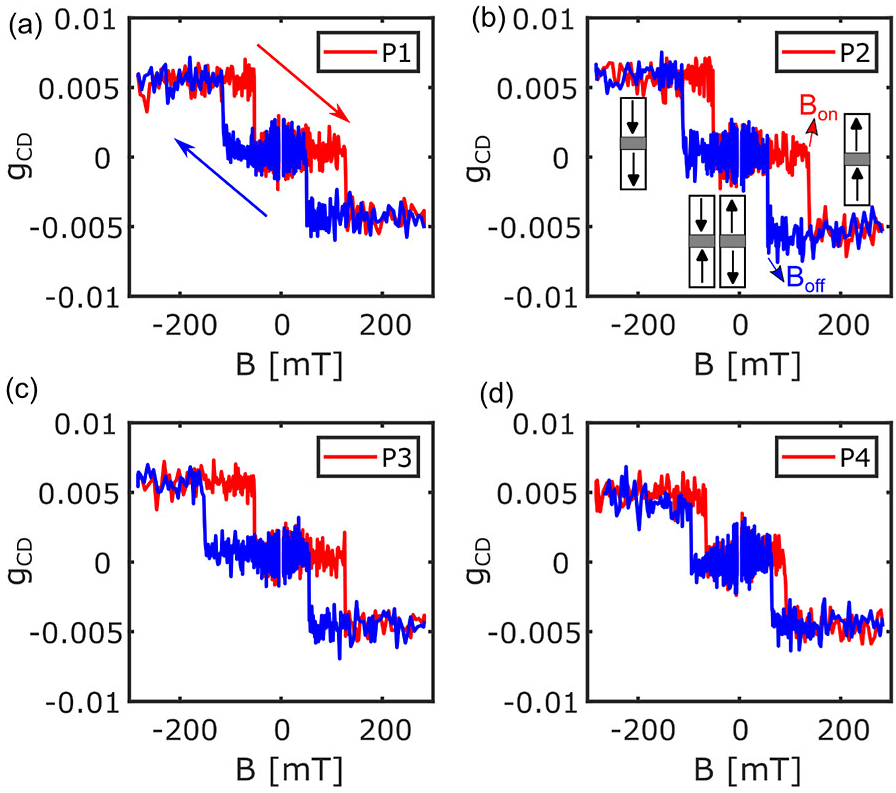

Figure 5.3: (a–d) Full magnetization curves of four single magnetic NPs, labeled as P1, P2, P3, and P4. Schematic of spin-flip is shown in (b) with on- and off-switching fields labeled with B_{on} and B_{off}.

The histograms taken from 32 NP measurements of the PT and g_{CD} factors at saturation are presented in Fig. B.3(a-b). They show comparatively narrow dis-

tributions, consistent with the high monodispersity of NPs (see Fig. 5.1 and Fig. B.1). This means that all NPs have similar g_{CD} factors of about 5×10^{-3} at saturation (see Fig. B.3b). The MCD signal arises mainly from the magnetic layers of the NP, whereas the PT signal arises from the absorption of both the magnetic and non-magnetic layers. Simulations discussed in the Appendix B.16 suggest that only ~8.7 % of the total light is absorbed in the two CoB layers. Therefore, normalization of the g_{CD} factor on the total CoB absorption would yield a value of $(5 \times 10^{-3})/0.087$ i.e., 5.7×10^{-2}. In a previous report[124], we have found that the saturation g_{CD} factor of magnetite nanoparticles was ~1×10^{-2}. This difference can be related to the difference in the saturation magnetization (M_s), however, due to the complexity of magneto-optic interactions[152] the absolute mapping of the g_{CD} factor to M_s is beyond the scope of this study.

We now compare the statistics of the switching behavior of the 32 single NPs measured by PT MCD with ensemble SQUID measurement. The switching fields B_{off} and B_{on} of 32 single NPs and their histograms are shown in Fig. 5.4(a-b). The mean values and distribution of the histograms of B_{on} and B_{off} are summarized in Table 5.1. The histograms of B_{rkyy} and B_c are shown in Fig. 5.4(c-d), with mean values in Table 5.1.

In agreement with our SQUID measurements, PT MCD measurements of single NPs show that these switch at different fields (see Fig. 5.4(a-b)), giving rise to a broader SFD for B_{on} (25 mT) as compared to the SQUID (10 mT). The SQUID measurements were performed on a 4×4 mm^2 piece of wafer, whereas the PT MCD measurements were done on released NPs from a full 2-inch wafer. We thus expect more inhomogeneity and a broader SFD for the released NPs, because they originated from the whole wafer and sampled the full inhomogeneity of the deposition process. We attribute the difference of the absolute values of B_{off}, B_{on} and B_{rkky} between PT MCD and SQUID to the error in the estimated temperature of the platelets in PT MCD measurements and/or to small differences in the calibration of the magnetic field (estimations of temperature in PT MCD and the effect of temperature on switching fields are given in the Appendix B.8). In addition, the difference may arise due to the change in strain in the released particles by the lift-off process compared to the unreleased particles. The measured B_c in PT MCD (27 mT) and SQUID (32 mT) match well as B_c is a relative

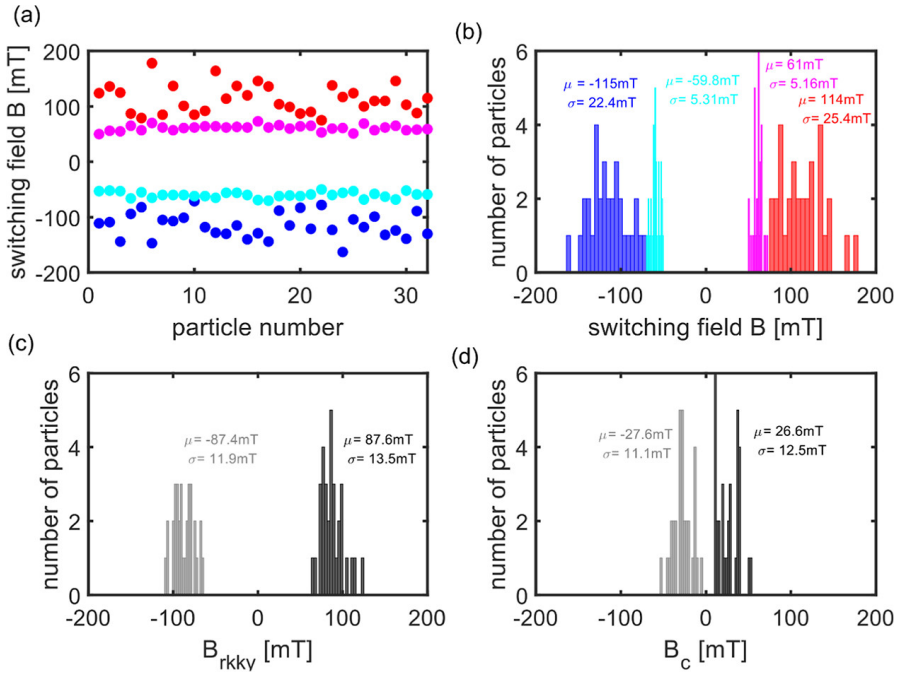

Figure 5.4: (a) Low positive (magenta) and negative (cyan) switching fields and high positive (red) and negative (blue) switching fields for each particle. (b) Histograms of all the switching fields. (c) Histograms of positive (black) and negative (gray) coupling fields Brkky i.e., $(B_{on}+B_{off})/2$ where B_{on} and B_{off} are high and low switching fields, respectively. (d) Histogram of positive (black) and negative (gray) coercive fields Bc, i.e., $(B_{on}\text{-}B_{off})/2$. Mean values ($\mu$) and standard deviations (σ) of the histograms are shown in the inset.

measurement of the two switching fields.

Interestingly, the SFD is much broader for B_{on} (26 mT) than for B_{off} (5 mT) in the single-particle PT MCD measurements, whereas they are similar (both 10 mT) for the SQUID measurements. This can be speculatively explained by the dipole fields in the AP configuration as schematically shown in Fig. B.1, and by the role of residual nucleation embryos in the reversal mechanism of on- and off-switching.[153–155] When NPs switch from AP to P state (B_{on}), the dipole fields of the two CoB layers repel each other, leading to a canting of the magnetization at the edge of NPs, which, in-turn, assists domain nucleation. In the P to AP switching (B_{off}), the dipole fields are aligned and do not contribute to the nucleation process. In addition, irreversible nucleation embryos left over from former field cycles may further contribute to the SFD.[154] In contrast to PT MCD, the

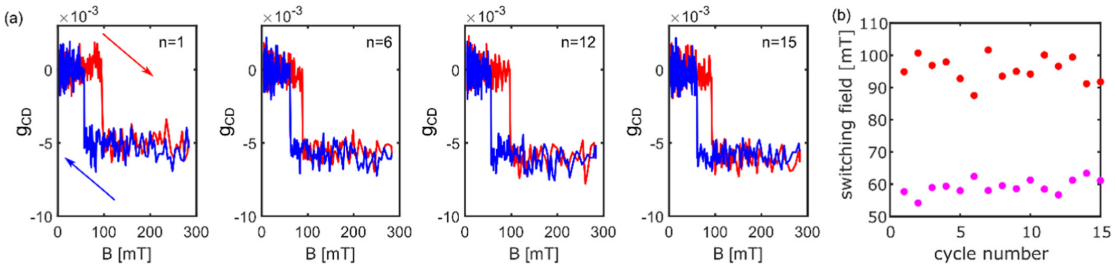

Figure 5.5: (a) Time-dependent minor loops of magnetization curves measured successively 15 times on the same single NP. Here, only the 1st, 6th, 12th, and 15th cycles are shown. (b) On- (red) and off- (magenta) switching fields measured for each cycle.

reduced B_{on} was not observed in SQUID, possibly because the effect is averaged out on a large number of NPs. Note that the dipolar interaction between NPs (not the interparticle dipole field) in both the PT MCD and SQUID measurements can be neglected since the dipolar field of neighboring NPs is very small (see the Appendix B.17). This difference needs further investigation. These findings however illustrate the power of single-particle measurements to reveal details of the single-particle switching properties, compared to ensemble studies.

In addition to the SFD measured on an ensemble of single particles, we also measured the same single particle repeatedly for 15 times. The minor loops of several cycles are shown in Fig. 5.5a. Both B_{off} and B_{on} fluctuate from cycle to cycle, as shown in Fig. 5.5b. We assign the temporal fluctuation of the switching field to the thermally activated stochastic domain nucleation process (the SFD is shown in Fig. B.10).[79] The mean values (standard deviations) are 59 ± 2 mT and 96 ± 4 mT for B_{off} and B_{on}, respectively. The cycle-dependent fluctuations of B_{on} are larger than those of B_{off}. The B_{off} fluctuations are similar to those found on the 32 different particles as shown in Fig. 5.4. However, the B_{on} fluctuations for the 32 NPs are much larger than for the single NP, implying that more disorder is found in the small ensemble of 32 NPs, which includes both spatial and temporal disorder. Thus, our PT MCD method enables us to distinguish spatial and temporal heterogeneity in the switching-behavior of magnetic nanoparticles.

5.4 Conclusions

In summary, we have shown that single-particle PT MCD is a very powerful technique to study the magnetization switching of single magnetic PMA-SAF NPs. The measured SAF properties of NPs and the narrow distribution of the PT MCD of NPs indicate that the PT MCD is a powerful probe of the magnetic behavior of individual NPs. Moreover, compared to SQUID, the spatial and temporal heterogeneity of the magnetic properties, especially the switching fields at the single-particle level, can be extracted from PT MCD. The SFD generated by averaging the switching field of many NPs via the PT method is found to be broad. In addition, the minor loops successively measured on the same NP vary moderately from cycle to cycle, confirming that the reversal process is indeed a thermally-activated stochastic process. We observed a difference in the magnetization switching from AP→P vs P→AP in the PT measurements, which was absent in the SQUID measurements. We speculatively attribute this difference to the dipole-field which assists reversal for AP→P (on-switching), but is absent for P→AP (off switch). Such details are washed out in ensemble measurements.

6

Tuning the coercivity of synthetic antiferromagnetic nanoplatelets with perpendicular anisotropy through tuning the Co_xB_{1-x} alloy composition

Synthetic antiferromagnetic (SAF) nanoplatelets (NPs) with perpendicular magnetic anisotropy based on archetype SAF structures e.g. Pt/Co/Ru/Co/Pt are of particular interest for torque-related bio-applications due to their large uniaxial magnetic anisotropy. However, when the diameter of the NPs is reduced, the magnetic properties change. For instance, the coercive field increases and starts to vary strongly from NP to NP in a batch due to an increased variation in the reversal probability dominated by local defects. In this study, we investigate how the concentration of Boron (B) in $Co_{1-x}B_x$ affects the switching properties of NPs, because the addition of B renders the Co layer amorphous and hence introduces more defects. Moreover, it reduces variations in local crystalline anisotropy making the magnetic properties of the NPs more soft. Specifically, we show that the coercivity of the NPs decreases with higher B concentration. This decrease is explained by two mechanisms; (i) the loss of interfacial anisotropy due to less Co-Pt hybridization at the Pt-Co interface and (ii) an increase in the surface's magnetic domain nucleation site density leading to a narrower distribution of the coercivity of an ensemble of NPs. This understanding will greatly help the field of NP-torque related applications as the spread in applied torque from the NPs to

their surroundings can be homogenized. *

6.1 Introduction

Synthetic antiferromagnetic nanoplatelets (SAF NPs) exhibiting perpendicular anisotropy (PMA) have garnered significant attention in torque-related applications, such as mechanical destruction of cancer cells[23,134,156], micro mixing[157], and cell manipulation[158]. The SAF structure is comprised of multiple layers of ultra-thin film layers. Thin film structures, such as Co/Pt and Co/Pd, demonstrate high PMA owing to the strong hybridization of 3d-5d orbitals at the interface, which is the primary cause of effective torque transfer[23,74]. Through the Ruderman-Kittel-Kasuya-Yoshida (RKKY) interaction, two ferromagnetic (FM) layers can be anti-ferromagnetically coupled by a spacer layer to form a SAF[77–79] structure as shown in Fig. 6.1a. Consequently, the entire stack exhibits a zero net magnetic moment at a low applied magnetic field, but can be switched 'on' at moderate applied magnetic fields as shown in Fig. 6.1c. This allows for a threshold field where the NPs are activated and, when not aligned with this field direction will exert a torque on its surroundings due to the large PMA[85]. This threshold field is affected by the switching field (see Fig. 6.1c), which is the magnetic field required to switch the magnetization of the two ferromagnetic layers from antiparallel (AP) alignment to parallel (P) alignment[62].

One key factor that limits the application of SAF NPs is the increase in switching fields when the size of the NPs decreases leading to a large required external field to manipulate the NPs. The field required to activate these NPs can easily reach hundreds of milliTeslas due to the large intrinsic anisotropy field of PMA stacks. This will complicate e.g., bio-applications and research, which are often performed in microscopes where the application of large magnetic fields requires either specific permanent magnet arrangements which do not allow for varying the magnetic field magnitude or direction easily, or bulky electromagnets which require water cooling or cryogenic superconducting coils.

It has been shown that for such a PMA system, the coercivity field ($\mu_0 H_c$) and switching field distribution (SFD), i.e., the distribution of the coercive field in a

*This chapter has been accepted for publication in *Journal of Applied Physics*: **Li, J.** *et. al.*

batch of NPs, are higher compared to continuous films[127]. This is explained by a thermally activated reversal mechanism being dominated by a magnetic domain nucleation event followed by domain wall expansion[159,160]. Moreover, $\mu_0 H_c$ and SFD grow considerably as the nanostructure size decreases since fewer defects are present in the reduced area[105,161–163].

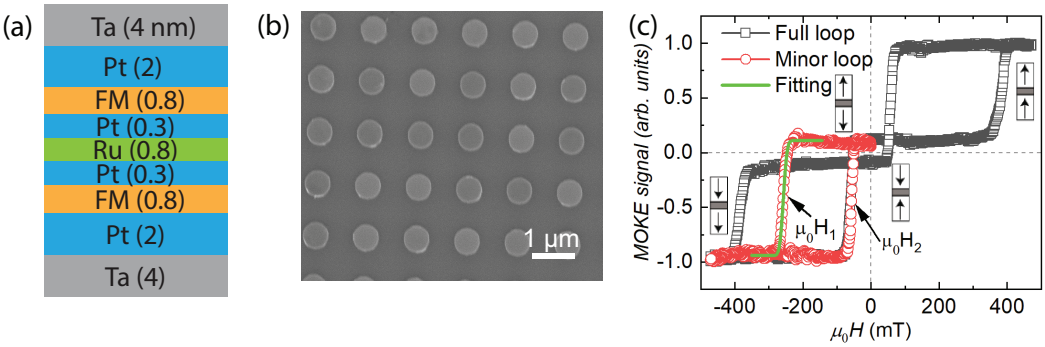

Figure 6.1: (a) The thin film stack used in this work. The ferromagnetic (FM) layer is $Co_{1-x}B_x$. (b) SEM image of 600 nm diameter SAF NPs. (c) A typical major and minor hysteresis loop of $Co_{80}B_{20}$ 5 µm diameter SAF NPs including a fit of the minor loop using an error function. Arrows indicate the relative magnetization configuration at every level of the loop.

To decrease the switching field, both the RKKY coupling field and the coercivity can be tuned. The RKKY coupling field can be reduced, for example, by changing the Ru layer thickness or inserting a Pt layer between the FM layer and the RKKY spacer layer[164]. Welbourne *et al.* reported the reduction in the switching field while keeping the AF state by using the second strongest AF coupling peak, combined with using a thin Pt layer to reduce the RKKY interaction[86]. However, due to a finite coercivity, it cannot be reduced too much, since this will render the NP ferromagnetic at zero applied external field; that is, the system would not switch 'off'. Moreover, introducing a Pt layer will also increase the PMA of the FM layers, thereby increasing the coercivity. The growing pressure during the sputtering of FM layers, which can affect the microstructure of layers, is also known to influence the coercivity and SFD[165–167]. For example, in Co/Pt thin film stack, higher pressure can cause larger coercivity[165]. Alternatively, it has been observed that ion irradiation through Ga^+, Ar^+ and He^+ can tune PMA and defect density, thus directly decreasing the coercivity[168–170], which might be

another interesting route to explore.

In this work, we show that by introducing Boron in the Co layer we can reduce the coercive field and reach a smaller SFD in a batch of NPs, while still maintaining a sufficient PMA as required for torque-related bio applications. Thin film samples are patterned into NPs ranging from 15 µm to 100 nm in diameter with different B concentrations. We compare batches of pure Co, $Co_{80}B_{20}$ and $Co_{68}B_{32}$. Using the Sharrock formalism[161] allows us to extract quantitative values for the PMA and nucleation (defect) site density and supports the claim that the decrease in $\mu_0 H_c$ and SFD can indeed be explained by a decrease in PMA and an increase in nucleation (defect) density leading to magnetically more homogeneous NPs batches that can be operated at lower applied magnetic fields.

6.2 Methods

In our previous work we showed that before and after releasing from the substrate, the switching behaviour of SAF NPs did not change[127]. Hence, we decided in this work to study the SAF NPs that are still on the substrate without losing generality for the released particles. To make this clear we will refer to these NPs as islands through the remainder of the paper. Arrays of islands with the stack Ta(4)/Pt(2)/$Co_{1-x}B_x$(0.8)/Pt(0.3)/Ru(0.8)/Pt(0.3)/$Co_{1-x}B_x$(0.8) /Pt(2)/Ta(4) as shown in Fig. 6.1a were used in our present work. These metallic stacks were deposited on Si substrates with native SiO_2 at room temperature through DC magnetron sputtering with an Ar pressure of 10^{-2} mbar. The base pressure of the sputtering chamber was maintained at 10^{-9} mbar. We then patterned arrays of islands with different diameters ranging from 15 µm to 100 nm via electron beam lithography with the resist MaN2403. In each array of islands, the inter-island distance is equal to the diameter. After patterning, the samples were etched through Ar ion beam milling followed by a lift-off process to remove the residual resist. The IBM process involved a sequential two-step etching process and was performed at an ion density of approximately 1200 µA/cm^2. Initially, etching was conducted at 90° for 2 minutes. This was followed by a subsequent etching at an angle of 20° for 60 seconds. Throughout this procedure, the resist MaN2403 was employed as the mask. The magnetic properties of the thin film

SAF samples were characterized using SQUID. To investigate the magnetization switching process of the SAF nanostructure, the magneto-optical Kerr effect in a polar configuration (pMOKE) at room temperature and with the field perpendicular to the plane was employed.

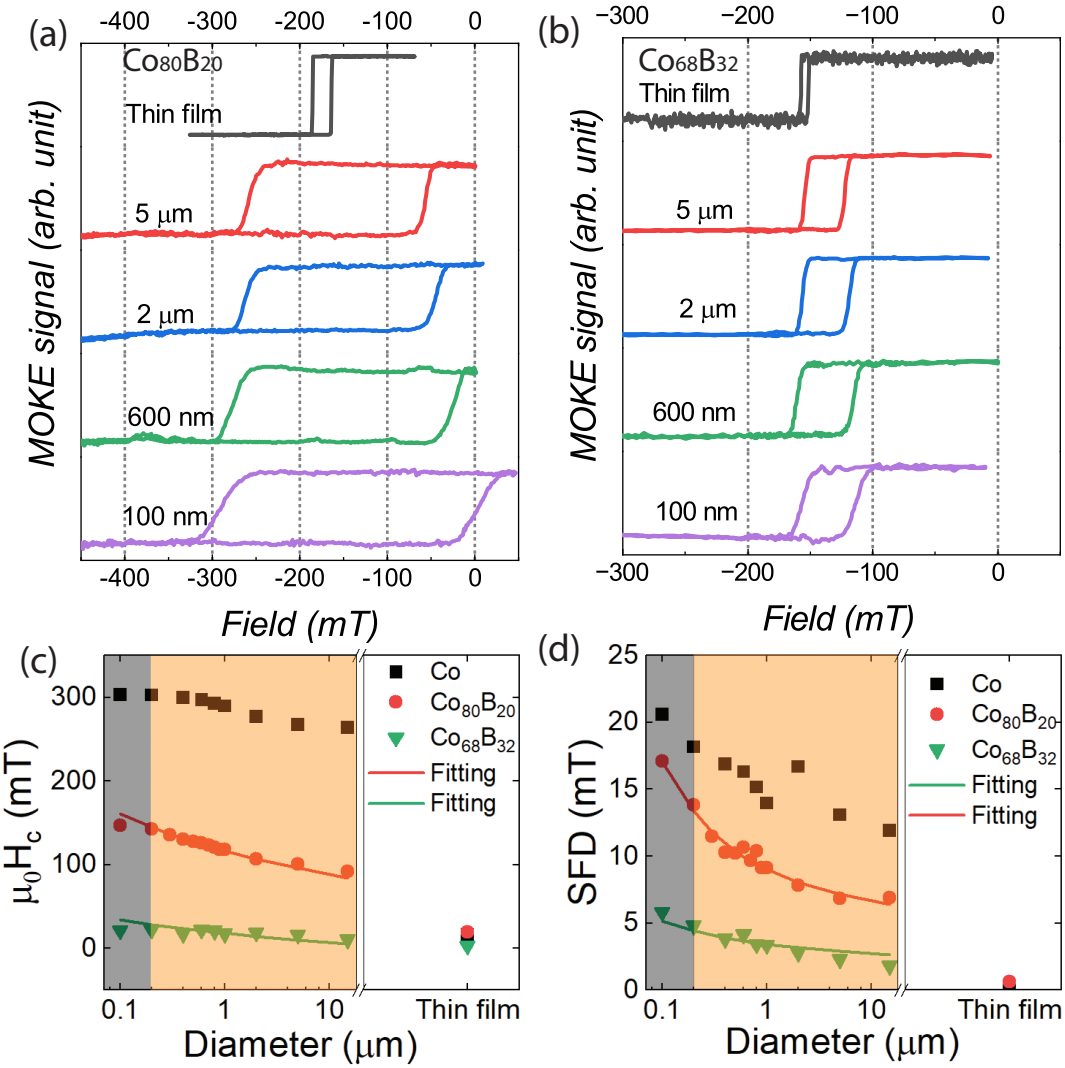

Figure 6.2: Minor hysteresis loop of (a) $Co_{80}B_{20}$ and (b) $Co_{68}B_{32}$ based thin film SAF stack and SAF islands with different diameters. (c) Coercivity as a function of diameter. (d) SFD as a function of diameter.

6.3 Results

In Fig. 6.1b a SEM image of a patterned sample with islands that have a diameter of 600 nm is shown (other sizes are shown in Appendix C.1). We have intentionally selected a relatively large inter-island distance to ensure that our study focuses on the intrinsic properties of the NPs without the confounding effects of dipolar coupling. The dipolar interaction between islands can be experimentally measured[171]. However, here we have only conducted a simulation on the dipolar field and found that the influence can be neglected (see Appendix C.3). In a liquid environment, where NPs are dispersed, the proximity of these NPs could lead to enhanced dipolar interactions, which potentially influence the switching field for application, however, such considerations are beyond the scope of this work.

A typical pMOKE hysteresis loop of $Co_{80}B_{20}$ based SAF islands, where the field is applied along the easy axis, perpendicular to the sample surface, is shown in Fig. 6.1c. At a low external field (<50 mT) the magnetization of the top and bottom FM layers is always aligned antiparallel, resulting in a zero net magnetic moment, preventing agglomeration of the NPs when released. It is important to note that in MOKE measurement the intensity of light reflected from the top and bottom FM layers differs. This arises because the light undergoes attenuation as it penetrates the material layers, resulting in a non-zero signal even at an antiparallel state in MOKE. SQUID measurements, shown in the Fig. C.4, confirm that the absolute value of the magnetic moment is zero at a low field. Increasing the external field leads to a switch as expected from PMA-SAF samples in the spin-flip regime[127]. In Fig. 6.1c, a notable difference is observed between the opening of the full loop (in black) and the minor loop (in red). This distinction arises because the minor loop specifically measures the magnetic switch of a single layer, namely the top layer in our study, whereas the full loop measures both layers. The difference between the full and minor loops indicates the divergence in the magnetic properties of the top and bottom layers, which is likely attributable to their distinct growth conditions—one layer being directly grown on Ta/Pt and the other on Pt/Ru. Such asymmetry is crucial as it potentially impacts the alignment of NPs in a liquid environment, a factor that must be considered in future applications[85]. More details regarding the full loop are available in Appendix C.8. This study primarily focuses on the analysis of the minor loop. From a minor loop the RKKY coupling field

($\mu_0 H_{RKKY}$), defined as $\frac{\mu_0 H_1 + \mu_0 H_2}{2}$, and the intrinsic coercivity ($\mu_0 H_c$), defined by $\frac{\mu_0 H_2 - \mu_0 H_1}{2}$ are extracted. Note that in the pMOKE measurement, the diameter of the used laser spot is approximately 137 µm (see Fig. C.2). Since a large number of islands are within the measured laser spot, the obtained signal reflects the collective switching behavior of these islands. We extract $\mu_0 H_1$, $\mu_0 H_2$ and the SFD by fitting an error function to the minor loop as shown by the green fit in Fig. 6.1c, where the SFD is defined as the width of the error function.

In Fig. 6.2(a-b), the minor loops of SAF blanket films and island arrays consisting of $Co_{80}B_{20}$ and $Co_{68}B_{32}$ with varying diameters are shown. All blanket films exhibit sharp switches as they are dominated by the reversal of a single most defective site and the consequent fast domain wall motion[159,172]. Upon patterning, a large increase in $\mu_0 H_c$ is observed as expected, while $\mu_0 H_{RKKY}$ remains rather constant and the switching field curves become slanted. This is because the reversal is dominated by the 'weakest' nucleation site located on each separate island. By 'weakest', we mean that these sites require the least external magnetic field to switch. Different 'weakest' sites result in varied fields across the islands[163]. Further proof of this can be found in recent measurements on released single SAF-PMA NPs where sharp switches (i.e. nucleation dominated reversal) were observed down to 120 nm diameter NPs[141]. For 100 nm diameter $Co_{80}B_{20}$ islands, a finite remanent magnetic moment is observed at zero field after scanning the field from negative saturation. This indicates that some islands did not return to the AF state at zero field. For these islands, the increase in the coercive field for a part of the probed ensemble is larger than the RKKY coupling field. For released NPs made from these islands, this means that some of them will exhibit a finite magnetization at zero field and this will cause NP aggregation which needs to be avoided for applications. This can be compensated by a higher RKKY coupling field in the basic stack at the cost of a larger activation field.

To further investigate the observed increase in $\mu_0 H_c$ and SFD, we examine the $\mu_0 H_c$ and SFD as functions of the diameter of different $Co_{1-x}B_x$ compositions as shown in Fig. 6.2(c-d). In the pink region, where the diameter is above 200 nm, both $\mu_0 H_c$ and SFD increase with decreasing island diameter. We attribute the increase in $\mu_0 H_c$ to the reduction in the number of nucleation centers on each island when the size decreases. The increased SFD indicates higher variation in

$\mu_0 H_c$ over the ensemble. However, as depicted in the grey area in Fig.6.2(c-d) when the size of the islands falls below 200 nm, this trend breaks. Here, $\mu_0 H_c$ shows slower increments or even decreases, while the SFD value keeps increasing. The slower increments or decreases in $\mu_0 H_c$ indicate that the nucleation density is higher on the islands smaller than 200 nm diameter, which is further confirmed by the higher SFD. We speculate that this behavior indicates the point at which edge vs. bulk nucleation starts to be dominated by edge defects introduced during the fabrication process[105]. High-resolution nucleation imaging, in both space and time, would be required to verify this, which is beyond the scope of this study.

When comparing $\mu_0 H_c$ and SFD for different $Co_{1-x}B_x$ compositions (see Fig. 6.2(c-d)), we observe a decrease in $\mu_0 H_c$ and the SFD with increasing B content. The dropping of $\mu_0 H_c$ and SFD can be partly explained by the decrease in PMA. In Table 6.1, the effective anisotropy (K) and the saturation magnetization (M_s) of $Co_{1-x}B_x$ measured through SQUID are shown. The range of the K is from the error margins established during the measurement. Detailed information on this process can be found in Appendix C.4. Both K and M_s drop with increasing B content, as expected. With smaller K, the magnetization is easier to switch, leading to a smaller $\mu_0 H_c$. However, this cannot fully explain the decrease of $\mu_0 H_c$. If the decrease in coercivity were entirely due to anisotropy, an increase in the normalized coercivity ($\frac{\mu_0 H_c}{K}$) would be anticipated with an increase in boron concentration, given the M_s decrease almost linear with boron concentration and $\frac{\mu_0 H_c}{K} = \frac{2}{M_s}$. However, as shown in Fig. C.5, the normalized coercivity declines with boron concentration, indicating that the drop in coercivity is much faster compared to the anisotropy. We propose that this abnormal drop in $\mu_0 H_c$ at the highest B content is associated with a strong increase in nucleation centers. This hypothesis is further supported by Kerr microscopy images on blanket films (see Fig. C.6). The $Co_{68}B_{32}$ sample exhibits a much larger number of nucleation centers during switching as compared to the $Co_{80}B_{20}$ sample. This indicates that a high B concentration increases the nucleation center density per unit area. Surprisingly, we observed an increased number of nucleation centers on a Co/Pt sample. The reason for this increase is still unclear; our hypothesis is that it is related to the misoriented grains of the polycrystalline Co structure, which are reported to serve as preferential sites for nucleation[173,174]. In contrast, $Co_{1-x}B_x$

Table 6.1: Material constant of $Co_{1-x}B_x$ with different composition

Materials	M_s (kA/m)	K (J/m^3)	$\frac{\sigma_K}{K}(\%)$	$d_{nu}(nm)$
Co	1187	8.0×10^5		
$Co_{80}B_{20}$	1040	$4.4 \sim 5.8 \times 10^5$	2.9∼3.5	288∼58
$Co_{68}B_{32}$	780	$2.8 \sim 3.5 \times 10^5$	3.0∼2.2	$41 \sim 16$

samples, at boron concentrations of 20% and 32%, are typically amorphous[175,176]. This is consistent with findings in CoFeB thin film systems where the crystalline-amorphous transition occurs at low boron of 6%[177]. Thus, the $Co_{1-x}B_x$ samples in our study are inferred to be amorphous and they exhibit no grain boundaries, and consequently fewer nucleation centers are observed up to a certain B content, after which it increases again. The exact mechanism of this increase requires more research, but we speculate that it is due to a more homogeneous magnetic landscape leading to a sharper nucleation field threshold further supported by the low SFD for high B content samples of islands (see Fig. 6.2d).

In the following, we will attempt to further quantify the effect of B concentration on nucleation center density. For this, we employ a model based on the Sharrock formalism Eq. 6.2 to fit $\mu_0 H_c$ and SFD of $Co_{80}B_{20}$ and $Co_{68}B_{32}$ as a function of island diameter. This fitting process allows us to extract information regarding the nucleation mechanism, such as the distance between nucleation centers d_{nu} and the homogeneity of the PMA. Note that the fitting procedure fails on the pure Co sample (see Fig. C.7). We attribute this failure to the increased number of pinning sites within the Co/Pt system[165–167,178], which hinder domain wall propagation, potentially leading to a different switching mechanism. Hence this data is left out of Table 6.1. In the following, we assume that the local anisotropy is non-uniform with a Gaussian distribution around the K as measured from SQUID measurements[161,179]. The probability of obtaining a particular K value for a nucleation center is calculated using Eq 6.1:

$$P[K] = \frac{1}{\sigma_K \sqrt{2}} exp\left(-\frac{(K - K_{mean})^2}{2\sigma_K^2}\right) \tag{6.1}$$

Here, σ_K is the standard deviation of Gaussian distribution which characterizes the intrinsic distribution in PMA. K_{mean} represents the average anisotropy and we use the absolute K value as obtained from SQUID measurements for the fitting

process(see Table 6.1). The switching field for a nucleation center ($\mu_0 H_{nu}$) can then be written as[104,161]:

$$\mu_0 H_{nu} = \frac{2K}{M_s}\left(1 - \sqrt{\frac{k_B T}{KV} ln\left(\frac{f_0 t}{ln2}\right)}\right) \tag{6.2}$$

In Eq. 6.2, M_s denotes the saturation magnetization, k_B is the Boltzmann constant, $T = 300$ K represents the temperature, $f_0 = 10$ GHz is the attempt frequency, $t = 0.1$ s is the measurement time at each applied field, and V corresponds to the nucleation volume, which is defined as $V = \frac{\pi z l_{nu}^2}{4}$. $z = 0.8$ nm is the thickness of the FM layer. Here, l_{nu} represents the diameter of a nucleation site, defined as twice the domain wall width (2δ). The domain wall width is derived from $\delta = \pi\sqrt{\frac{A}{K_{eff}}}$, where A denotes the exchange stiffness. A range of A values has been reported for different samples and thicknesses, complicating the estimation of A for ultrathin magnetic layers[42,180]. Here, we do not measure the A but instead assume $A \approx 10$ pJ/m for Co thin film from similar systems[181]. For $Co_{80}B_{20}$ and $Co_{68}B_{32}$, we adopt reduced values of $A \approx 5$ pJ/m and $A \approx 4$ pJ/m, respectively, reflecting the tendency of A to decrease with increased alloying element concentration[182]. These assumptions are made based on the observations that significant changes in the A occur when transitioning from a crystalline to an amorphous state; however, in the amorphous state, increases in boron have only a minor effect on A[177]. The total number of nucleation centers (N) for a patterned island is defined as $N = \frac{A_{area}}{d_{nu}^2}$, where d_{nu} is the distance between nucleation centers. The larger d_{nu}, the fewer nucleation centers per unit area. Knowing $P[K]$, the distribution of the switching field of the nucleation center ($P[\mu_0 H_{nu}]$) can be obtained through Eq. 6.2. Given the complex relationship between $\mu_0 H_{nu}$ and K, obtaining an analytical expression for $P[\mu_0 H_{nu}]$ is challenging. Here we adopt a numerical approach to approximate this distribution. Initially, we generate a large number of random K values from the Gaussian distribution in Eq. 6.1. Subsequently, we compute the corresponding $\mu_0 H_{nu}$ values utilizing Eq. 6.2 and estimate the $P[\mu_0 H_{nu}]$.

For an island to switch at a certain field (x mT), two conditions must be satisfied: (1) at least one nucleation site switches at this field and (2) no nucleation sites switch below this field. The distribution of the switching field of an island $P[\mu_0 H_{is}]$

can then be derived:

$$P[\mu_0 H_{is} = x] = N \cdot P[\mu_0 H_{nu} = x] \cdot (1 - P[\mu_0 H_{nu} < x])^{N-1} \tag{6.3}$$

This distribution $P[\mu_0 H_{is}]$ is then used to calculate the simulated $\mu_0 H_c$ (the mean of $\mu_0 H_{is}$) and the SFD (the standard deviation of $\mu_0 H_{is}$), which are then compared with the measured values in Fig. 6.2c and d. From the fitting, the values of σ and d_{nu} of $Co_{1-x}B_x$ are obtained.

The obtained values of σ_K normalized by K ($\frac{\sigma_K}{K}$) and d_{nu} are shown in table 6.1. It's important to note that the error in K has been accounted for, and the corresponding normalized $\frac{\sigma_K}{K}$ and d_{nu} were simulated across the range of K values (details in Appendix C.9). For $Co_{80}B_{20}$, the normalized σ_K values range between 2.9% and 3.5%, whereas for $Co_{68}B_{32}$, they range from 2.2% to 3.0% relative to their respective K values. These ranges align with those reported in existing literature[161,183]. The d_{nu} of $Co_{68}B_{32}$ sample is overall higher compared to $Co_{80}B_{20}$ sample, indicating a higher nucleation density in $Co_{68}B_{32}$ compared to $Co_{80}B_{20}$. This observation confirms that the introduction of a higher concentration of B in the system can lead to an increased number of nucleation sites.

6.4 Summary

In conclusion, our study demonstrates that by introducing B in Co-based SAF NPs, $\mu_0 H_c$ and SFD can be reduced significantly. This reduction can be attributed to two main factors: the decrease in PMA and increased nucleation center density in the material. The decrease in PMA resulting from the introduction of B will, however, reduce the torque transfer of PMA-SAF NPs due to its reduced K. Furthermore, our findings reveal that the rate of decrease in $\mu_0 H_c$ is higher than the decrease in anisotropy. This observation confirms that introducing B serves as an effective way to tune the coercivity of patterned PMA-SAF nanostructures. Our study shows the potential of B as a parameter for optimizing the operational magnetic properties of PMA-SAF NPs, offering opportunities for their utilization in various applications.

7

Dynamics of Synthetic Antiferromagnetic Nanoplatelet Chains in a Rotating Magnetic Field

This study presents an in-depth analysis of the behavior of synthetic antiferromagnetic nanoplatelet (SAF NP) chains in the presence of rotating magnetic fields. Our findings show that SAF NP chains exhibit notable rigidity due to their high anisotropy and disc shape. They can maintain a rod-like structure without undergoing S-shaped deformations typically seen in superparamagnetic bead chains. Experimentally, we demonstrate that SAF NP chains can sustain synchronized rotation with external fields up to 15 Hz, and modeling suggests this synchronization could extend to even higher frequencies. Significantly, at 10 Hz, the chain length of SAF NPs surpasses 100 μm, markedly longer than that of superparamagnetic bead chains. The rigid property of the chains positions them as promising candidates for advanced applications in microfluidics.[*]

7.1 Introduction

Magnetic nanoparticles (MNPs) and their assemblies have gained considerable interest for their potential in remotely manipulating lab-on-chip devices[184]. In these systems, which are characterized by small dimensions and low Reynolds numbers, liquid transport is predominantly diffusion-limited[185]. Numerous stud-

[*]This manuscript is in preparation: **Li, J.** *et. al.*

ies have demonstrated that MNPs can effectively enhance the transport of liquids and targeted molecules, thereby facilitating processes such as mixing, transport, and sorting in microfluidic devices[186]. A particularly notable application, which is the focus of this work, involves using rotating chains of MNPs, such as superparamagnetic bead chains, to improve mixing in these devices[187]. Under external magnetic fields, these MNPs self-assemble into chains, creating a unidirectional magnetic moment[188,189]. Upon application of a rotating magnetic field, the chains undergo rotational motion, resembling the action of a magnetic stirring bar, exerting mechanical forces on the surrounding liquid[157].

Understanding the mechanical response of these MNP chains, particularly in terms of chain length, deformation, and phase lag of the chain relative to the external field in response to a rotating magnetic field, is crucial for evaluating their effectiveness and suitability for applications such as mixing. Research through both computational and experimental studies has investigated the dynamics of spherical superparamagnetic bead chains, such as FeO_x-based MNPs which we call SPION, in rotating magnetic fields. Melle *et al.* have shown that these chains can rotate synchronously with the magnetic field frequency with a delayed phase angle[190]. However, at sufficiently high field frequencies, a reverse motion of the chains occurs due to viscous drag, decelerating their rotation speed and leading to asynchronous rotation with the field[191]. The chains exhibit shorter lengths at higher rotation frequencies, following a negative exponential power law relationship relative to the frequency[190,192,193]. Phenomena such as the formation of S-shaped chains and non-chain clusters of particles have also been observed under different rotational conditions[194]. These chain dynamics are governed by the Mason number (M_n), defined as the ratio of viscous to magnetic forces[91,92,194]. At high Mason numbers, due to increased viscous forces, chains tend to cluster and break into shorter lengths. The chain length inversely scales with the square root of the Mason number[92]. Below a specific critical Mason number, S-shaped chains remain stable; above this threshold, the chains are prone to breakage near the center[91].

As mentioned above, chains of spherical superparamagnetic MNPs, which display relatively low magnetic anisotropy, are susceptible to asynchronous rotation, deformation, and breakage, especially at high frequencies or in high-viscosity fluids

(meaning high M_n). Although it is reported that the breakup and reformation of the chain under certain conditions can induce chaotic mixing, facilitating the mixing[157], the tendency of shorter chain length and asynchronous rotation reduced overall the mixing efficiency[195]. New types of MNPs with high anisotropy, either with intrinsic or shape anisotropy, are of interest for these rotating applications to form longer chains and provide synchronous rotation. However, there are few studies on the influence of highly magnetic anisotropic MNPs and MNPs of varying shapes on chain dynamics.

In this work, we introduce disc-shaped nanoparticles - synthetic antiferromagnetic (SAF) nanoplatelets (NPs) - with perpendicular anisotropy (PMA), consisting of a multilayer stack: Ta/Pt/CoFeB/Pt/Ru/Pt/CoFeB/Pt[62,64,127]. The significant hybridization of the 3d-5d orbitals at the Co and Pt interfaces induces a strong PMA[74,75]. These SAF NPs, featuring two ferromagnetic layers antiferromagnetically coupled through the Ru layer via the Ruderman-Kittel-Kasuya-Yoshida (RKKY) interaction[77–79], exhibit zero net magnetic moment under zero field. Under a magnetic field, SAF NPs form chains in two configurations[85]: a side-by-side configuration under a low external field, connecting the nanoplatelets at their edges, and a face-to-face configuration under a high magnetic field, where the surfaces of the NPs attach to each other. Notably, in the face-to-face configuration where the NPs are magnetically saturated, the large contact area between NPs and the high magnetic anisotropy are excepted to contribute to the formation of stable chains compared to spherical particles.

However, research on the dynamics of SAF NP chains remains unexplored. In this study, we investigate the dynamics of SAF NPs under a rotating magnetic field through optical microscopy. Our research initially focuses on examining chain deformation across various rotating frequencies and in different viscosity solutions. Furthermore, we analyze the synchronized motion region of the chains in relation to the external field and investigate the correlation between chain length and rotating frequency.

7.2 Methods

The SAF NPs employed in this study are comprised of multilayer thin films $[Ta(2)/Ru(2)]_3[Ta(4)/Pt(2)/CoFeB(0.8)/Pt(0.4)/Ru(0.8)/Pt(0.4)/CoFeB(0.8)/Pt(2)]_5Ta(4)$, with layer thickness in nanometer, as depicted in the insert of Fig. 7.1a. These NPs were fabricated through substrate conformal imprint lithography, as detailed in the work[127]. The diameter of the NPs is 1.88 µm with a thickness of 72 nm, as shown in the SEM image in Fig. 7.1a.

For the dispersion of SAF NPs, we used liquids with varying viscosity levels, maintaining a consistent NP concentration across all measurements. The liquids comprised of mixtures of glycerin and deionized (DI) water in various ratios (50% and 75% glycerin). Chain formation took place in circular cells with a diameter of 5 mm, constructed from two glass coverslips separated by a 1 mm-thick PDMS spacer. Before the experiments, these cells were left overnight to enable the sedimentation of the NPs at the bottom of the cell.

The experimental setup for observing chain rotation is illustrated in Fig. 7.1c. A rotating magnetic field was generated by a Hallbach array, attached to a motor. The central magnetic field strength was measured to be 418 mT (see Fig. D.1 for the field distribution inside the Hallbach array), and the profile of the Hallbach array is shown in Fig. 7.1d. The prepared cells were placed at the center of the Hallbach array for observation under a microscope.

To initiate chain formation, the cells were first exposed to the stationary Hallbach array for 30 minutes to form chains. Following chain formation, the Hallbach array was rotated at variable speeds. The rotation of the chains was recorded using a Hamamatsu digital camera at approximately 30 frames per second. For image analysis, ImageJ was used to remove background noise, and Matlab was utilized for binarizing the images and quantifying the chain lengths in each frame.

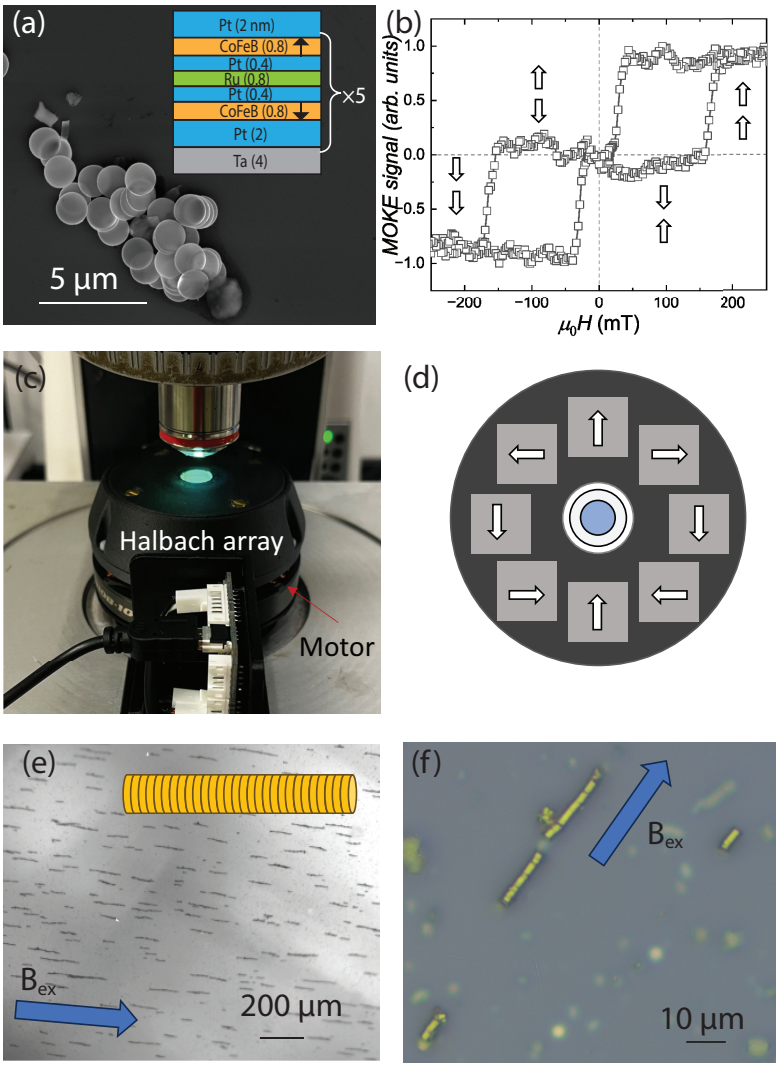

Figure 7.1: (a) Scanning Electron Microscopy (SEM) image of the released SAF NPs. Inset: The multilayer stack composition utilized in this study. (b) Hysteresis loop of SAF NPs, measured via Magneto-Optical Kerr Effect (MOKE), while still adhered to a wafer and not released. (c) Schematic of the experimental setup for measuring magnetic chains. The rotating magnetic field is provided by the Halbach array which is mounted on a motor to rotate. (d) Detailed view of Halbach array and the measurement cell. The Halbach array is composed of $1 \times 1 \times 1$ cm^3 NbFeB cubes, with white arrows indicating the direction of magnetization. SAF NPs are dispersed within a cell of 5 mm in diameter. (e) SAF NPs in a 50% glycerin mixture, positioned within the non-rotating Halbach array for 15 minutes. The NPs form face-to-face connected chains. The blue arrow indicates the external field direction. (f) Optical microscopy image of SAF NPs drop-cast on a silicon wafer and dried under an applied in-plane external magnetic field.

7.3 Results

7.3.1 Chain Formation Under a Constant Magnetic Field

The Magneto-Optical Kerr Effect (MOKE) measurement of SAF NPs after fabrication and prior to release in solution is shown in Fig 7.1b, with arrows indicating the direction of magnetization. At low magnetic fields, the NPs display antiparallel magnetization, leading to a net zero magnetization. Conversely, at high magnetic fields, the NPs reach saturation and their magnetization aligns out-of-plane. Within the Halbach array, the magnetic field strength surpasses the saturation threshold, resulting in the NPs being saturated with an out-of-plane magnetization.

We begin by examining chain formation in a constant magnetic field. Figure 7.1e displays a microscopic image of NPs suspended in a 50 % glycerin mixture under a stationary Hallbach array for 15 minutes. Here, the NPs adhere to one another, creating chains that align with the external magnetic field direction. Owing to the saturation of the NPs, they predominantly connect in a face-to-face configuration, consistent with the observations reported by T. Vemulkar *et al*[85]. Notably, it is reported that under weak magnetic fields, the NPs arrange themselves side-by-side. Like spherical particles, this configuration is not rotationally stable and is not the focus of our current study. Additional support for the face-to-face configuration is provided by the optical microscopy image (Fig. 7.1f), captured after drop-casting of the NP solution onto a silicon wafer and subsequent drying within the Halbach array. This image distinctly shows the NPs aligned in a face-to-face configuration.

7.3.2 Chain Dynamics in a Rotating Magnetic Field

This section delves into the dynamics of NP chains when exposed to rotating magnetic fields. Three key aspects are critically important for their practical applications: (1) the tendency of the chains to deform under different magnetic fields, (2) the synchronization of chain rotation with the external field, and (3) the variation in chain length. We will explore each of these aspects comprehensively.

Deformation

To evaluate the deformation of the NP chains, rotating magnetic fields at various frequencies were applied to pre-formed chains in a liquid mixture with different glycerin concentrations. The deformation of the chains was observed to be similar in mixtures containing 50% and 75% glycerin. For detailed analysis, we take the NP chains in 75% glycerin for illustration. Microscopic images captured at set time intervals, as presented in Fig. 7.2, demonstrate the chains' responses at frequencies of 0.1 Hz, 1 Hz, and 5 Hz.[†] The first column of Fig. 7.2 depicts the initial state of the pre-formed chains, while the subsequent columns display their states at various time points within the same rotation cycle.

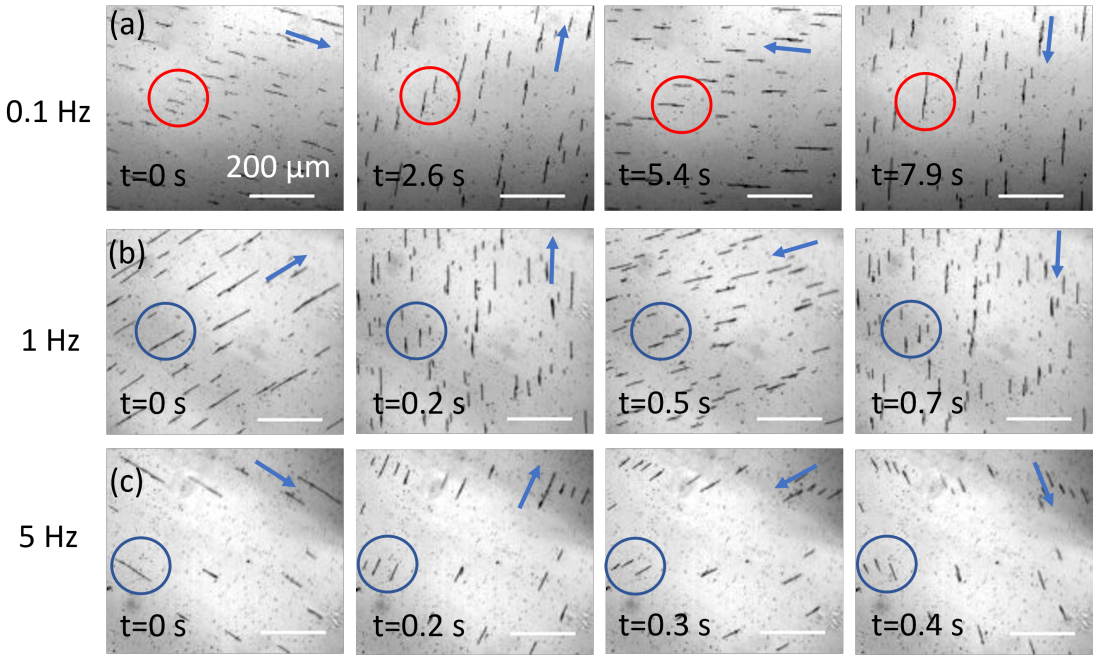

Figure 7.2: Microscopy images illustrating the behavior of SAF NP chains in a 75% glycerin mixture under various rotating magnetic field frequencies: (a) 0.1 Hz, (b) 1 Hz, and (c) 5 Hz. The first column of images depicts the chains prior to rotation, while the subsequent images capture the chains during the application of the rotating magnetic field. Blue arrows indicate the direction of the magnetic field.

At a low rotational frequency of 0.1 Hz, end-to-end aggregation of shorter chains was observed, leading to the formation of elongated structures. As highlighted

[†]Scan the QR code in Appendix D.2 for videos of chains under different rotating frequencies

by the red circles in Fig. 7.2a, three separate chains combine to form a single, longer chain, a process we term 'combination'. Additionally, we noticed that when chains come into proximity during rotation, they may undergo lateral attachment, thereby forming a 'wider' chain. This event is depicted within the circled region in Fig. 7.2a, where the darker part of the chain shows the attachment of two chains. At higher frequencies, such as 1 Hz and 5 Hz, these phenomena of combination and lateral attachment were rarely observed. Instead, 'break-up' events were observed, where the long chains break into small fragments as shown in the blue circles in Fig. 7.2b-c.

The occurrence of combination and lateral attachment is primarily governed by the dipolar interactions between the chains, which supersede the influence of viscous forces, thereby facilitating chain amalgamation rather than fragmentation. Moreover, the rotational motion of chains increases the chance of chains finding each other and further increases the connection. This increase is also reported in SPION chains[192]. Further increasing the rotating frequency, the viscous forces become dominant, surpassing the dipolar interactions and leading to the break of the chain.

However, irrespective of the interaction mode — combination, lateral attachment, or break-up — the chains consistently maintained a linear morphology as shown in Fig. 7.2a-c. No S-shaped deformations, commonly reported in SPION chains[91,194], were detected in the studied frequency range (0.1 to 10 Hz). Even under a higher frequency of 15 Hz (see Fig. D.4), the chains still keep the linear configuration, suggesting that the NP chains are rigid and resistant to bending. This rigidity can be attributed to the disk-like morphology of the NPs, which increases the friction between particles avoiding displacement. Additionally, the high uniaxial PMA of NPs induces a priority for alignment perpendicular to the applied magnetic field, further avoiding bending via fluid guiding.

Synchronized Rotation

The synchronization of chain motion with an external rotating field is a crucial factor affecting application efficiency. We measured chain movements in each frame during rotation and correlated these with the frequency of the external

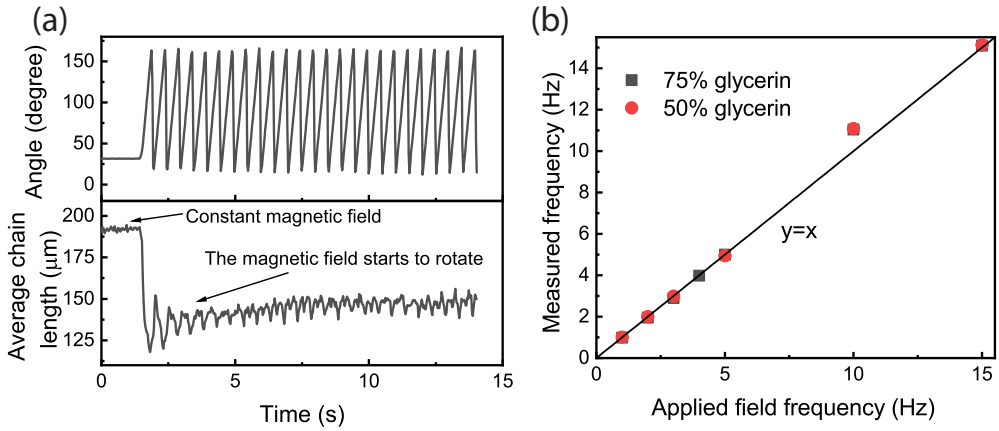

Figure 7.3: (a) Variation in the average orientation angle and average length of NP chains over time in a 75% glycerin mixture. At around 1.4 seconds, the magnetic field started to rotate at 1 Hz. (b) Correlation between the measured rotation frequency of the chains and the rotating frequency of the external magnetic field.

field, as depicted in Fig. 7.3. Figure 7.3a shows the average angular orientation and length of chains in a 75% glycerin mixture over time. These averages were derived from all chains in individual microscopy images, with the method for determining chain angle and length detailed in Appendix D.3. Due to the rod shape of the chain, the recognized angle only ranges between 0 and 180 degrees. At approximately 1.4 seconds, the external field started to rotate at 1 Hz, the chains rotated correspondingly. We also noted that upon rotation initiation, the chain length decreases which indicates the chain breaks into shorter segments, aligning with the high-frequency break-up events discussed above. After a few seconds of rotation, the chain length stabilized, suggesting equilibrium had been reached.

The average angular orientation of the chains allowed us to deduce the chain rotation frequency through the Fourier transform. Figure 7.3b illustrates the chain rotation frequency as a function of the external field's rotation frequency under varying viscosity conditions. Remarkably, up to 15 Hz, chains in both 50% and 75% glycerin mixture exhibited identical rotation frequencies to the external field, demonstrating effective synchronization. Experimental limitations prevented exploration beyond 15 Hz. However, compared to other micro-sized chains in literature[191], which lose synchrony with the external field at 15 Hz in solution with

lower viscosity, SAF NP chains exhibit considerable rigidity.

To further evaluate the boundaries of synchronized motion, we developed a model incorporating magnetic torque and viscous torque to estimate the phase lag (α) which is the angle between the external field and the rotation of the chain. A constant α in the model represents the synchronized rotation of the chain and the applied field.

The model's schematic, shown in Fig. 7.4a, considers chains rotating in the X-Y plane. We assume the chain contains $2N$ NPs and the middle of the chain is at the origin point of the Cartesian coordinate system. Magnetic torque (τ_{mag}) from the rotating magnetic field and viscous torque (τ_{vis}) arising from the rotational friction with the surrounding fluid act upon the chain. The external field's angle is given as ωt, where ω is the angular velocity of the field. To simplify the model, we made several assumptions: (1). The NPs are identical in shape and magnetic properties and their magnetization is always aligned perpendicular to the NP surface. (2). The chain is regarded as a rigid rod, which is unaffected by breakage or combination. (3). The interaction between chains and between the chain and substrate is not taken into account. (4). The thermal fluctuation and Brownian motion of the chain are neglected[91,190].

The chain's rotation angle at time t, $\theta(t)$, is defined as the angle between the rod's long axis and the initial angle ($\theta(0) = 0$). The phase lag α is:

$$\alpha(t) = \omega t - \theta(t) = 2\pi f_B t - \theta(t) \tag{7.1}$$

where f_B is the external field's rotation frequency.

The τ_{mag} of the chain is calculated as:

$$\tau_{mag} = 2mNBsin(\alpha) \tag{7.2}$$

with m being the magnetization of a single SAF NP, and B the the external field. m is derived from M_sV, with $M_s = 1300\ kA/m$ used in the simulation, and V is the volume of the magnetic materials in a single NP.

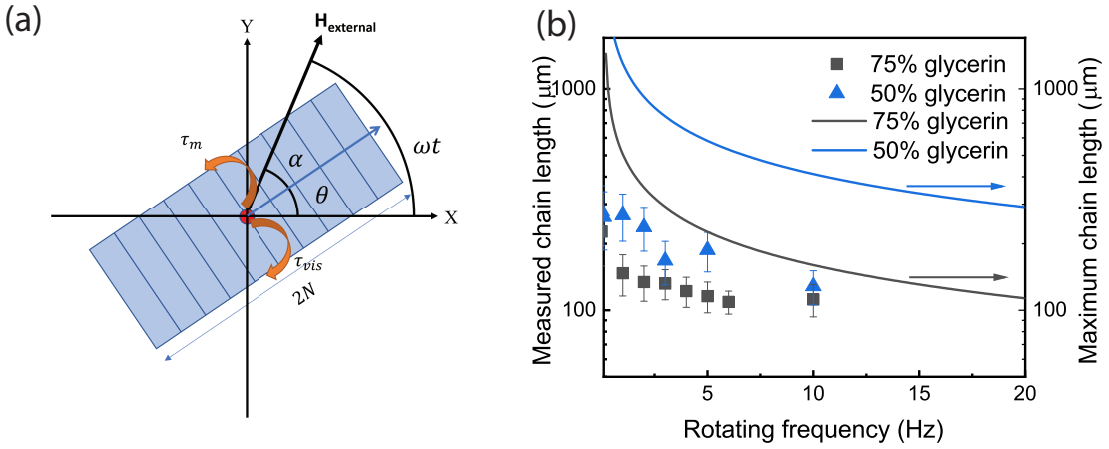

Figure 7.4: (a) Schematic representation of a magnetic chain consisting of 2N particles with a thickness of 72 nm. The chain is subjected to a rotating magnetic field with a constant angular frequency ω. The chain is aligned at θ degree. The angle between the rotated field and the chain's angle is the phase lag which is denoted by α. (b) The solid lines show the simulated maximum chain length to maintain the synchronized rotation under a certain rotation frequency. Chain lengths below this threshold can achieve synchronized rotation, whereas lengths above it cannot. The points indicate the experimentally measured stable average lengths of SAF NP chains relative to the rotating frequency.

For an individual NP, the viscous torque is calculated from

$$\tau_{vis} = -\zeta(\frac{d\theta}{dt}) = -\zeta(2\pi f_B - \frac{d\alpha}{dt}) \tag{7.3}$$

where $\zeta = 3\pi S\eta dr^2$ is the rotational friction factor of one NP. S is the shape factor. For a disc-shaped particle with a diameter of 1.88 µm and thickness of 72 nm, S is set to 0.313[196]. The viscosity of the solution (η) varies with the glycerin concentration; for a 50% glycerin mixture, η is 8.37 $mPas$, and for a 75% mixture, it is 55.27 $mPas$. The equivalent diameter (d) of NPs, regarded as the diameter of a spherical particle with the same volume as the NP, is 0.36 μm. The variable r is the distance of an NP from the origin (0,0). Here the minus sign in the Eq. 7.3 defines that the viscous torque is in the opposite direction of the magnetic torque. As each NP contributes to the chain's viscous torque, the total torque is the sum

of torques on $2N$ NPs, calculated as:

$$\tau_{vis} = -3\pi S\eta d(2\pi f_B - \frac{d\alpha}{dt}) \sum_{i=-N}^{N} (it)^2 \tag{7.4}$$

The rotational dynamics of the chain under a rotating magnetic field is governed by:

$$I\frac{d^2\alpha}{dt^2} = \tau_{mag} + \tau_{drag} \tag{7.5}$$

Here I is the chain's inertia, which is typically negligible due to its low value[91,190]. When the chain reaches equilibrium, the total torque is equal to zero. Solving the Eq. 7.5 under equivalent, with initial conditions $\theta(0) = 0$ and $\alpha(0) = 0$, we can calculate $\alpha(t)$ for chains comprising different numbers of particles.

At an angle α of 45°, the magnetic torque reaches its maximum, further increasing the phase lag leads to a decrease in the torque which potentially disrupts the balance with viscous torque[23]. Therefore, we define $\alpha = 45°$ as the threshold for maintaining synchronized rotation. Under this specific condition, we determined the maximum chain length that can maintain synchronized motion in 50% and 75% glycerin mixtures at different external field rotating frequencies, which is depicted by the solid lines in Fig. 7.4b. Below the solid line, chains can maintain synchronized motion; above it, they cannot rotate synchronously with the field. We observe that as viscosity increases, the maximum chain length for synchronization decreases, a consequence of the increasing viscous torque. According to our estimations, the chains are expected to achieve synchronized motion with the external field even at rotational frequencies exceeding 15 Hz. However, as frequency increases, the maximum chain length to maintain synchronous motion decreases.

Chain length

As previously discussed, the rotational frequency of the external field influences the maximum chain length that can maintain synchronized motion. To confirm whether the measured chains fall within this synchronized motion region, we compared the chain length at varying rotational field frequencies and fluid viscosities

with our model.

The chain length was determined by the average length upon achieving system equilibrium as shown in Fig. 7.3a. The stable average chain length, as a function of rotational frequencies under different viscosities (75% and 50% glycerin mixture), is plotted in Fig. 7.4b. The error bars represent the standard deviation of chain length in the frame when stable. Notably, all chain lengths lie within the synchronized motion region, confirming their synchronized movement, as observed in Fig. 7.3b. However, a noticeable discrepancy exists between the simulated maximum chain length to keep the synchronized rotation and the measured lengths. This discrepancy is expected, as the model is simplified. On one hand, we assume the magnetization is always perpendicular to the NP surface, which is not the case in reality, leading to an overestimation of the maximum chain length. On the other hand, we assume the chain is rigid, whereas actual chains may experience breakage. The NPs are not perfect; unflat surfaces or contaminants, e.g. dust or dirt from fabrication, in the mixture can cause chains to break, resulting in shorter lengths. Additionally, interactions between chains and with the substrate, which the model does not account for, can further reduce the chain length.

Now, let us discuss the trend of measured chain lengths with respect to rotation frequency. From Fig. 7.4b, we observed that higher rotational frequencies and higher viscosity correspond to reduced chain lengths, a trend consistent with observations in SPION chains[192]. This reduction in length is attributed to increased viscous forces at higher rotation speeds, leading to chain fragmentation. Contrary to our initial hypothesis, we did not observe an obvious increase in average chain length at lower frequencies, despite the occurrence of combination events. This could be due to fluctuations in individual chain lengths, which vary considerably among chains. Remarkably, at a frequency of 10 Hz, the average chain length reaches 128 µm and 112 µm for 50% and 75% glycerin mixtures, respectively. These lengths are significantly longer than those typically observed in SPION chains, which are normally below 15 µm[191,192] at 10 Hz.

7.4 Conclusion

SAF NP chains exhibit significantly greater rigidity compared to SPION chains, as evidenced by their ability to maintain a rod-like structure without exhibiting S-shaped deformations, even during chain breakup. Remarkably, SAF NP chains demonstrate enhanced stability at high rotation frequencies and in high-viscosity environments e.g. 75% glycerin mixture. This is reflected in their synchronized motion and maintaining large chain lengths under high viscous drag. These properties highlight the substantial potential of SAF NP chains for use in microfluidics, targeted drug delivery, and magnetic manipulation, underscoring their relevance for future technological and scientific applications.

8

Conclusions and outlook

Addressing the challenges outlined in the introduction, we focused on three key areas: the fabrication, magnetic properties, characterization, and mechanical response of perpendicularly magnetized synthetic antiferromagnetic nanoparticles (p-SAF NPs). This section is dedicated to summarizing our key findings in these domains and offering recommendations for future research directions.

8.1 Conclusion

In this thesis, we have successfully demonstrated that Substrate Conformal Imprint Lithography (SCIL) can be used to fabricate p-SAF NPs with uniform diameters in both the micrometer (1.8 µm) and sub-micrometer (120 nm) range in Chapter 4. After fabrication, these NPs retain their high PMA, crucial for high-torque applications, marking a significant step forward in the large-scale production of magnetic nanoplatelets via a subtractive method. In Chapter 6, we explored the magnetic properties, specifically coercivity and switching field distributions, of p-SAF NPs. Our findings revealed that the introduction of boron (B) into Co-based SAF NPs significantly reduces both the coercivity ($\mu_0 H_c$) and the switching field distribution (SFD). This reduction can be attributed primarily to a decrease in PMA and an increase in nucleation center density within the material due to added boron. By introducing boron, we are able to control the coercivity to a low range, allowing the NPs to be switched on by a low external field.

In Chapter 5, we showed that PT MCD is an effective technique for investigating the magnetization switching of single p-SAF NPs. Specifically, PT MCD allowed us to measure the spatial and temporal heterogeneity in the magnetic properties of p-SAF NPs with a diameter of 120 nm, particularly in terms of their switching fields at the single-particle level.

In Chapter 7, we explored the assembly and mechanical rotation of 2 µm diameter p-SAF NPs under varying frequencies of rotating magnetic fields and different viscosities. It observed that these NPs form chains that are more rigid than the commonly used SPION chains. Notably, they synchronize their rotation with the external field at higher frequencies and maintain longer chain lengths.

8.2 Fabrication

Although we have successfully fabricated the p-SAF NPs and have tuned the coercivity within a manageable range, challenges remain in terms of practical application. A primary concern is the functionalization of these p-SAF NPs. The presence of cobalt (Co) in the thin-film stack, a material toxic to biological systems, presents a significant hurdle[197]. While the thin-film structure of these NPs may limit direct exposure, the exposed side walls of Co still pose a risk of environmental contact and need to be avoided. Additionally, the rapid sedimentation of p-SAF NPs in solutions indicates a lack of stable colloidal formation, an essential feature for many applications. Furthermore, for targeted biomolecule applications, these NPs require attachment to specific ligands, necessitating stabilization and functionalization.

The functionalization of p-SAF NPs, a topic not covered in this thesis, is a critical area for future research. One potential approach involves depositing a layer of gold (Au) to encapsulate the NPs, utilizing thiol-containing ligands that can form covalent bonds with the Au surface for attachment[198]. The selection of specific ligands for functionalization will depend on the intended application and is beyond this thesis's scope. However, options such as polyethylene glycol 2-mercaptoethyl ether acetic acid could be considered for both steric and electrostatic stabilization[199]. Addressing these functionalization and stabilization challenges will be crucial in advancing the practical application of p-SAF NPs in various fields.

8.3 Novel types of nanoplatelets

Utilizing SCIL technology, we can fabricate disc-shaped particles, and with sputtering, the thin film layers can be easily tuned. These techniques allow us to create not only p-SAF NPs but also various other types of nanoparticles with distinct magnetic properties. Here, we discuss some potentially interesting nanoparticle types with unique magnetic properties for future exploration.

8.3.1 Asymmetric stack

For certain applications, such as self-assembly, it is essential to achieve precise alignment of particles, such as orienting a particular face of the particles in a specific direction. This precise orientation ensures that the building blocks can connect in a desired manner. One strategy to achieve this involves engineering the basic SAF stacks so that one of the magnetic layers can consistently switch before the other. We refer these stack with different switching sequences as an 'asymmetric stack.' This can be achieved in several ways described below.

Exchange bias

The exchange bias effect arises from the exchange interaction at the interface between ferromagnetic (FM) and antiferromagnetic (AF) layers[200]. This interaction stabilizes the spins of the ferromagnet in a certain direction which is influenced by the uncompensated surface of AF materials. An uncompensated surface refers to an imbalance in antiparallel spin alignment, resulting in a net magnetization. This phenomenon can lead to a shift in the hysteresis loop.

In SAF NPs, the exchange bias effect is used to fix the orientation of the magnetization of one layer, creating asymmetry and directional alignment of the NPs. This is achieved by adding an AF layer, such as IrMn, on top of a FM layer, like Co. Here we present preliminary results on the SAF NPs with exchange bias. Adding IrMn on top Co leads to an exchange bias coupling that is evident in the shifted hysteresis loop shown in Fig. 8.1, where the right half of the loop is notably displaced to the right.

Since NPs have the freedom to rotate in a fluid medium, they will naturally

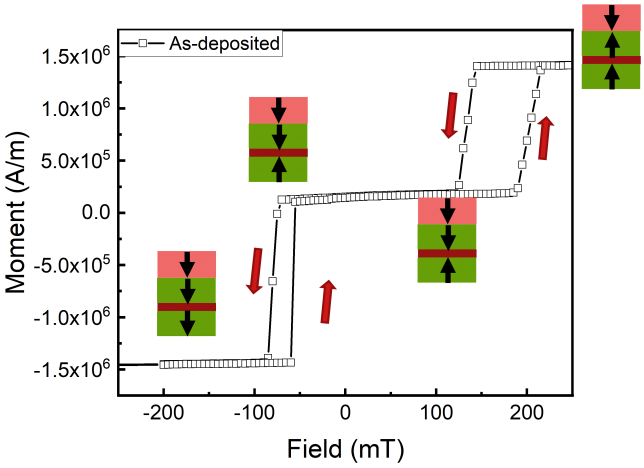

Figure 8.1: Hysteresis loop of p-SAF NPs with exchange bias measured by SQUID

orient themselves in the direction such that the AF layer's uncompensated spins is parallel to the external field, as this is the energetically favorable state. Figure. 8.2a displays the simulated energy profiles for NPs aligned at angles of 0°, where the AF layer's spins align parallel to the external field; at 90°, where the spins are perpendicular to the external field; and at 180°, where the spins are antiparallel to the external field. The corresponding spin alignments for these orientations are shown in Fig. 8.2b. The energy required for alignment at 0° is consistently lower or equal compared to that at 180°, indicating a natural tendency for the NPs to align at 0°, the direction of the AF layer's uncompensated spins. At lower fields, the lowest energy alignment occurs at 90°, suggesting that NPs will align perpendicular to the external field, which is the same as the behavior of standard p-SAF NPs (as detailed in the literature in Section 2.4).

Synthetic ferrimagnetic NPs

Synthetic ferrimagnetic NPs arise when the top and bottom FM layers in SAF structures have different thicknesses. This asymmetry can result in a preferred alignment direction, as indicated by prior studies[85]. Although this method is simpler for introducing asymmetry, it is important to note that it induces net magnetization, potentially leading to aggregation issues. An alternative method involves designing a structure with equal total magnetic moments but different anisotropy levels, potentially also leading to preferred alignment.

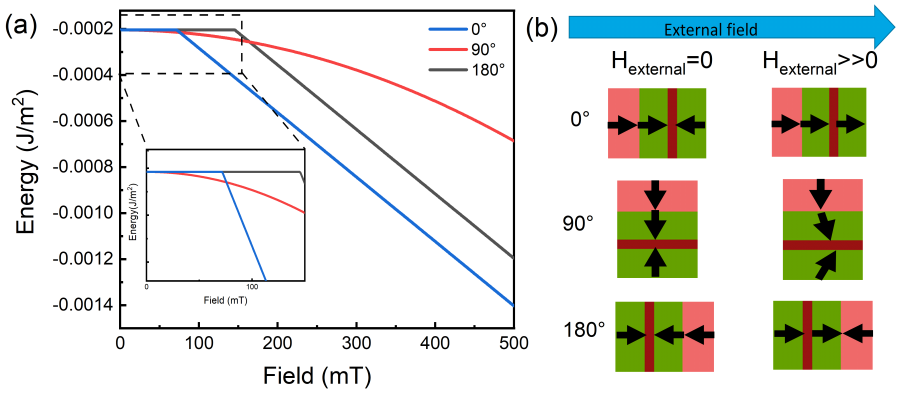

Figure 8.2: Energy profile of p-SAF NPs with exchange bias in response to increasing field strengths. Energy calculations were conducted for three distinct orientations of the NPs relative to the external field: 0°, 90°, and 180°. The illustration in (b) depicts the alignment of the NP in relation to the external field, with black arrows indicating the direction of the spins.

It is feasible to use a thin film stack composed of Co and Gadolinium (Gd) to achieve the asymmetric structure. Co/Gd stack is synthetic ferrimagnetic as well. Furthermore, this thin film structure can be optically switched using a laser, providing an alternative method for manipulating NPs[201].

8.3.2 In-plane SAF

Although we mentioned in Chapter 1 that in-plane SAF NPs are not suitable for torque-related applications, they hold potential for other uses. A key advantage of in-plane SAF is that their susceptibility can be easily tuned by changing the interlayer magntic anisotropy though thickness modification[57,59,202]. Additionally, in-plane SAF structures can achieve high susceptibility up to 1600[202], a value higher than SPIONs. These characteristics make them particularly suitable for applications in immunoassays to quantify the number of analysis biomolecules. These assays frequently utilize the magnetic response of magnetic particles in AC fields, where high susceptibility typically amplifies the magnetic response, thereby enhancing sensitivity[203,204].

8.4 Characterization

While PT MCD is a powerful tool for studying magnetic properties, it does not directly measure the mechanical torque of p-SAF NPs. As mentioned previously, magnetic torque is not directly equivalent to mechanical torque, alternative methods for measuring mechanical torque are necessary.

Atomic Force Microscopy (AFM), a technique sensitive to small torques and forces even in the piconewton range, presents a potential solution[205]. The conceptual setup for using AFM to measure mechanical torque is shown in Fig. 8.3a. It involves placing a NP on a cantilever and applying an external field. The exerted torque causes the cantilever to deflect, and this deflection (Δz) is detected by a laser reflecting the change in the cantilever's position. By correlating the cantilever's deflection, its mechanical properties, such as the spring constant (k), and the NP's position (r), we can calculate the force through $F = k\Delta z$ and the torque through $T = F \times r \cos\alpha$[206].

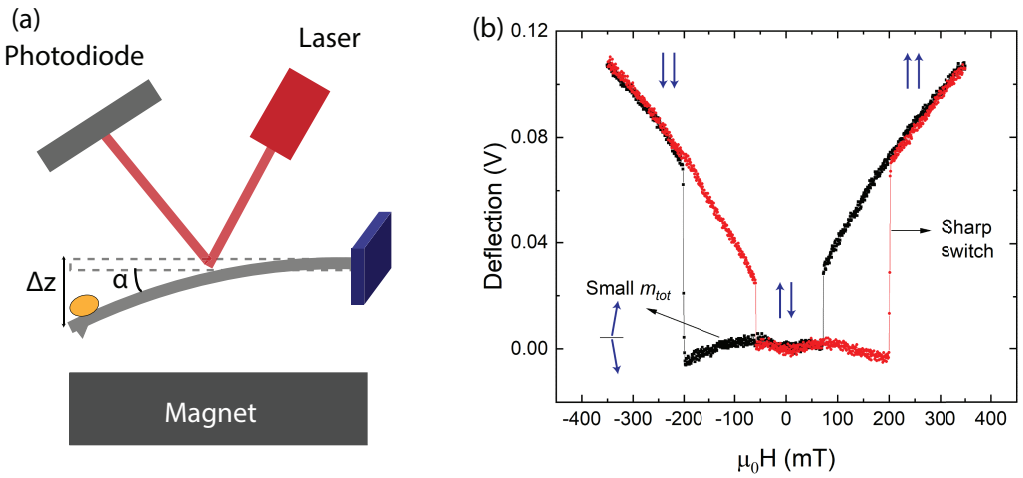

Figure 8.3: (a) Schematic of the AFM setup for measuring torque. A NP is attached to a cantilever, which is positioned above a magnet that generates the field. This magnetic field causes the NP to experience a mechanical torque, leading to the bending of the cantilever. A laser is reflected onto the cantilever to detect its bending. (b) Deflection of the cantilever as a function of the applied magnetic field. The thin film stack Ta(4)/Pt(2)/CoB(0.8)/Pt(0.4)/Ru(0.8)/Pt(0.4)/CoB(0.8)/Pt(2) is deposited on the cantilever. The black curve corresponds to the sweep of the magnetic field from positive saturation to negative saturation, and the red curve corresponds to the back sweep. The blue arrows represent the magnetization of the FM layers.

We utilized a SAF thin film stack on a cantilever to demonstrate this principle, with the deflection shown in Fig. 8.3b. Huge change of deflection, corresponding to magnetization state changes from AF to FM or vice versa, indicated the potential to measure the switching of the SAF stack. The observed linear relationship between deflection and the external field after saturation, which we successfully measured, is expected. From this linear relationship, we can estimate mechanical torques on the order of 10^{-13} Nm, validating the method's sensitivity and accuracy. The details of this measurement process are further elaborated in Ruijs's thesis[207]. This success with AFM demonstrates the feasibility of accurately measuring small-scale mechanical torques and forces, opening new avenues for quantifying mechanical effects in magnetic systems.

However, several challenges must be addressed before AFM can be effectively used to measure the mechanical torque of single NPs. We need to validate its efficacy in measuring single NPs with a diameter of 120 nm, which generate relatively low torque in the order of 10^{-18} Nm. More sensitive cantilevers with higher spring constants may be required to improve signal detection. Additionally, differentiating between the effects of magnetic force and torque will require either the use of uniform magnetic fields or the development of medels to estimite the difference.

In conclusion, while AFM shows promise for measuring actual torque in NPs, further improvement and test of the technique are needed to fully realize its potential in this application area.

8.5 Mechanical response

Although, we have experimentally investigated the rotation of p-SAF NPs' chain under different field frequencies, the understanding of their rotation poses challenges. One major challenge lies in developing a better model to describe the dynamics of NP chains' rotation and NPs' aggregation into chain-like structures. This model needs to account for a broad range of factors, including magnetic, drag, and friction forces, as well as the intricacies of Brownian motion. Additionally, interparticle interactions, such as the forces experienced by the NPs as they approach each other, need to be considered. The model should also include the collective motion of these aggregated chains, which may attach to each other due

to dipolar interaction. While initial efforts have been devoted toward a simplified model, the complexity and extent of these interactions have to be considered to achieve a more realistic estimation.

In Chapter 7, we limited our study of field rotating frequencies to a maximum of 15 Hz due to our experimental setup constraints. The limitations stemmed from both the inability of our field generation setup to achieve higher frequencies and the camera's frame rate, which was insufficient for capturing images at these higher frequencies. To overcome these challenges, a setup capable of generating fields at higher rotating frequencies is essential. Additionally, employing advanced optical setups instead of microscopy would allow us to observe the rotation of chains under higher frequencies, avoid the frame rate limitations of our current camera[190,208].

Another aspect that requires attention is the interaction of NPs with more rigid mediums, such as cell membranes. While our primary focus has been on liquid environments, understanding how NPs behave and interact with solid or semi-solid environments is essential, especially for torque-related applications. For instance, in mechanical cancer cell destruction, determining how large the mechanical torque applied is, and how these NPs deform the cell membrane, is crucial for designing applications. Therefore, more experiments are needed to observe interactions with semi-rigid media.

Regarding the experiment setup, it is crucial to note that the interaction of NPs with the media or the rotation of NPs is three-dimensional (3D) rather than two-dimensional (2D). Therefore, an ideal setup would be a 3D field generator capable of generating fields in all directions. This setup would allow for the free alignment of NPs in any direction, providing a more comprehensive understanding of their motion.

8.6 Application

In this thesis, the practical applications of p-SAF NPs have not been extensively discussed. Future research could focus on their in-vivo applications, such as mechanical cancer disruption or the manipulation of ion channels in cells at a nanoscale. Additionally, for the implementation of these NPs within the human

body, toxicity studies and methods for their safe removal should be investigated[209].

Moreover, the potential for these NPs in in-vitro applications, such as microfluidic mixing, warrants attention. While we have demonstrated the rigidity of SAF NP chains and hypothesized their enhanced efficiency in mixing in Chapter 7, further empirical research is required to validate the efficiency.

Conclusion

In conclusion, this thesis has delved into the fundamentals of p-SAF NPs from their fabrication to fundamental physics. We have investigated their magnetic properties, characterized their magnetic switching behaviors, and examined their rotational responses under various field conditions. Our findings underscore the potential of p-SAF NPs in torque-related applications, laying the groundwork for future advancements. Nevertheless, this remains an emerging field with ample scope for further research and exploration.

A

Supplemental information for chapter III

A.1 Fabrication process of SAF NPs

A.1.1 Growth of the metallic stack

A 30 nm Cu thick sacrificial layer was first deposited on a 2 inch silicon wafer (<100> orientation, p-doted, from University Wafer) followed by the deposition of the metallic stack through DC sputtering. The deposition was conducted under the Ar pressure of 10^{-2} mbar in a chamber with a background vacuum of $\sim 10^{-9}$ mbar.

For 1.8 µm SAF NPs, [Ta(4)/Pt(2)/CoB(0.8)/Pt(0.3)/ Ru(0.8)/Pt(0.3)/CoB(0.8)/ Pt(2)]$_5$ (with the thickness in nanometer) was used. The metallic stack for 120 nm NPs was Ta(4)/Pt(2)/CoB(0.8)/Pt (0.3)/Ru(0.8)/Pt(0.3)/CoB(0.8)/Pt(2).

Five repetitions of the basic thin film stack ([Ta(4)/Pt(2)/CoB(0.8)/Pt(0.3)/Ru(0.8)/Pt(0.3)/CoB(0.8)/Pt(2)], with thickness in nanometer) were used for 1.8 µm NPs to increase the total thickness and thus prevent the roll-up of the NPs during the release step i.e. to increase its mechanical robustness. The SEM image of released 1.8 µm NPs with only one repetition of the basic stack is shown in Fig. 4.2. We observe that the sample edge rolled up after the selective etching of the sacrificial layer. The bending can be attributed to the stress difference between the top and bottom layers during etching[210]. With smaller aspect ratio (diameter/thickness), the bending can be prevented. For 120 nm Ns, the aspect ratio is much smaller and the single repetition is enough to form flat NPs. Naturally, increasing a non-magnetic layer thickness in the stack would provide the

same robustness, however on the first order the magnetic moment to volume ratio would be very different and hence the magnetic behavior would be different but is beyond the current scope and we decided to keep this ratio constant.

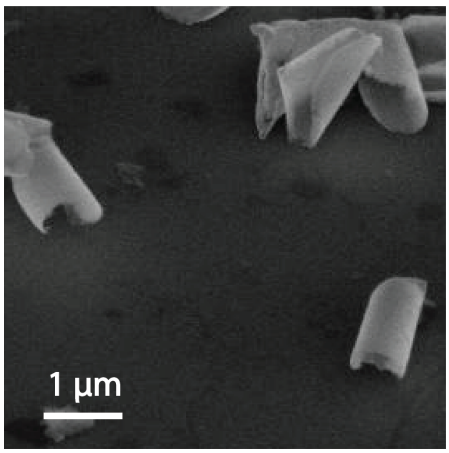

Figure A.1: SEM image of the released 1.8 µm NPs with one repetition of the basic stack.

A.1.2 Nanoimprint

A typical stamp used in the nanoimprint process is shown in Fig. A.2. The stamp consists of a thin glass substrate, on top of which two PDMS layers are attached. The bottom low modulus PDMS layer allows the conformal contact during imprinting. The top high modulus PDMS layer contains the designed patterns[139]. To create the pattern, the SiO_2 based sol-gel resist (from SCIL Nanoimprint Solution) T1250 and T1100 were used for 1.8 µm and 120 nm NPs. They were spin coated at a different speed, 1000 rpm for 10 s and 2000 rpm for 8 s for 1.8 µm and 120 nm NPs respectively, on the metallic stack. Immediately after spin coating, the corresponding stamp was pressed into the resist which attached firmly to the resist due to capillary force. The sample together with the stamp was then baked at 50 °C for 2 min. After the stamp was removed, the sample was baked at 50 °C for another 2 min. After nanoimprint, we created nicely repetitive pillars as shown in Fig. A.3 (a), which were used as the masks for metal etching afterwards.

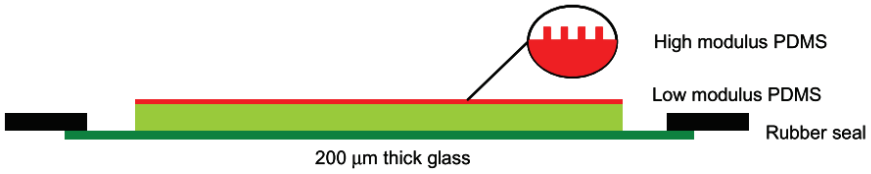

Figure A.2: Schematic of a typical SCIL stamp for nanoimprint.[139]

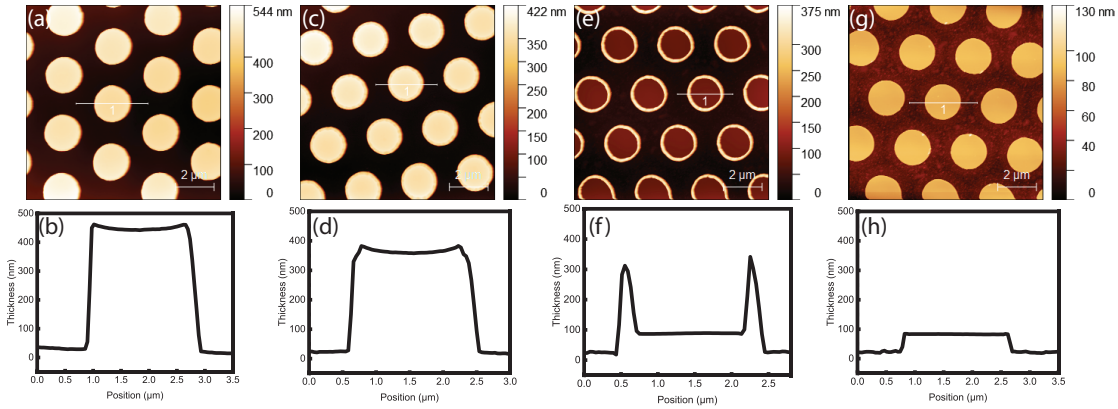

Figure A.3: AFM image of 1.8 µm SAF NPs (a) directly after imprint, (c) after IBM, (e) after BHF dipping (g) after sonication. (b), (d), (f) and (h) are the height profiles along the white line in (a), (c), (e), (f).

A.1.3 Pattern transfer into metallic layers

Some residual sol-gel resist was left between the designed patterns which should be removed first in order to conduct the following metal etching process. This was achieved by a short selective reactive ion etching (RIE) performed with 50 sccm CHF_3 and 5 sccm O_2 at a radio frequency (RF) power of 100 W. Since the height of the residual resist layer was different for 1.8 µm and 120 nm NPs, different etching periods of 90 s and of 84 s were used, respectively.

Nonselective ion beam milling (IBM) was used to pattern down the metallic layers from thin film to nanoplatelets. A two-step Ar+ ion beam was performed to etch the metal layers with a 40 mA beam current and accelerating voltage of 400 V. The sample was first etched by the ion beam normal to the sample surface and then etched 30 degree relative to the surface to reduce redeposition. The IBM milling was performed in 30 second exposures with 30 second cool down time in between. A temperature controlled sample stage at 20 degrees centigrade is

used with active heat exchange gas cooling the substrate. In this way we prevent "Annealing effects" during the IBM step.

To remove the residual resist on top of the metal NPs after IBM, the sample was immersed in a 30:1 buffered HF solution for 2 min.

During IBM processing, the etched atoms can deposit on the sidewall of the resist causing irregular sidewalls namely redeposition. One example is shown in Fig. A.3 (e), where the AFM image of 1.8 µm NPs after HF etching is measured. To get rid of the redeposition, samples were further sonicated in DI water for 20 min which removed the sidewalls as shown in Fig. A.3g.

A.1.4 Release of the NPs

After sonication, the sample was immersed in 1.5% CuSO4 – 10% ammonia solution with sonication to dissolve the sacrificial Cu layer. The solution was then neutralized with citric acid. Finally, the NPs were collected through centrifugation. To clean the NPs, the collected NPs were redistributed in DI water and collected with centrifugation three times.

A.1.5 Morphology of 1.8 µm SAF NPs during Fabrication

The morphology of 1.8 µm SAF NPs after nanoimprinting, after IBM, after BHF dipping, and after sonication was measured under AFM and shown in Fig. A.3. Through nanoimprinting, we can obtain pillars consisting of resist with homogeneous diameter as shown in Fig. A.3 (a).

A.2 Yield of SCIL

The packing density, which is the total area of the NPs divided by the total surface of the sample, is calculated from the SEM images of the sample before release shown in Fig. A.4, where the red box is defined as the unit cell to represent the whole sample. For 1.8 µm NPs, the unit cell is the parallelogram formed by any four NPs next to each other. For 120 nm NPs, the unit cell is the square defined by the vertical bisector of adjacent NPs. The packing density is then defined as:

$$Packingdensity = \frac{S_{NP}}{S_{unitcell}} \tag{A.1}$$

where S_{NP} is the area of the NP and $S_{unitcell}$ is the area of the red box. The packing density we deduce for our stamps is 34 % and 11% for 1.8 µm and 120 nm NPs.

Knowing the packing density, we can calculate the number of particles obtained from a 2 inch wafer, which are $\sim 10^8$ particles for 2 µm NPs and $\sim 10^{10}$ particles for 120 nm NPs.

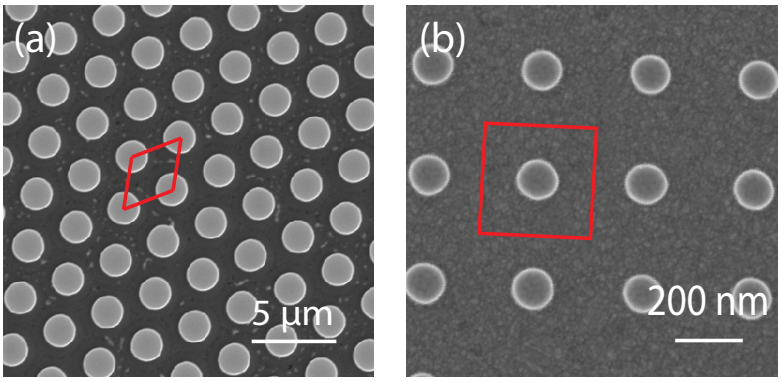

Figure A.4: SEM images of (a) 1.8 µm diameter and (b) 120 nm diameter SAF NPs before release. The red box is the smallest unit which we used to calculate the packing density.

A.3 Magnetic properties of NPs after etching

To investigate the effect of etching processes on the magnetic properties, the hysteresis loops of the 1.8 µm SAF NPs after different etching steps were measured and compared in Fig A.5. Three samples were measured. 1. the sample after IBM process. 2. the sample after immersing in buffered HF (BHF) and sonication in DI water. 3. the sample after immersing in $CuSO_4$ – ammonia solution for 1 hour without sonication during the step. Note without sonication the NPs were still on the wafer. All the measured hysteresis loops show the same SAF properties: two distinguishing switches and the antiferromagnetic state. The saturation magnetization is 967 kA/m, 1025 kA/m and 920 kA/m for the sample after IBM, after immersing in BHF and after immersing in $CuSO_4$ – ammonia solution, respec-

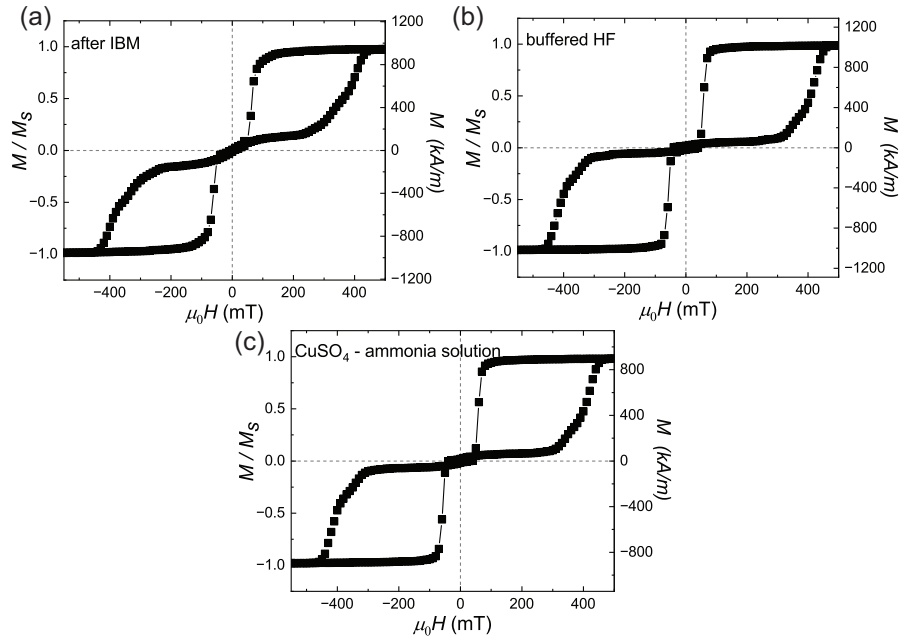

Figure A.5: Hysteresis loops measured along the easy axis through SQUID of the 1.8 µm NPs (a) after IBM, (b) after immersing in buffered HF and sonication (c) after immersing in $CuSO_4$ – ammonia solution.

tively. The difference is within the measurement error. Considering the obvious SAF properties and the similar saturation magnetization, we can conclude that neither the BHF solution nor $CuSO_4$ – ammonia solution degrade the magnetic properties.

A.4 Methodology

A.4.1 Preparation of released NPs

After the NPs were cleaned and dispensed in DI water, we dropped cast a part of the solution onto a clean Si-substrate. The samples were dried until the solution was fully evaporated at room temperature without applying an external magnetic field. The samples were ready for SEM measurement after drying. For SQUID measurement of released NPs, the samples were further spin coated with photoresist MaN2410 at 3000 rpm for 1 min to prevent the NPs from contaminating the SQUID during measurement.

A.4.2 SQUID measurement

It has been reported that the sample geometry (shape and size) and orientation can affect the measured magnetization in SQUID[211]. In our measurement, samples with dimension around 4x4 mm^2 are used. The sample is aligned horizontally in easy axis (EA) hysteresis loop measurement and vertically in hard plane (HP) hysteresis loop measurement. Considering the shape effect and the orientation, the raw data was divided by a correction factor of 1.145 for EA hysteresis loop measurement and 1.004 for HP hysteresis loop measurement to compensate for the effect acctording to the application note[211].

A.4.3 Size distribution of NPs

To obtain the size distribution of the SAF NPs, the diameter of the NPs before release was collected by ImageJ from several SEM images at different positions on the wafer. One example of the SEM images is shown in Fig. 4.2 (b) and (f). In total 432 NPs were used to calculate the distribution of the 1.8 µm NPs and 1109 NPs for the 120 nm NPs.

A.4.4 Switching field distribution (SFD)

In SQUID measurement, an assembly of particles is measured, from which there is a distribution of the switching field. To get the SFD, an error function is used to fit for the switching filed ($\mu_0 H_1$ and $\mu_0 H_2$) in the minor loop shown in Fig. A.6. The standard deviation SD_1 and SD_2 in the fitting is defined as the SFD of $\mu_0 H_1$ and $\mu_0 H_2$ respectively. We use the average of SD_1 and SD_2 as the SFD of the sample.

A.5 Error calculation

The standard deviation of $\frac{\mu_0 H_2 - \mu_0 H_1}{2}$ and $\frac{\mu_0 H_2 + \mu_0 H_1}{2}$is regarded as the error for the coercivity ($\mu_0 H_c$) and the RKKY coupling field ($\mu_0 H_{rkky}$). An example to calculate the error is shown in Fig. A.6. From the fitting, $\mu_0 H_1$ and $\mu_0 H_2$ at each y value can be calculated and thus $\frac{\mu_0 H_2 - \mu_0 H_1}{2}$ and $\frac{\mu_0 H_2 + \mu_0 H_1}{2}$. The mean and SD

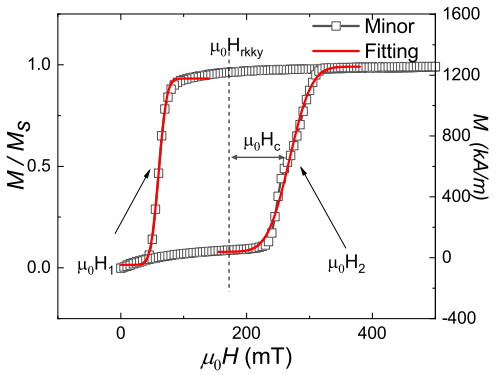

Figure A.6: Minor hysteresis loop of 1.8 µm NPs before release.

of the filed are obtained based on these values at different y value.

B

Supplemental information for chapter IV

B.1 Nanofabrication of SAF-PMA and dispersion in a liquid

A substrate conformal imprint process was used to fabricate the SAF-PMA nanoplatelets (NPs) which were studied in the paper.[127] After depositing the sacrificial Cu layer and the SAF thin film stack on a 2-inch silicon wafer, the disc shape was created by the imprint process. Several etching processes e.g. reactive ion etching, ion beam milling and buffered hydrogen fluoride etching were used to transfer the disc shape into the metal layer. Then the Cu layer was dissolved by $CuSO_4$-ammonia solution to release the NPs. After release into the liquid environment, the NPs were cleaned with deionized (DI) water three times. Then the NPs were redistributed in the DI water with sonication. For the SEM measurement, the released NPs were prepared by spin coating the solution which contained the NPs on a silicon wafer at 500 rpm. For the unreleased sample, a piece of wafer of the sample before release was used.

B.2 Size distribution of nanoplatelets

The size distribution of nanoplatelets is calculated based on the TEM image of 146 released nanoplatelets. To prepare the TEM sample, the nanoplatelets were dispersed in DI water and drop cast on a TEM copper grid. One example of the TEM image of the released NPs is shown in Fig B.1(a). Only the NPs which were fully aligned on the substrate were taken into consideration. ImageJ was used to analyze the diameter of the NPs and a histogram of the diameters of the nanoplatelets is shown in Fig. B.1(b). A normal distribution is used to fit the

diameter and we obtain a size distribution of 122 ± 4 nm.

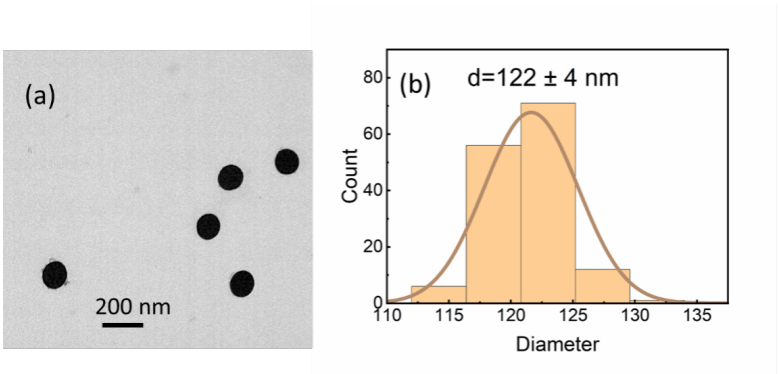

Figure B.1: (a) TEM image of released SAF nanoplatelets. (b) Histogram of the diameters of the nanoplatelets. A normal distribution is used to fit the histogram.

B.3 SQUID measurement

The SQUID measurement of the SAF nanoplatelets was conducted on the unreleased NPs, which were still on the silicon wafer, instead of the released NPs. A 4×4 mm^2 wafer piece of the unreleased sample was used in the measurement. Considering the filling rate of NPs shown in Fig. 5.1b, in total $\sim10^6$ SAF nanoplatelets were measured. A magnetic field was applied perpendicular to the sample surface. The reason for using unreleased nanoplatelets is to prevent the misalignment of the dried-in nanoplatelets relative to the applied field and the possibility of nanoplatelets piling on top of each other, which can cause more slanted switching fields due to particle-particle interaction.[127] Previous study also denotes that after release the typical SAF properties do not degrade,[127] indicating that the properties of unreleased nanoplatelets measured by SQUID can be compared with the properties of released nanoplatelets measured by PT MCD.

B.4 Error function fit to the magnetization curve obtained from SQUID

In the SQUID measurement, the ensemble average switching behavior of more than 10^6 particles was measured. Since the switching process is a stochastic process, an error function ($y = A \cdot erf(\frac{x-B_{sw}}{\sqrt{2}SD}) + B$, where A and B are constants and B_{sw} is the average switching field and SD is the standard deviation) was used to fit for part of the hysteresis loop as shown in the insert of Fig. 5.1c. The

standard deviation of the fit represents the switching field distribution (SFDs) of the ensemble, dominated by NP to NP variation. Moreover, as SQUID is a quasi-static measurement process, i.e., field is set, a measurement is performed, etc, the time interval between two points is on the order of 20 seconds. In the PT MCD measurement a continuous measurement protocol is used, i.e., the field changes continuously and points are measured while sweeping (the magnetic field is varied by moving the external magnet away from, or towards, the sample with a speed of 0.5 mm/s and the magnetic field is calculated from a calibration curve of field-distance measured with a Gauss Meter). Hence, the quasi-static SQUID does not probe the SFD of the individual NP (more time to perform a switch i.e., Arrhenius type of process see Eq. B.2, but probes the distribution in the ensemble. In contrast the PT MCD protocol, where a continuous measurement is performed, which for an Arrhenius process leads to a larger spread as the measurement time is shorter, indeed probes the switching process of individual NPs and reflects the single-particle SFD.

B.5 Hysteresis loop of a continuous SAF film

The hysteresis loop of the as-deposited continuous film of the SAF stack before patterning is measured by SQUID at 400 K as shown in Fig. B.2. SAF properties are observed with the B_{rkyy} of 171 mT. Sharp switches with the SFD of 2 mT from AP to P state and P to AP state are observed compared to the patterned SAF NPs which exhibit a broad SFD of 10 mT (see Fig. 5.1c). The B_c of patterned NPs is 22 mT while the B_c of the continuous field is 2 mT. The differences between the continuous film and the patterned NP are expected and can be attributed to the reversal mechanism. Since the switch starts with a reversal of nucleation followed by fast domain wall propagation, sharp switches are expected as we observed on the continuous film and on the individual NPs. However, the SQUID measurement of the patterned NPs contains many NPs thus the broader SFD can be observed. With reduced area, less nucleations can be found on the patterned sample compared to the continuous film leading to a larger B_c of the patterned SAF NPs.

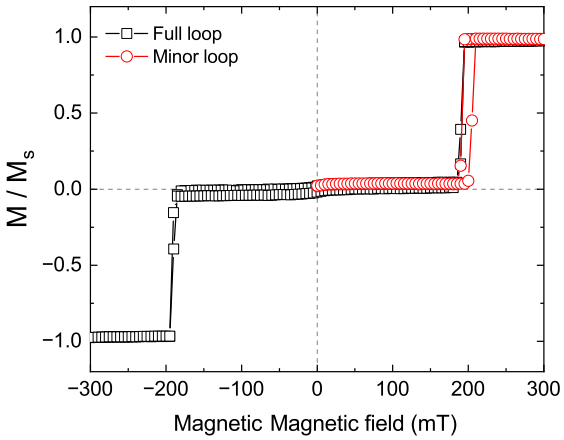

Figure B.2: Hysteresis loop of the as-deposited continuous film SAF stack at 400 K

B.6 Histogram of PT signals and g_{CD} factors

Histograms of photothermal (PT) signals and g_{CD} factors of 32 single magnetic nanoplatelets at a saturated magnetic field are shown in Fig. B.3. The g_{CD} factor is defined as

$$g_{CD} = \frac{CD}{PT} = 2\frac{\sigma_L - \sigma_R}{\sigma_L + \sigma_R} \tag{B.1}$$

Where, g_{CD} factor is the normalization of CD signal by PT signal. σ_L and σ_R is the absorption cross sections of left- and right-circularly polarized light, respectively.

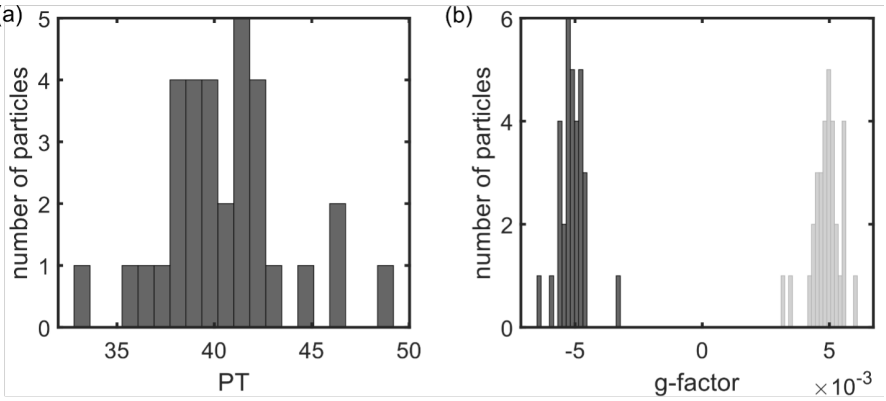

Figure B.3: (a) Histogram of photothermal signals of 32 single magnetic nanoplatelets. (b) Histograms of g_{CD} factors at saturation magnetic fields of 280 mT (black) and -280 mT (gray).

B.7 Calculation of temperature in PT MCD using a calibration method

The temperature calibration was done by heating the nanoplatelets until nanobubble formation was observed in the liquid (Hexane) surrounding the NPs. The hexane has a lower boiling point (341.6 K) than hexadecane (560 K) and was used as the contrast medium for this calibration. We performed the calibration with the following assumptions:

1. The nanoplatelets are assimilated to spheres.

2. The absorption cross section for the heating beam and for the probe beam are approximately equal.

3. The thermal conductivity and refractive index of hexane and hexadecane are nearly identical.

Then, we increase the heating power slowly until the PT signal suddenly increases significantly, which indicates nanobubble formation. Considering surface tension and size of the NP, the critical temperature of NP from calculation is 377 K. The critical power of heating and probe beam used in experiments are 7.5 mW and 1 mW, respectively. Because of the linear relationship between heating power and the temperature of nanoplatelet, the estimated temperature of nanoplatelet in hexadecane is 390.28 K with a heating power of 12 mW and probe power of 1 mW.

B.8 Temperature dependent switching fields

Hysteresis loops were obtained by SQUID at temperatures ranging from 200 K to 400 K with an out-of-plane configuration on an ensemble of approximately 10^6 particles in a periodic configuration on a 4×4 mm^2 wafer piece. The measurements were performed several times over multiple days. Next to that, the temperature was first increased and then decreased for several times by which it was concluded that there was no irreversible effect observed in the magnetic properties for temperatures ranging up to 400 K. The switching fields of the minor loop as a function of the temperature are recorded in Fig. B.4, the corresponding coercivity (B_c) and RKKY coupling field (B_{rkky}) are shown in Fig. B.5a and Fig. B.5b. The error bars of the B_c and B_{rkky} come from the standard deviation of the values obtained from different measurements. We observe a decreasing coupling field with an increase in temperature as shown in Fig. B.5b, due to the switching fields moving closer together as can be seen in Fig. B.5.

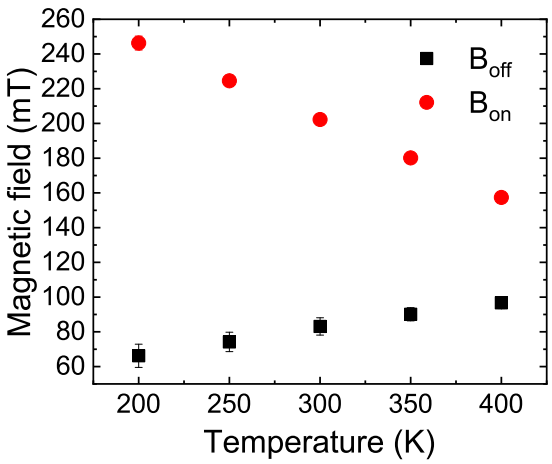

Figure B.4: Temperature dependent switching fields (B_{on} and B_{off}) measured by SQUID.

Besides that, the B_c is also decreased with an increase in temperature, which is the result of the thermally assisted switching behavior. The decrease in B_c can be fitted with the Sharrock formalism,

$$B_c = \frac{2K}{M_s}\left(1 - \sqrt{\frac{k_B T}{KV} ln\left(\frac{f_0 t}{ln2}\right)}\right) \tag{B.2}$$

Here B_c is the coercive field, K is the anisotropy constant, M_S is the saturation magnetization, k_B is the Boltzmann constant, T is the temperature, V is the nucleation volume, f_0 is the attempt frequency and t is the measurement time. From this equation it follows that for finite temperatures the coercive field is reduced by the factor in brackets with respect to the anisotropy field $\frac{2K}{M_S}$. For the fitting, f_0 , t and k_B are fixed, where f_0 is set to 10^{10} Hz (typical for ferromagnets as CoB) and t is set to 20 s (∼measurement time between points in the SQUID). Furthermore, it is assumed that both K and M_S have no temperature dependence which is a rather crude assumption for ultrathin CoB layers with a Curie temperature of ∼550 K. The fitting parameters are then $\frac{2K}{M_S}$ and KV. The fitting gives that $\frac{2K}{M_S}$ equals 240 mT and KV equals 1.9×10^{19} J. According to the fitting, the B_c at 390 K is 33 mT, which agrees nicely with the value obtained in the PT MCD.

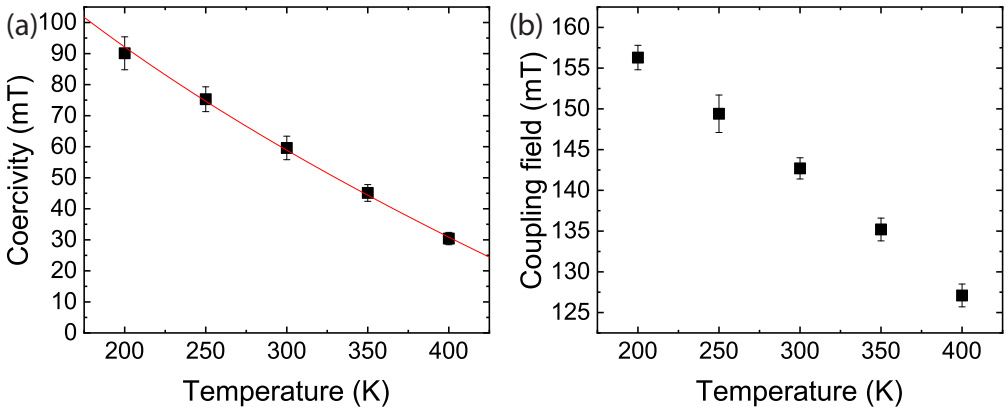

Figure B.5: (a) Average temperature-dependent coercivity of an ensemble of ∼10^6 platelets as obtained from the minor loops measured using SQUID. The data points are fitted using the Sharrock formalism as mentioned in the text. (b) Average temperature-dependent coupling field of an ensemble of ∼10^6 platelets as obtained from the minor loops measured using SQUID.

B.9 Sample preparation for PT MCD measurements

The nanoplatelet solution was spin-coated on a UV-plasma-cleaned glass coverslip (thickness about 170 µm) to disperse the nanoplatelets homogeneously on the glass surface. The glass coverslip was sandwiched with a microscope glass slide with a cavity (glass slide's thickness of about 1.4 mm) which contained a cavity to hold the liquid (hexadecane, Sigma-Aldrich, MGPB20) used for the photothermal measurement.

B.10 Optical setup

The details of the optical setup are described in our recent publication[124]. Here we describe the setup briefly. The heating laser with wavelength of 532 nm was passed through two polarization modulators, an electro-optical modulator (EOM) and a photo-elastic modulator (PEM) to modulate the laser's polarization at frequencies 33.5 kHz and 50 kHz, respectively. The circular dichroism (CD) signal was detected at the sum frequency. The heating laser was focused in the back-focal plane of the immersion-oil objective (NA = 1.45) to illuminate the sample in a widefield area of about 3 m diameter. The circularly polarized continuous-wave probe beam at wavelength 780 nm was focused onto the sample using the same microscope objective. The scattered probe beam was filtered from the heating beam using a band-pass filter (BP780) before focusing on an analog photodiode using a lens. A sensitive lock-in amplifier was used to obtain the CD signal at the sum frequency of two modulators. To vary the magnetic field, a long permanent cylindrical NdFeB magnet made from a set of small cylindrical magnets of diameter of 6 mm, was placed perpendicular to the sample plane and its position relative to the sample was varied to vary the applied magnetic field. The magnetic field was calibrated with a Hall probe (Hirst Magnetics, Model: GM07). The field was measured without the objective (the presence of the steel ring in the microscope objective may modify the magnetic field in the sample, however the influence of the steel ring was not considered due to the position of the ring several millimeter away from the sample). To invert the direction of the magnetic field, the magnet was reversely mounted. Note that PT MCD is most suitable for nanoparticle measurements and not very suitable for a thick film measurement. For a film

measurement, it is quite complex to quantitatively understand and requires an additional theoretical modeling.

B.11 Measurement sequence of applied magnetic fields in PT MCD measurements

Upon measuring the hysteresis loop of NPs through PT MCD, g_{CD} factors under different applied fields, defined as CD signal normalized by PT signal, are recorded. A high positive magnetic field was applied to saturate the sample, then the applied magnetic field was varied from zero to high magnetic field, then returned to zero and then the same was done for the opposite orientation of the magnetic field. Thus, the hysteresis loops in both positive and negative magnetic field directions resemble the minor loop of the hysteresis curve measured by SQUID. Note that, in this study, we focus on the minor loops of the system, i.e., single-polarity sweeps of the field which will assure that only one of the two layers of the SAF system switches which allows us to compare the same switching event consistently.

B.12 Full magnetization curves of 32 single magnetic nanoplatelets

The full magnetization curves of a total of 32 single magnetic nanoplatelets are shown in Fig. B.6 and Fig. B.7. All the platelets show sharp transitions from one of the anti-ferromagnetic configurations (on switch) to the ferromagnetic one and always reverted to an anti-ferromagnetic configuration upon field decrease (off switch).

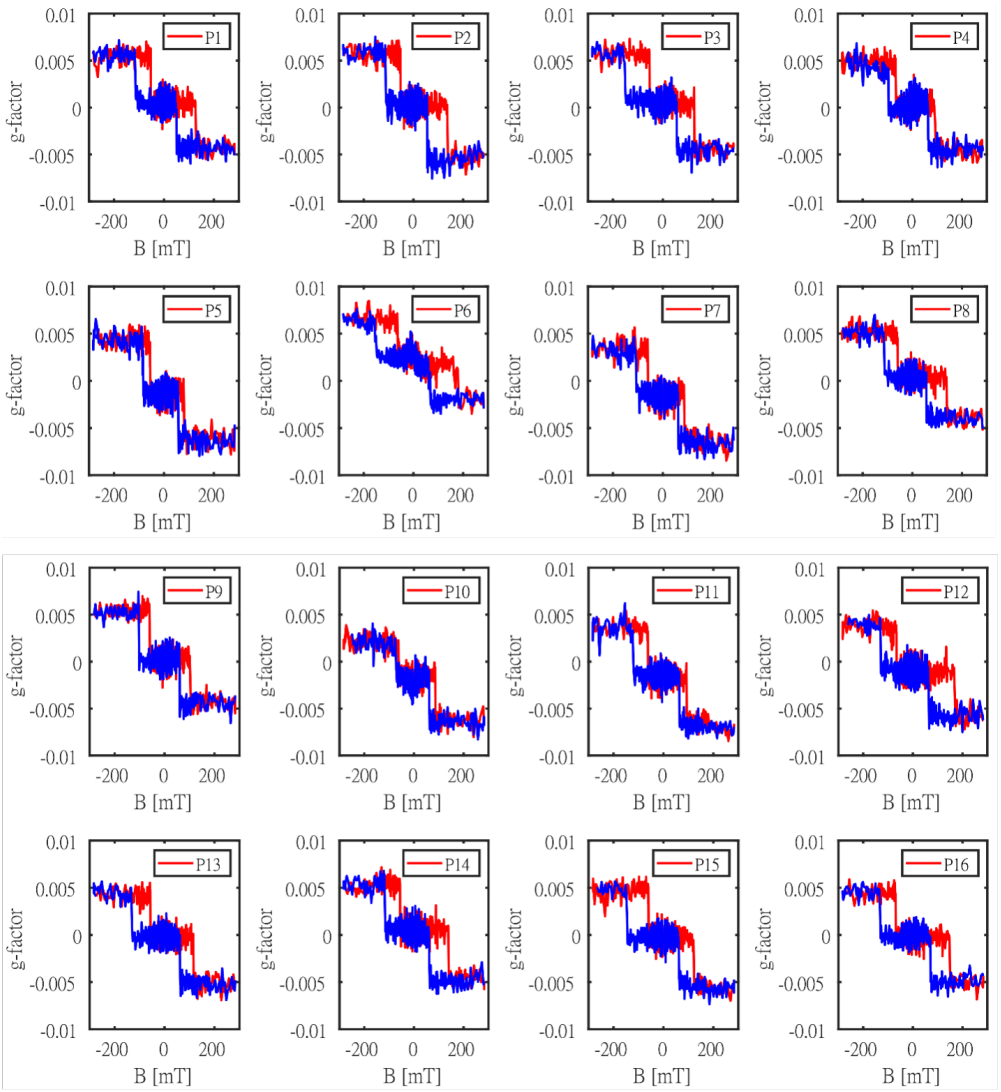

Figure B.6: Full magnetization curves of 16 single magnetic nanoplatelets. Magnetization curves of another 16 single nanoplatelets are shown in Fig. B.7. Particles numbers are mentioned in the inset.

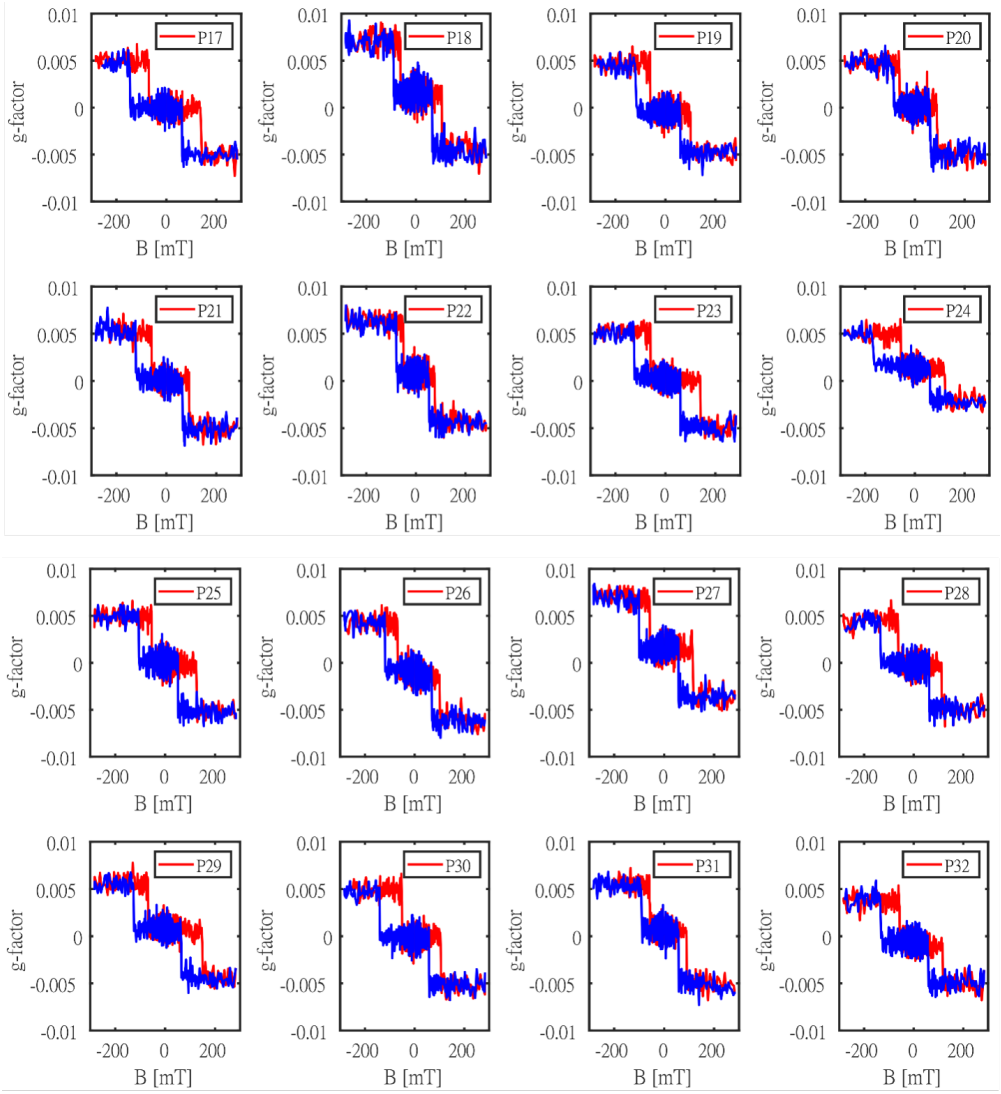

Figure B.7: Full magnetization curves of another 16 single magnetic nanoplatelets. Particles numbers are mentioned in the inset.

B.13 Magnetization as a function of the permanent magnet's position

Figure. B.8 shows magnetization curves of the four single magnetic nanoplatelets shown in Fig. 5.2 in the main text. Here, we plot the optical MCD signal as a function of the position of the permanent magnet from the sample, instead of the magnetic field. There is no change of noise amplitude on this plot, which demonstrates that the higher apparent noise at lower magnetic fields in the magnetization curves of Fig. 5.2 in the main text is an artefact. Because we measure

with a constant stepping in magnet position, we obtain a much denser sampling of weak fields at large distances compared to the sampling of high fields at short distances (e.g., the field generated by a permanent magnetic is non-linear in its distance to it).

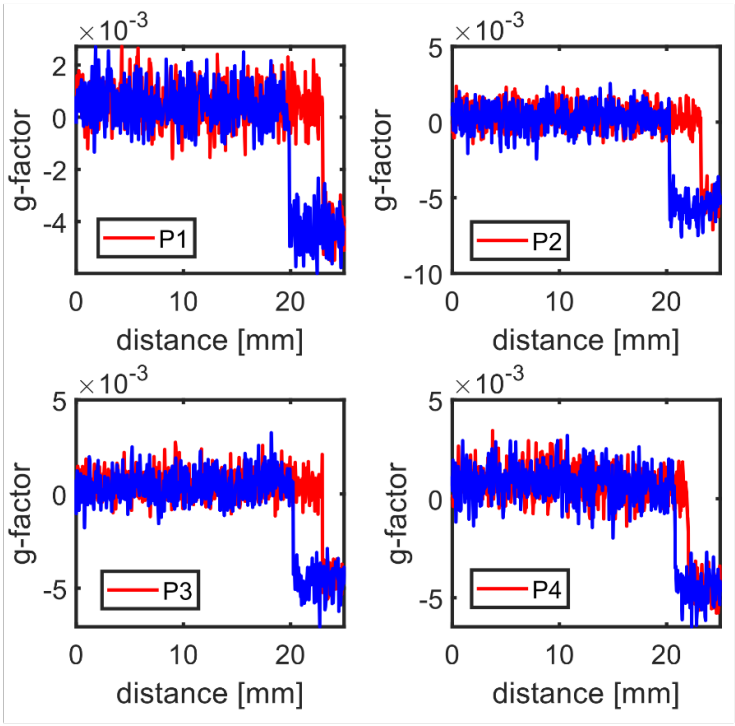

Figure B.8: Magnetization curves of the four nanoplatelets shown in Fig. 5.2 in the main text. Here, the MCD signal is plotted as a function of the distance of the magnet from the sample, only in the positive magnetic field direction.

B.14 MCD time traces at $B = 0$ and $B = 280$ mT

Figure. B.9 shows time traces of the MCD signal at $B = 0$ mT and $B = 280$ mT. Both time traces show similar noise levels. This again confirms that the higher noise level at lower fields apparent in Fig. 5.2 is only due to the larger number of data points at lower than at higher fields.

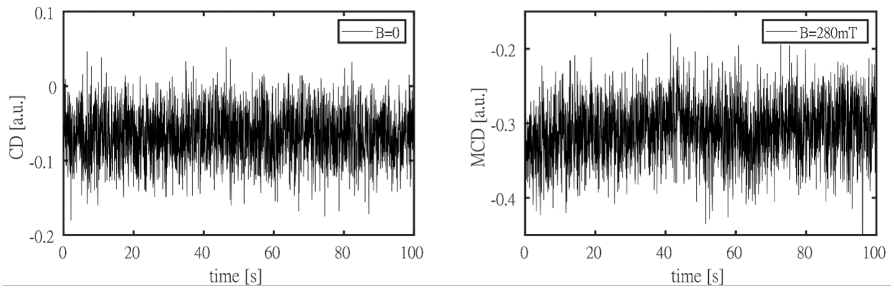

Figure B.9: (Left) CD time trace at B= 0 and (b) MCD time trace at B= 280 mT for a single magnetic platelet.

B.15 Histogram of on and off switching fields from time-dependent magnetization curve

Figure B.10 shows the histogram of on and off switching fields of minor loops of a single NP measured over 15 sequential cycles as presented in Fig. 5.5 in the main text. The mean values and standard deviations of the histograms are mentioned in the inset. The distribution of on switching fields is broader than that of the off switching fields.

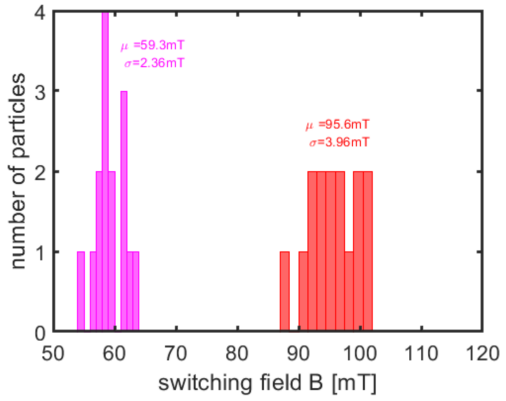

Figure B.10: Histogram of off (magenta) and on (red) switching fields of minor loops of a single NP measured over 15 cycles as shown in Fig. 5.5 in the main text. The mean value (μ) and standard deviation (σ) is mentioned in the inset.

B.16 Simulation for calculating absorption of magnetic layers

An analytical calculation based on the transfer matrix method is used to estimate the optical absorption of each layer of the NPs[212]. The complex refractive indexes

of different materials at the wavelength 532 nm, which is the wavelength used in PT MCD measurement, are used in the simulation[213]. Here we use the refractive index of Co to represent the CoB layer. In the simulation, we assume that the laser enters the platelet from the top side of the NP from air and has the following stack AIR /Ta(4)/Pt(2)/Co(0.8)/Pt(0.4)/Ru(0.8)/Pt(0.4)/Co(0.8)/Pt(2)/Ta(4)/AIR. The absorption of the laser of each layer is shown in Fig. B.11. From the estimation, only 8.7 % of the light is absorbed in the two Co layers (4.5% in the first layer and 4.2% in the second layer) which will contribute to the MCD signal. Note that only 41.1% of the incoming light will be absorbed in the layer stack of the platelet (integrated absorption) as its thickness is less than the penetration depth of the light.

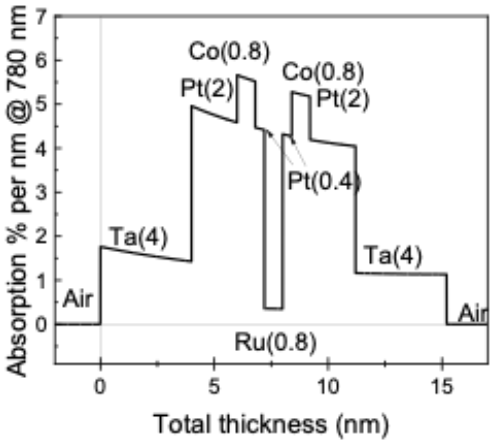

Figure B.11: The absorption of the heating laser by the NP stack

B.17 The effect of dipolar field on the unreleased SAF NPs in SQUID measurement

As shown in Fig. B.12, the unreleased SAF NPs are well aligned on the substrate with a constant distance of 335 nm between the two NPs. Dipolar fields from nearby NPs may influence the switching of NPs. When the external field is low, NPs are in the antiferromagnetic state leading to zero dipolar fields and thus not affecting the surrounding NPs. When NPs are saturated, the total dipolar fields at the central NP (in the red circle) are calculated as shown in Fig. B.12. Note that we did not include NPs beyond 2 µm from the central NP, since their dipolar

fields on the position of the central NP are negligible. In addition, we calculate the field on the center of the central NPs. For a small area of the saturated NPs, the magnetic flux which is perpendicular to the substrate on the central NP is

$$\Delta B = \frac{\mu_0}{4\pi}\frac{\Delta m}{r^3} = \frac{\mu_0}{4\pi}\frac{M_s t \cdot \Delta area}{r^3} \tag{B.3}$$

where M_s is the saturation magnetization of CoB which is 1120 kA/m, t is the total thickness of the magnetic material which is 1.6 nm, r is the distance from the center of the central NP. By integrating on the area of all the NPs (except the central NP), we obtain a field of 0.5 mT. Considering the small value, we can neglect the effect of the dipolar field of neighboring NPs.

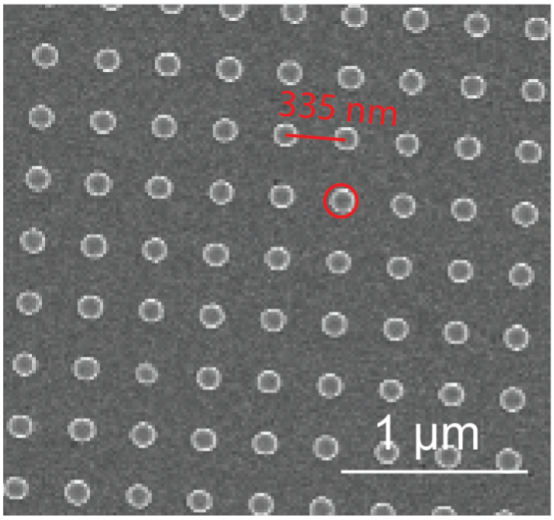

Figure B.12: SEM of unreleased SAF NPs, which was used in SQUID.

B.18 Schematic representation of the spin reversal mechanism

The switching mechanism of ultrathin CoB PMA layers is known to start with the nucleation of small reversed areas[178]; these domains can then expand rapidly due to domain wall (∼10 nm width in PMA systems) motion as the domain wall mobilty is high[102]. The initial nucleation process is a stochastic process and depends on the history and detailed morphology at the nanoscale for the ultrathin CoB layer. Although the layers in the PMA-SAF stack are polycrystalline, the nucleation of the NPs is dominated by the strongest defect and our results show

that this distribution is well defined. However to fully grasp the difference between the reversal of the on and off switch of the individual NP we first discuss the case of homogenous CoB layers in the NP and the effect of the generated dipole fields in the on and off state. Then we explain the effect of microstructure by including so-called nucleation embryos (strongest defects or hysteretic residuals of not fully reversed nanocrystals from the former saturation) where the stochastic domain nucleation happens and is followed by domain wall propagation.

The scheme in Fig. B.13 represents the orientation of the magnetic moments in the two ferromagnetic layers of the nanoplatelet in the parallel (P) and anti-parallel (AP) states. Figure B.13 shows the ideal arrangements of the dipoles in the absence of any nucleation embryos. The same arrangement can be perturbed by the presence of some nucleation embryos. These schemes are meant to explain two observations on the minor hysteresis loop: (a) the much higher switching field in going from AP to P than when returning from P to AP; (b) the larger dispersion of switching fields when going from AP to P than when returning.

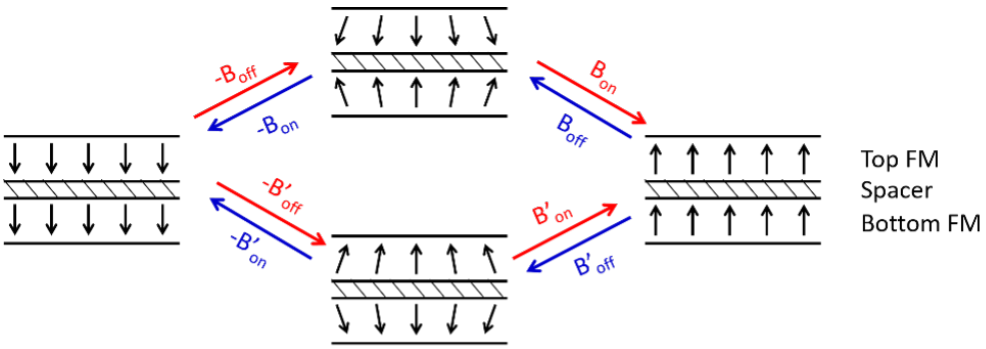

Figure B.13: Two ferromagnetic layers antiferromagnetically coupled by the Ru spacer layer present anti-parallel (AP) states as represented in the middle and parallel (P) states as represented in the left and right. They are schematized in the absence of nucleation embryos and other defects. The red and blue color of the arrows representing the hysteresis loop of single particle PT MCD measurements. For the switching from the AP state to P state (B_{on}), the dipole field leads to canting of magnetization at the edge and assists the switching, whereas, for the switching from P state to AP state (B_{off}), the dipole fields are already aligned and do not contribute to the switching process.

In the AP state, the generated dipole field of the two ferromagnetic layers has a component in the plane of the films which increases the switching probability at the edges of the NP. This will act as more active nucleation areas and hence the

switching to the P arrangement is favored. In the inverse transition, when the field is lowered, the dipole field at the edges is collinear to the OOP direction. Hence, in this alignment there is no assistance of the dipolar field to the switching probability at the B_L (or B_{off}) switching field.

For the case of the same process in the presence of defects and nucleation embryos, the perturbations and stray fields created by these embryos will shift the switching fields B_{on} and B_{off} by random quantities, leading to a spread of switching fields when moving from particle to particle, or even, to a lesser extent, when repeating measurements on the same particle. Due to a lower sensitivity of the low switching field B_{off} to defects, the dispersion in this low switching field is lower.

C

Supplemental information for chapter V

C.1 SEM images of SAF islands

The SEM images of SAF islands with varying sizes are presented in Fig C.1. The distance between each island is the same as its diameter.

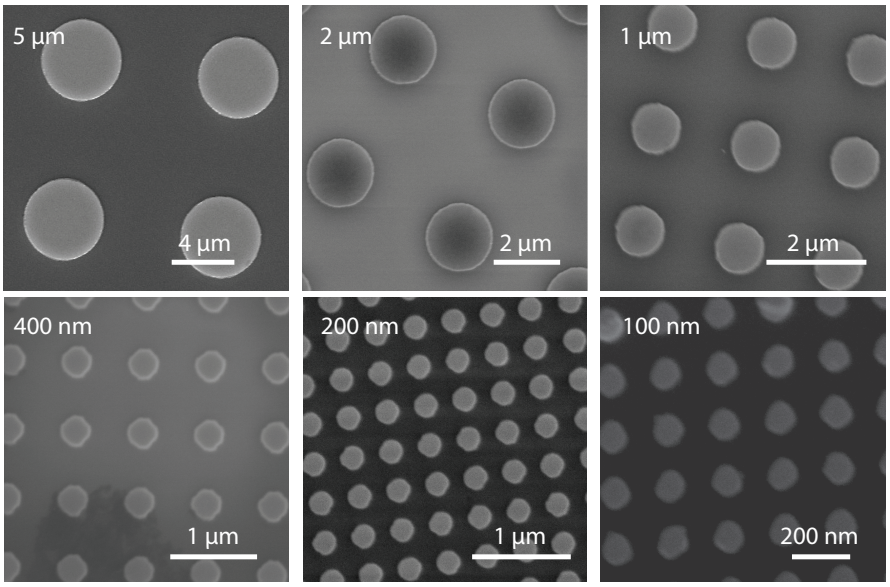

Figure C.1: The SEM image of SAF islands with different diameter

C.2 Laser spot size

The laser was scanned across a knife edge of the thin film sample to obtain the laser spot size. The intensity and the corresponding derivative as a function of scanning distance are shown in Fig C.2. The derivative is then fitted with a

Gaussian function from which the full width at half maximum (FWHM) of 137 µm is obtained. This FWHM is used as the laser spot size.

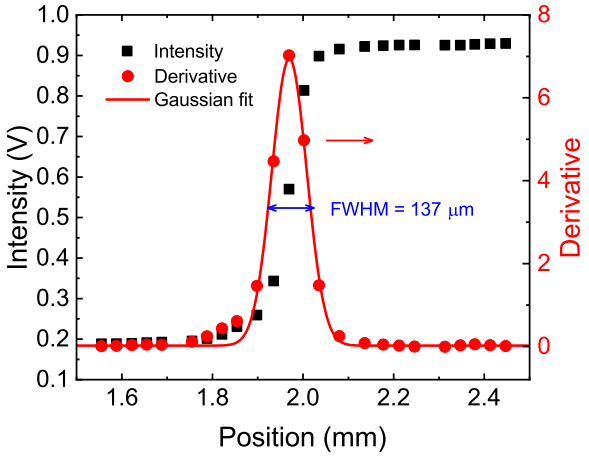

Figure C.2: The intensity of the laser used in MOKE as a function of position. The FWHM of 137 µm is obtained through the Gaussian fit

C.3 Effect of dipolar field

At a low external field, SAF islands are in an antiferromagnetic state leading to negligible dipolar fields that have no significant impact on the neighbouring islands. However, as these islands switch to the on state, where the magnetization aligns in the same direction, cumulative dipolar fields are generated by neighbouring islands, impacting the central island. To assess the perpendicular magnetic flux on the central island, the following equation is utilized:

$$dB = \frac{\mu_0}{4\pi}\frac{\Delta m}{r^3} = \frac{\mu_0}{4\pi}\frac{M_s t \cdot dA_{area}}{r^3} \tag{C.1}$$

where M_s is the saturation magnetization, t is the total thickness of the magnetic material which is 1.6 nm, and r is the distance from the center of the central island. The integration is carried out over the area of all neighbouring islands except the central island. In our analysis. We have included the impact of neighboring islands up to the 100th order while neglecting the contribution of islands beyond this range, as their dipolar fields exert a negligible impact on the central island. Additionally, we assume that the dipolar field acts at the center of the central

islands.

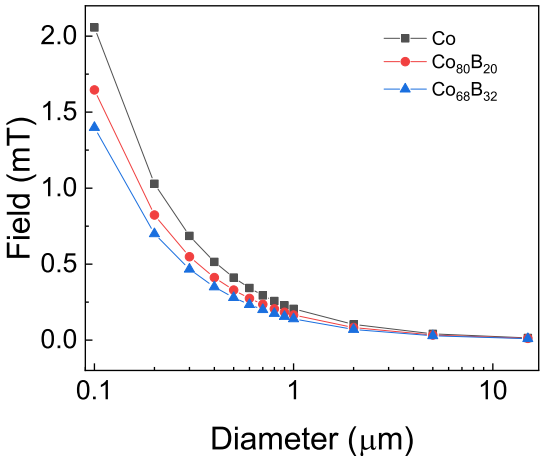

Figure C.3: The dipolar field generated by the surrounding islands on the center island when saturated as a function of the diameter of island.

C.4 Anisotropy and Magnetization

To determine the anisotropy and magnetization characteristics of the sample, hysteresis loops were measured for the SAF thin films with varying $Co_{1-x}B_x$ compositions through VSM-SQUID (see Fig. C.4). These hysteresis loops were obtained by applying external fields both parallel (easy-axis loop) and perpendicular (hard-plane loop) to the easy axis of the SAF structure. To calculate the effective perpendicular anisotropy (K), a well-established method outlined in the referenced work[127] was followed. The saturation field ($\mu_0 H_{sat}$) is related to the anisotropy field ($\mu_0 H_k$) and the RKKY interaction field ($\mu_0 H_{rkky}$) by the equation $\mu_0 H_{sat} = \mu_0 H_k + 2\mu_0 H_{rkky}$. K is then given by $K = \frac{H_k M_s}{2}$. M_s and $\mu_0 H_{rkky}$ are obtained from the easy-axis hysteresis loop. $\mu_0 H_{sat}$ is obtained from the hard-axis hysteresis loop, which is defined as the crossing point of the saturated state and a linear fit of the data. Due to the s-shape of the hysteresis loop, determining K is a challenge. Here, we considered two ranges of x data to estimate K for $Co_{1-x}B_x$ sample: 1) from -1000 mT to 1000 mT, and 2) extending the x-axis to include the saturation point, which varies by sample (see the green line in Fig. C.4). The range leads to the error in K.

As depicted in Fig.C.3, the magnetic field generated by the surrounding islands is found to be consistently smaller than 2.1 mT across all cases. Given its small magnitude, we neglect the dipolar field from neighbouring islands.

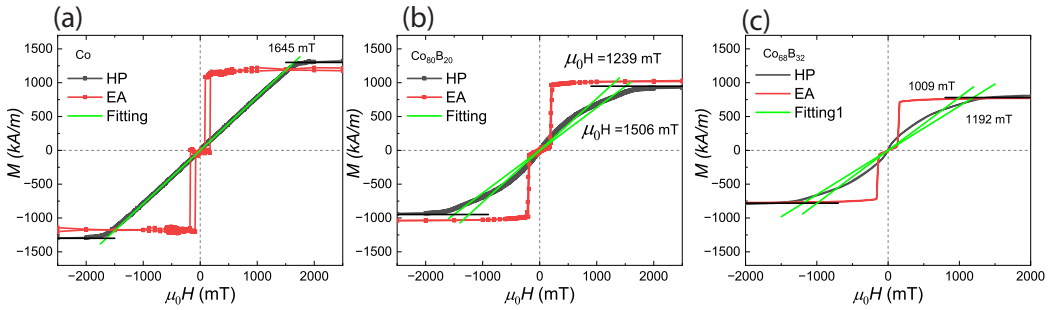

Figure C.4: Hard-plane (HP) and easy-axis (EA) loop of (a).Co, (b).$Co_{80}B_{20}$, and (c). $Co_{68}B_{32}$ measured through VSM-SQUID.

C.5 Normalized anisotropy

The normalized coercivity, defined as $\mu_0 H_c/K$, is plotted as a function of B concentration in Fig. C.5. Here we use the middle value of the K range obtained in Fig. C.4 to normalize. The normalized coercivity drops from approximately 3.5×10^{-7} m/A for pure Co to $1.7 - 3.2 \times 10^{-7}$ m/A for 20% B content, and further decreases to 0.5×10^{-7} m/A for 32% B content.

C.6 Kerr microscopy images during the switching process

Three thin-film samples, Ta(4)/Pt(2)/$Co_{1-x}B_x$(0.8)/Pt(2)/Ta(4) with thickness in nanometer, with varying boron concentrations (x=0, 20, and 32) were prepared and measured under Kerr microscopy to investigate the formation of nucleation centers during the switching process. A typical hysteresis loop of the thin film stack is illustrated in Fig. C.6. In each measurement, the sample was initially saturated at - 25 mT for 100 ms, as indicated by the green spot in Fig. C.6a. Here the minus field denotes the direction of the applied field pointing into the plane. Subsequently, a pulsed field of 5 ms at a specific positive field was applied to switch the sample, denoted by the blue spot in Fig. C.6a.

The hysteresis loop of the three $Co_{1-x}B_x$ based thin film samples is shown in

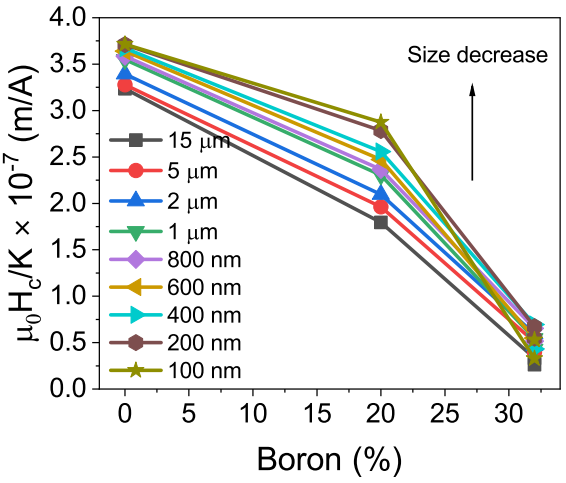

Figure C.5: Coercivity normalized by effective anisotropy ($\frac{\mu_0 H_c}{K}$) as a function of boron percentage.

Fig. C.6b. The Kerr microscopy images captured at different pulsed fields for the various $Co_{1-x}B_x$ compositions are presented in Fig. C.6(c-e). Across all samples, we found a round-shaped, small-volume region switched first at a lower field, which we refer to as nucleation centers. As the pulsed field increased, more nucleation centers appeared. Simultaneously we observed that the switched domain expanded. This behavior aligns with the switching mechanics which starts with domain nucleation and is followed by propagation of the domain wall[102].

Comparing between samples, we noted that Co-based samples exhibited a higher number of nucleation centers compared to $Co_{80}B_{20}$ and $Co_{68}B_{32}$. Moreover, the expansion of the nucleation centers in Co sample is slower compared to $Co_{80}B_{20}$ and $Co_{68}B_{32}$ samples. These nucleation centers are associated with grain boundaries arising from the polycrystalline structure. Introducing boron into Co resulted in a reduction in the number of nucleation centers and a decrease in domain-wall depinning due to the amorphous structure with fewer grain boundaries[178]. Upon further increasing the boron content, the number of nucleation centers increased again, which we attribute to the introduction of more homogenous defects into the material. Here, we speculate that the variation of K as captured by sigma as shown in Table 6.1 of the main text is much lower in the Boron containing samples as compared to Co, hence a more homogenous (in field) nucleation occurs (see also

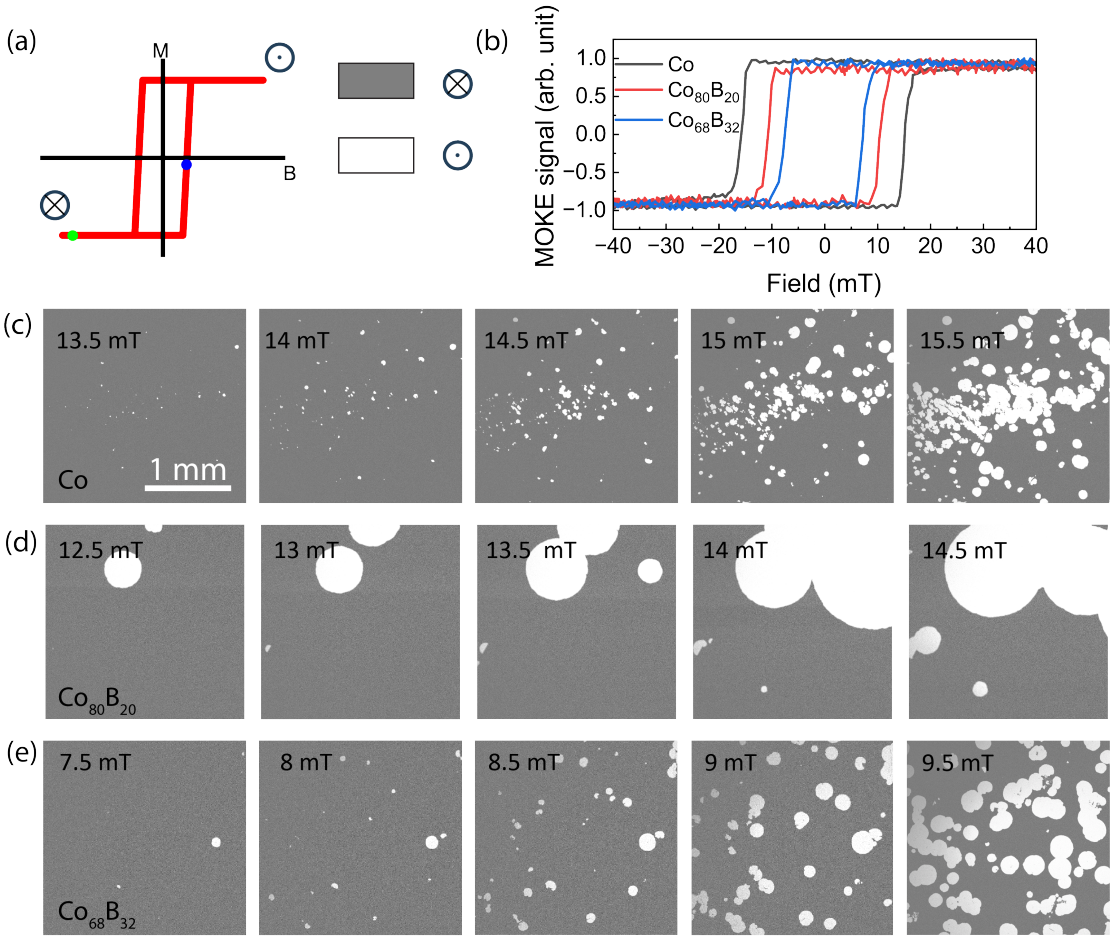

Figure C.6: (a) A typical hysteresis loop of $Co_{1-x}B_x$/Pt/Ta thin film stack. In each measurement, the sample was first saturated at -25 mT (marked as the green spot). Then a pulsed field (marked as the blue spot) of 5 ms was applied. (b) Hysteresis loop of the thin film sample based on different $Co_{1-x}B_x$ measured by MOKE. Kerr microscopy images of (c) Co, (d) $Co_{80}B_{20}$, and (e) $Co_{68}B_{32}$ sample at different pulsed fields. The grey area corresponds to the magnetization pointing into the plane. In the white region, the magnetization points out from the plane

section s6) as also reflected in the much lower coercivity of B containing samples compared to pure Co.

C.7 Fitting of the Co-based SAF sample

The $\mu_0 H_c$ and SFD of the Co-based SAF sample and the fitted curve are shown in Fig. C.7. The obtained σ is $0.06K$ and the d_{nu} is 1 nm. A noticeable discrepancy

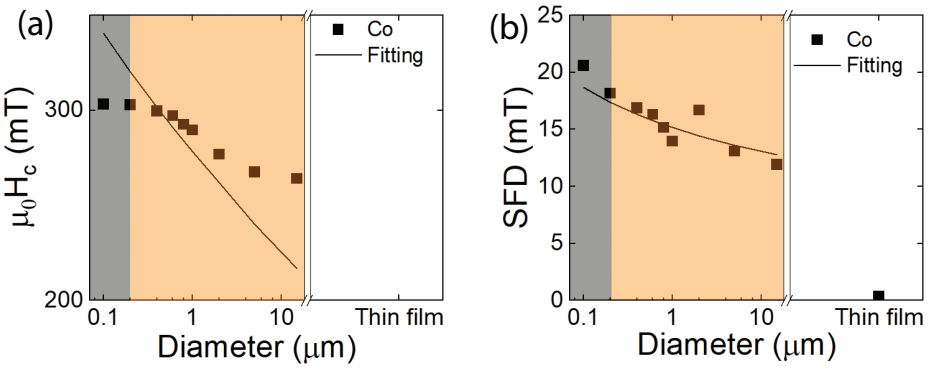

Figure C.7: The (a) $\mu_0 H_c$ and (b) SFD of Co based SAF sample as a function of diameter

exists between the fitted and measured $\mu_0 H_c$, which we attribute to the microstructure of the Co thin film that contains increased pinning sites, requiring a higher field for depinning. Our model assumes that once a nucleation center switches, the entire sample switches; however, in the Co sample, this condition may not be met due to the limited propagation of domain walls. One possible reason is the higher sputtering pressure used (10^{-2} mbar or 7.5 mTorr in our study) compared to 1-3 mTorr in other studies[88,160] . It has been reported that sputtering pressure influences the grain structure, consequently affecting magnetic properties[165–167] . In the Co/Pt system, domain walls move freely during reversal under lower growth pressures (below 3 mTorr). However, at higher pressures, an increase in defects that hinder domain wall propagation is observed[165,167] . Our sputtering pressure, which is close to the critical transition point for the reversal mechanism of 8-10 mTorr[165], is likely to impact the reversal mechanism. Furthermore, reference has been made to the higher number of pinning sites in Co/Pt compared to the CoB/Pt system, leading to slower domain wall motion[178]. These factors lead us to suspect that in our Co/Pt system, a higher field is required to propagate the domain wall and a different reversal mechanism is applied.

C.8 Major loop

The major and minor hysteresis loops of $Co_{80}B_{20}$ at various sizes are shown in Fig. C.8a, and the corresponding switching fields (H2 from the major loop, H1

and H3 from the minor loop) as functions of diameter are illustrated in Fig. C.8b. Differences in the opening of the major and minor loops are observed across all samples, indicating that the top and bottom layers differ. H1 and H3 represent the switching of the top layer, and H2 corresponds to the switching of the bottom layer. It is expected that the coercivity increases with decreasing size for both layers. Consequently, with the reduction in island size, an increasing H1 and decreasing H2 and H3 are expected. This trend is exactly what is observed in Fig. C.8b.

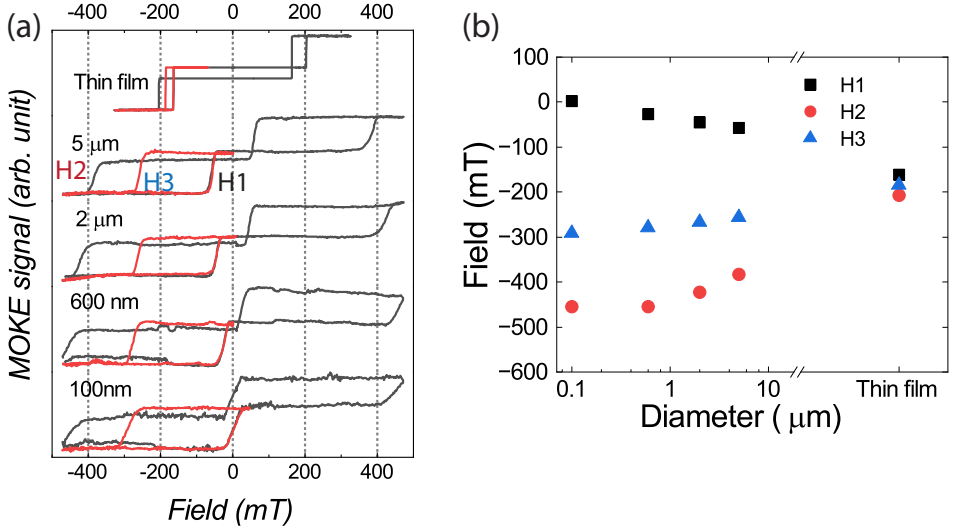

Figure C.8: (a) Major (in black) and minor (in red) hysteresis loops of $Co_{80}B_{20}$ based thin film SAF stack and SAF islands with different diameters. (b) The switching field H1, H2 and H3 in (a) as functions of diameter

Regarding the asymmetry between the top and bottom layers, H3 and H2 can be used to reflect the degree of asymmetry. As the size decreases, H3 decreases more rapidly than H2, resulting in a greater disparity between H3 and H2 and, thus, an increase in asymmetry.

C.9 Simulations with different K

Figure. C.9 shows simulations of coercivity and SFD as a function of diameter using different K obtained in Fig. C.4. The simulated $\frac{\sigma_K}{K}$ and d_{nu} are shown in

Table C.1: Simulation results of $Co_{1-x}B_x$ with different K

Materials	K (J/m^3)	$\frac{\sigma_K}{K}(\%)$	$d_{nu}(nm)$
$Co_{80}B_{20}$	4.4×10^5	2.9	288
$Co_{80}B_{20}$	5.8×10^5	3.5	58
$Co_{68}B_{32}$	2.8×10^5	3.0	41
$Co_{68}B_{32}$	3.5×10^5	2.2	16

Table. C.1.

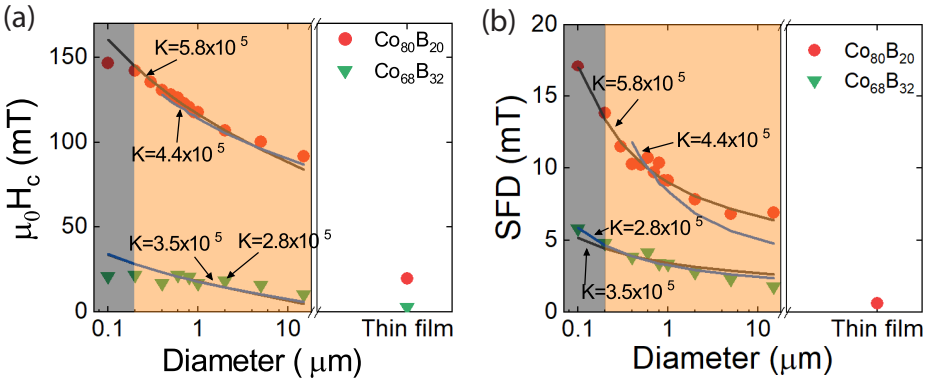

Figure C.9: Simulation results of (a) coercivity ($\mu_0 H_c$) and (b) SFD as a function of diameter. Different anisotropy (K) are used.

D

Supplemental information for chapter VI

D.1 Halbach array

The magnetic field inside the Halbach array is shown in the Fig. D.1.

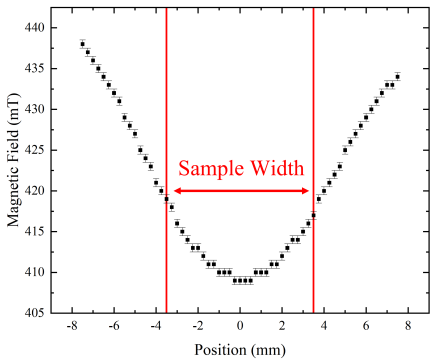

Figure D.1: The magnetic filed profile of Halbach array.

D.2 Video of rotating chains

In Fig. D.2, a QR code is provided for accessing videos that show the rotation of p-SAF NP chains at different frequencies (0.1 Hz, 1 Hz, and 5 Hz) in a 75% glycerin mixture.

Figure D.2: Scan this QR code to access detailed videos demonstrating the behavior of p-SAF NP chains at various frequencies in a 75% glycerin mixture.

D.3 Measurement of chain length

The way to get the chain length at each frame is shown in Fig. D.3. The original microscopy image is first transferred to a binary image. Then the chains are recognized based on the binary image. The average chain length is calculated based on all chains in a frame. The angle of the chain is relative to the horizontal plane.

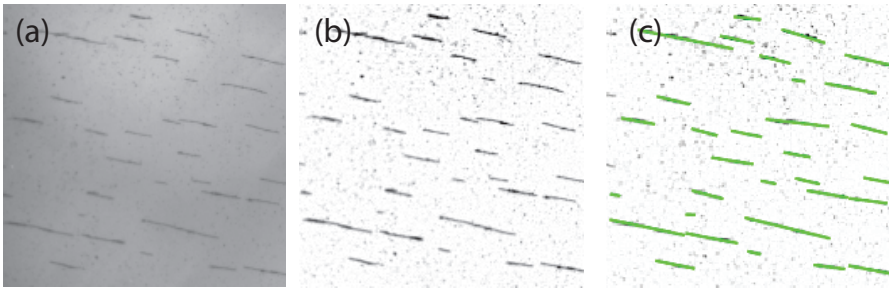

Figure D.3: (a) Original optical image of SAF NPs in 75% glycerin mixture. (b) Binary image of the original image. (c) Recognized chains are marked in green.

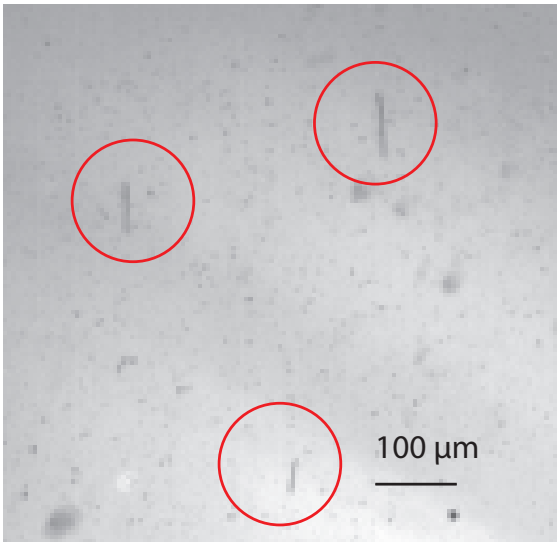

Figure D.4: Microscopy images of SAF NP chains in a 75% glycerin mixture under various 15 Hz. The chains still keep a line structure.

Summary

Towards Nanoscale Torque Revolution - Highly anisotropic synthetic antiferromagnetic nanoplatelets for torque-related application

The work described in this thesis covers the fabrication, characterization and application of so-called synthetic antiferromagnetic (SAF) based nanoplatelets (NPs) with perpendicular magnetic anisotropy (PMA). Magnetic nanoparticles have gained significant prominence owing to their ability to remotely manipulate their surrounding environment using a remote magnetic field or gradient thereof. They are used in many fields such as drug delivery, medical treatment, and diagnostics. While superparamagnetic iron oxide-based nanoparticles have been widely investigated, these nanoparticles face limitations, such as restricted magnetization and non-uniform magnetic properties. Additionally, their low magnetocrystalline and shape anisotropy hampers their torque transformation capabilities. To address these issues, we study the recently introduced PMA-SAF NPs.

These PMA-SAF NPs have a disc shape and contain a multilayer thin film structure as widely studied in the field of spintronics. This allows the introduction of a strong easy-axis/hard-plane PMA, making the NPs promising for applications requiring efficient torque transfer for magneto-mechanical force and torque actions: e.g. for micro-mixing, and cancer cell destruction. Although promising, it is a brand-new area with many challenges related to top-down fabrication, fundamental physical understanding of downscaling / particle-particle interactions, and characterization. In this thesis, we shed new light on these tasks.

In the first chapter, we developed a new top-down fabrication protocol based on substrate conformal imprint lithography (SCIL), together with a local company

SCIL Nanoimprint Solutions. We successfully fabricated PMA-SAF nanoplatelets with a diameter in the micrometre (1.8 um) and sub-micrometre (120 nm) range with a narrow size distribution, while preserving their high PMA. The results pave the way for using SCIL imprint for the large-scale production of PMA-SAF nanoplatelets using a subtractive method.

In the second chapter, a novel experimental technique is employed to examine the magnetization switching of individual SAF nanoplatelets with a diameter of 120 nm. Using photothermal magnetic circular dichroism (PT MCD) in collaboration with the NanoOptics group from Leiden University, we were able to measure the spatial and temporal heterogeneity of the magnetic properties, especially the switching fields at the single-particle level. The switching field distribution (SFD) is extracted from ensembles and individual NPs; comparing these confirms that the reversal process is a thermally activated stochastic process.

On downscaling, and with the insight that the thermal activation reversal remains the dominant reversal mechanism, the coercivity of the SAF NPs increases dramatically, which at first might seem counter-intuitive. This increase of coercivity requires a high magnetic field to activate the NPs, limiting their application. In the third chapter, we investigate a route to reduce the coercivity of PMA-SAF NPs. Our findings show that alloying Cobalt with Boron forming Co_xB_{1-x} can effectively reduce both coercivity and its SFD. This reduction is attributed to a decreased anisotropy and increased defect density in the ferromagnetic material.

In the final chapter, the study explores the potential of PMA-SAF NPs in a standard application, microscale mixing of a fluid, by investigating the dynamic mechanical properties under rotating magnetic fields. We found that under a rotating magnetic field, the PMA-SAF NPs form rigid chains that exhibit synchronized motion with the external field and do not deform. Increasing the frequency of the rotating field reduces the chain length, but the chains remain longer and more stable than those formed by e.g. iron oxide-based nanoparticles. This confirms the added value of the efficient mechanical response originating from the easy-axis/hard-plane symmetry of the magnetic anisotropy combined with the nanoplatelet shape.

The results in this thesis add to the fundamental understanding of PMA-SAF

NPs. This includes advancements in fabrication techniques, novel characterization techniques, precise tuning of PMA-SAF NPs' magnetic properties, and insights into their behavior in a torque-exploiting application.

Curriculum Vitae

Jianing Li was born on December 16, 1994 in Wuxi China. After finishing high school in 2012 at Jiangsu Xishan Senior High School, she studied Materials Science and Engineering at Zhejiang University. In 2016, she obtained her bachelor's degree in Engineering.

Jianing continued her studies at École polytechnique fédérale de Lausanne and obtained her master's degree in Materials Science and Engineering in 2019. During this time, she carried out an internship at the Biointerfaces lab, EMPA, working on antimicrobial surfaces. Her graduation project was focused on new dielectric materials for gate and passivation of GaN devices under the supervision of prof. Elison Matioli.

After obtaining her master's degree, Jianing continued with a PhD project on synthetic antiferromagnetic nanoplatelets in the group Physics of Nanostructure under the supervision of prof. Reinoud Lavrijsen and prof. Bert Koopmans. The main results of this project are presented in this thesis.

Publications

1. **Li, J.**, Van Nieuwkerk, P., Verschuuren, M.A., Koopmans, B. and Lavrijsen, R., *Substrate conformal imprint fabrication process of synthetic antiferromagnetic nanoplatelets.* Applied Physics Letters, 121(18) (2022).

2. Adhikari, S., **Li, J.**, Wang, Y., Ruijs, L., Liu, J., Koopmans, B., Orrit, M. and Lavrijsen, R., *Optical Monitoring of the Magnetization Switching of Single Synthetic-Antiferromagnetic Nanoplatelets with Perpendicular Magnetic Anisotropy.* ACS photonics, 10(5), pp.1512-1518 (2023).

3. **Li, J.**, Sijtsma, W., Koopmans, B. and Lavrijsen, R., *Tuning the coercivity of synthetic antiferromagnetic nanoplatelets with perpendicular anisotropy by varying the Co1−xBx alloy composition.* Journal of Applied Physics (2024).

4. **Li, J.**, Edelmann, L., Koopmans, B. and Lavrijsen, R., *Dynamics of Synthetic Antiferromagnetic Nanoplatelet Chains in a Rotating Magnetic Field* (2024). (In preparation)

5. Venkataramanachar, B.B., **Li, J.**, Islam, T.U., Wang, Y. and den Toonder, J.M., *Nanomagnetic Elastomers for Realizing Highly Responsive Micro-and Nanosystems.* Nano Letters, 23(20), pp.9203-9211 (2023).

Acknowledgements

Completing this PhD journey has been an meaningful and rewarding experience. I could not have reached this milestone without the support of many individuals who have been instrumental in my academic and personal growth. I extend my deepest gratitude to each one of them.

My heartfelt thanks go to my husband, Feng Lu. Your support in every aspect of my life, especially during those challenging moments filled with self-doubt, has been the foundation of my success. Your love, patience, and encouragement have been my greatest source of strength.

To my beloved family, especially my parents Weili and Juanjuan, thank you for your endless support. Despite the challenges posed by the COVID-19 pandemic and being unable to meet for almost three years, our weekly video calls made us close to each other. Your faith in me has always been my guiding light.

I am profoundly grateful to my supervisors. To Reinoud, my first promotor, I appreciate all the discussions, advice, and guidance throughout my PhD journey. Your concern for my well-being and your unwavering positivity have been a constant source of motivation. To Bert, my second promotor, our enlightening discussions on physics have been invaluable, offering new insights and clarity in my research.

A special acknowledgment to Mariia, my postdoc colleague. Your arrival marked a turning point in our nanoplatelets team, transforming my solitary journey into a collaborative and rewarding experience.

I extend my thanks to all the members of the Nanoplatelets team, particularly my students. To Paul, for our successful collaboration in creating 120 nm NPs; to Lieke, for turning our productive Friday afternoons into a published paper; to

Lotte, for advancing the AFM project; and to Laurenz, Carolus, Ruiz, Wieneke, and Sara, for your contributions to the SAF NPs project.

My gratitude also goes to those outside our lab who have been instrumental in my research. To Peter, for your invaluable assistance with experimental setups and discussions; to Marc from SCIL, for providing innovative solutions for imprinting; and to Michel, Subhasis, and Yonghui, for your collaboration on PT MCD.

I cannot express enough thanks for the support from our group. To Diana, for the insightful discussions; to Jeroen, our technician, whose swift action and dedication have been vital in keeping our lab functional; to Bart, for maintaining our lab equipment; and to Karin, our secretary, for managing our group with remarkable efficiency and even assisting with wedding venue arrangements. To Henk and Rembert, your support has been indispensable.

To my colleagues - Pingzhi, Luding, Zilu, Shen, Tianyu, and others - thank you for celebrating almost every Chinese festival with me and making me feel at home. To Adrien, Thomas, Julian, Lorenzo, Mark, Floris, Mark, Max, Gijs, Marielle, Youri, Casper, Tunç, Ece, Hamed, Tom, Juriaan, and Fanny, your assistance, discussions, and the cherished coffee time chats have greatly enriched my PhD experience.

This journey would not have been the same without each and every one of you. Your collective contributions have profoundly shaped my research and personal growth. For this, I am eternally grateful.

Bibliography

[1] M. W. Freeman, A. Arrott, and J. H. Watson, Magnetism in medicine, Journal of Applied Physics **31**, S404 (1960).

[2] N. F. Ramsey, Early History of Magnetic Resonance, Physics in Perspective **1**, 123 (1999).

[3] N. Tesla, Massage with currents of high frequency, Electrical Engineers **12**, 679 (1891).

[4] A. Pyatakov, Z. Pyatakova, and A. M. Tishin, Short history overview of magnetism and magnetic technologies for medical applications, Magnetic Materials and Technologies for Medical Applications , 3 (2022).

[5] P. C. Lauterbur, Image Formation by Induced Local Interactions: Examples Employing Nuclear Magnetic Resonance, Nature 1973 242:5394 **242**, 190 (1973).

[6] D. D. Stueber, J. Villanova, I. Aponte, Z. Xiao, and V. L. Colvin, Magnetic Nanoparticles in Biology and Medicine: Past, Present, and Future Trends, Pharmaceutics **13** (2021).

[7] A. Akbarzadeh, M. Samiei, and S. Davaran, Magnetic nanoparticles: Preparation, physical properties, and applications in biomedicine, Nanoscale Research Letters **7**, 1 (2012).

[8] K. N. Koo, A. F. Ismail, M. H. D. Othman, M. A. Rahman, and T. Z. Sheng, Preparation and characterization of superparamagnetic magnetite (Fe3O4) nanoparticles: A short review, Malaysian Journal of Fundamental and Applied Sciences **15**, 23 (2019).

[9] M. A. Malik, M. Y. Wani, and M. A. Hashim, Microemulsion method: A novel route to synthesize organic and inorganic nanomaterials: 1st Nano Update, Arabian Journal of Chemistry **5**, 397 (2012).

[10] A. H. Lu, E. L. Salabas, and F. Schüth, Magnetic nanoparticles: Synthesis, protection, functionalization, and application (2007).

[11] T. Kobayashi, Cancer hyperthermia using magnetic nanoparticles, Biotechnology Journal **6**, 1342 (2011).

[12] B. Jeyadevan, Present status and prospects of magnetite nanoparticles-based hyperthermia, Journal of the Ceramic Society of Japan **118**, 391 (2010).

[13] F. Gazeau, M. Lévy, and C. Wilhelm, Optimizing magnetic nanoparticle design for nanothermotherapy (2008).

[14] R. Hergt and S. Dutz, Magnetic particle hyperthermia—biophysical limitations of a visionary tumour therapy, Journal of Magnetism and Magnetic Materials **311**, 187 (2007).

[15] R. Hergt, S. Dutz, R. Müller, and M. Zeisberger, Magnetic particle hyperthermia: nanoparticle magnetism and materials development for cancer therapy, Journal of Physics: Condensed Matter **18**, S2919 (2006).

[16] E. Rimstad, E. Hornes, O. Olsvik, and B. Hyllseth, Identification of a double-stranded RNA virus by using polymerase chain reaction and magnetic separation of the synthesized DNA segments, Journal of Clinical Microbiology **28**, 2275 (1990).

[17] D. J. Wright, P. A. Chapman, and C. A. Siddons, Immunomagnetic separation as a sensitive method for isolating Escherichia coli O157 from food samples, Epidemiology & Infection **113**, 31 (1994).

[18] W. Liang, J. Liu, X. Yang, Q. Zhang, W. Yang, H. Zhang, and L. Liu, Microfluidic-based cancer cell separation using active and passive mechanisms, Microfluidics and Nanofluidics 2020 24:4 **24**, 1 (2020).

[19] C. Wyatt Shields Iv, C. D. Reyes, and G. P. López, Microfluidic cell sorting: a review of the advances in the separation of cells from debulking to rare cell isolation, Lab on a Chip **15**, 1230 (2015).

[20] C. Chircov, A. M. Grumezescu, and A. M. Holban, Magnetic Particles for Advanced Molecular Diagnosis, Materials **12**, 10.3390/MA12132158 (2019).

[21] K. T. Al-Jamal, J. Bai, J. T. W. Wang, A. Protti, P. Southern, L. Bogart, H. Heidari, X. Li, A. Cakebread, D. Asker, W. T. Al-Jamal, A. Shah, S. Bals, J. Sosabowski, and Q. A. Pankhurst, Magnetic Drug Targeting: Preclinical in Vivo Studies, Mathematical Modeling, and Extrapolation to Humans, Nano Letters **16**, 5652 (2016).

[22] J. F. Liu, Z. Lan, C. Ferrari, J. M. Stein, E. Higbee-Dempsey, L. Yan, A. Amirshaghaghi, Z. Cheng, D. Issadore, and A. Tsourkas, Use of Oppositely Polarized External Magnets to Improve the Accumulation and Penetration of Magnetic Nanocarriers into Solid Tumors, ACS Nano **14**, 142 (2020).

[23] R. Mansell, T. Vemulkar, D. C. Petit, Y. Cheng, J. Murphy, M. S. Lesniak, and R. P. Cowburn, Magnetic particles with perpendicular anisotropy for mechanical cancer cell destruction, Scientific Reports **7**, 10.1038/s41598-017-04154-1 (2017).

[24] M. Goiriena-Goikoetxea, D. Muñoz, I. Orue, M. L. Fernández-Gubieda, J. Bokor, A. Muela, and A. García-Arribas, Disk-shaped magnetic particles for cancer therapy, Applied Physics Reviews **7**, 10.1063/1.5123716 (2020).

[25] K. Han, C. Wyatt, O. D. Velev, K. Han, C. W. Shields, and I. O. D. Velev, Engineering of Self-Propelling Microbots and Microdevices Powered by Magnetic and Electric Fields, Advanced Functional Materials **28**, 1705953 (2018).

[26] D. Schamel, A. G. Mark, J. G. Gibbs, C. Miksch, K. I. Morozov, A. M. Leshansky, and P. Fischer, Nanopropellers and their actuation in complex viscoelastic media, ACS Nano **8**, 8794 (2014).

[27] R. Dreyfus, J. Baudry, M. L. Roper, M. Fermigier, H. A. Stone, and J. Bibette, Microscopic artificial swimmers, Nature 2005 437:7060 **437**, 862 (2005).

[28] L. Zhang, J. J. Abbott, L. Dong, K. E. Peyer, B. E. Kratochvil, H. Zhang, C. Bergeles, and B. J. Nelson, Characterizing the swimming properties of artificial bacterial flagella, Nano Letters **9**, 3663 (2009).

[29] W. Gao, S. Sattayasamitsathit, K. M. Manesh, D. Weihs, and J. Wang, Magnetically powered flexible metal nanowire motors, Journal of the American Chemical Society **132**, 14403 (2010).

[30] L. Zhang, T. Petit, Y. Lu, B. E. Kratochvil, K. E. Peyer, R. Pei, J. Lou, and B. J. Nelson, Controlled propulsion and cargo transport of rotating nickel nanowires near a patterned solid surface, ACS Nano **4**, 6228 (2010).

[31] W. Huang, F. Yang, L. Zhu, R. Qiao, and Y. Zhao, Manipulation of magnetic nanorod clusters in liquid by non-uniform alternating magnetic fields, Soft Matter **13**, 3750 (2017).

[32] H. Shen, S. Tong, G. Bao, and B. Wang, Structural responses of cells to intracellular magnetic force induced by superparamagnetic iron oxide nanoparticles, Physical Chemistry Chemical Physics **16**, 1914 (2014).

[33] D. Cheng, X. Li, G. Zhang, and H. Shi, Morphological effect of oscillating magnetic nanoparticles in killing tumor cells, Nanoscale Research Letters **9**, 1 (2014).

[34] S. B. Smith, L. Finzi, and C. Bustamante, Direct Mechanical Measurements of the Elasticity of Single DNA Molecules by Using Magnetic Beads, Science **258**, 1122 (1992).

[35] I. De Vlaminck and C. Dekker, Recent advances in magnetic tweezers, Annual Review of Biophysics **41**, 453 (2012).

[36] P. A. Valberg and H. A. Feldman, Magnetic particle motions within living cells. Measurement of cytoplasmic viscosity and motile activity, Biophysical Journal **52**, 551 (1987).

[37] C. P. Moerland, L. J. Van IJzendoorn, and M. W. Prins, Rotating magnetic particles for lab-on-chip applications – a comprehensive review, Lab on a Chip **19**, 919 (2019).

[38] X. Chen and L. Zhang, A review on micromixers actuated with magnetic nanomaterials, Microchimica Acta 2017 184:10 **184**, 3639 (2017).

[39] A. P. Astalan, F. Ahrentorp, C. Johansson, K. Larsson, and A. Krozer, Biomolecular reactions studied using changes in Brownian rotation dynamics of magnetic particles, Biosensors and Bioelectronics **19**, 945 (2004).

[40] A. Fornara, P. Johansson, K. Petersson, S. Gustafsson, Q. Jian, E. Olsson, D. Iiver, A. Krozer, M. Muhammed, and C. Johansson, Tailored magnetic nanoparticles for direct and sensitive detection of biomolecules in biological samples, Nano Letters **8**, 3423 (2008).

[41] J. Dieckhoff, A. Lak, M. Schilling, and F. Ludwig, Protein detection with magnetic nanoparticles in a rotating magnetic field, Journal of Applied Physics **115** (2014).

[42] J. M. Coey, *Magnetism and Magnetic Materials*, Vol. 9780521816 (Cambridge university press, 2010) pp. 1–617.

[43] Z. Ma, J. Mohapatra, K. Wei, J. P. Liu, and S. Sun, Magnetic Nanoparticles: Synthesis, Anisotropy, and Applications, Chemical Reviews **123**, 3904 (2023).

[44] Y. W. Jun, J. S. Choi, and J. Cheon, Shape Control of Semiconductor and Metal Oxide Nanocrystals through Nonhydrolytic Colloidal Routes, Angewandte Chemie International Edition **45**, 3414 (2006).

[45] K. Gandha, J. Mohapatra, M. K. Hossain, K. Elkins, N. Poudyal, K. Rajeshwar, and J. P. Liu, Mesoporous iron oxide nanowires: synthesis, magnetic and photocatalytic properties, RSC Advances **6**, 90537 (2016).

[46] Y. Hou, H. Kondoh, R. Che, M. Takeguchi, and T. Ohta, Ferromagnetic FePt Nanowires: Solvothermal Reduction Synthesis and Characterization, Small **2**, 235 (2006).

[47] H. Niu, Q. Chen, M. Ning, Y. Jia, and X. Wang, Synthesis and One-Dimensional Self-Assembly of Acicular Nickel Nanocrystallites under Magnetic Fields, Journal of Physical Chemistry B **108**, 3996 (2004).

[48] M. Chen, T. Pica, Y. B. Jiang, P. Li, K. Yano, J. P. Liu, A. K. Datye, and H. Fan, Synthesis and self-assembly of fcc phase FePt nanorods, Journal of the American Chemical Society **129**, 6348 (2007).

[49] N. Cordente, M. Respaud, F. Senocq, M. J. Casanove, C. Amiens, and B. Chaudret, Synthesis and Magnetic Properties of Nickel Nanorods, Nano Letters **1**, 565 (2001).

[50] V. F. Puntes, D. Zanchet, C. K. Erdonmez, and A. P. Alivisatos, Synthesis of hcp-Co nanodisks, Journal of the American Chemical Society **124**, 12874 (2002).

[51] J. Zhu and Z. Nan, Zn-Doped Fe3O4 Nanosheet Formation Induced by EDA with High Magnetization and an Investigation of the Formation Mechanism, Journal of Physical Chemistry C **121**, 9612 (2017).

[52] C. Schopphoven and A. Tschöpe, Magnetic anisotropy of nickel nanorods and the mechanical torque in an elastic environment, Journal of Physics D: Applied Physics **51**, 115005 (2018).

[53] D. W. Wong, W. L. Gan, N. Liu, and W. S. Lew, Magneto-actuated cell apoptosis by biaxial pulsed magnetic field, Scientific Reports 2017 7:1 **7**, 1 (2017).

[54] M. F. Contreras, R. Sougrat, A. Zaher, T. Ravasi, and J. Kosel, Non-chemotoxic induction of cancer cell death using magnetic nanowires, International Journal of Nanomedicine **10**, 2141 (2015).

[55] A. I. Martínez-Banderas, A. Aires, F. J. Teran, J. E. Perez, J. F. Cadenas, N. Alsharif, T. Ravasi, A. L. Cortajarena, and J. Kosel, Functionalized magnetic nanowires for chemical and magneto-mechanical induction of cancer cell death, Scientific Reports 2016 6:1 **6**, 1 (2016).

[56] M. J. Madou, *Fundamentals of Microfabrication and Nanotechnology, Three-Volume Set* (2018) pp. 1–23.

[57] S. Leulmi, H. Joisten, T. Dietsch, C. Iss, M. Morcrette, S. Auffret, P. Sabon, and B. Dieny, Comparison of dispersion and actuation properties of vortex and synthetic antiferromagnetic particles for biotechnological applications, Applied Physics Letters **103**, 10.1063/1.4821854 (2013).

[58] D. H. Kim, E. A. Rozhkova, I. V. Ulasov, S. D. Bader, T. Rajh, M. S. Lesniak, and V. Novosad, Biofunctionalized magnetic-vortex microdiscs for targeted cancer-cell destruction, Nature Materials **9**, 165 (2010).

[59] W. Hu, R. J. Wilson, C. M. Earhart, A. L. Koh, R. Sinclair, and S. X. Wang, Synthetic antiferromagnetic nanoparticles with tunable susceptibilities, Journal of Applied Physics **105**, 07B508 (2009).

[60] A. L. Koh, W. Hu, R. J. Wilson, S. X. Wang, and R. Sinclair, Preparation, structural and magnetic characterization of synthetic anti-ferromagnetic (SAF) nanoparticles, Philosophical Magazine **88**, 4225 (2008).

[61] B. Mora, A. Perez-Valle, C. Redondo, M. D. Boyano, and R. Morales, Cost-Effective Design of High-Magnetic Moment Nanostructures for Biotechnological Applications, ACS Applied Materials and Interfaces **10**, 8165 (2018).

[62] T. Vemulkar, R. Mansell, D. C. Petit, R. P. Cowburn, and M. S. Lesniak, Highly tunable perpendicularly magnetized synthetic antiferromagnets for biotechnology applications, Applied Physics Letters **107**, 10.1063/1.4926336 (2015).

[63] G. Varvaro, S. Laureti, D. Peddis, M. Hassan, G. Barucca, P. Mengucci, A. Gerardino, E. Giovine, O. Lik, D. Nissen, and M. Albrecht, Co/Pd-Based synthetic antiferromagnetic thin films on Au/resist underlayers: Towards biomedical applications, Nanoscale **11**, 21891 (2019).

[64] E. N. Welbourne, T. Vemulkar, and R. P. Cowburn, High-yield fabrication of perpendicularly magnetised synthetic antiferromagnetic nanodiscs, Nano Research , 1 (2021).

[65] Y. Cheng, M. E. Muroski, D. C. Petit, R. Mansell, T. Vemulkar, R. A. Morshed, Y. Han, I. V. Balyasnikova, C. M. Horbinski, X. Huang, L. Zhang, R. P. Cowburn, and M. S. Lesniak, Rotating magnetic field induced oscillation of magnetic particles for in vivo mechanical destruction of malignant glioma, Journal of Controlled Release **223**, 75 (2016).

[66] M. Morcrette, G. Ortiz, S. Tallegas, H. Joisten, R. Tiron, T. Baron, Y. Hou, S. Lequien, A. Bsiesy, and B. Dieny, Fabrication of monodisperse magnetic nanoparticles released in solution using a block copolymer template, Journal of Physics D: Applied Physics **50**, 10.1088/1361-6463/aa790b (2017).

[67] E. A. Rozhkova, V. Novosad, D. H. Kim, J. Pearson, R. Divan, T. Rajh, and S. D. Bader, Ferromagnetic microdisks as carriers for biomedical applications, Journal of Applied Physics **105**, 5 (2009).

[68] S. Yuasa and D. D. Djayaprawira, Giant tunnel magnetoresistance in magnetic tunnel junctions with a crystalline MgO(0 0 1) barrier, Journal of Physics D: Applied Physics **40**, R337 (2007).

[69] D. D. Djayaprawira, K. Tsunekawa, M. Nagai, H. Maehara, S. Yamagata, N. Watanabe, S. Yuasa, Y. Suzuki, and K. Ando, 230% room-temperature magnetoresistance in CoFeBMgOCoFeB magnetic tunnel junctions, Applied Physics Letters **86**, 1 (2005).

[70] S. Yuasa, T. Nagahama, A. Fukushima, Y. Suzuki, and K. Ando, Giant room-temperature magnetoresistance in single-crystal Fe/MgO/Fe magnetic tunnel junctions, Nature Materials 2004 3:12 **3**, 868 (2004).

[71] S. Bandiera, R. C. Sousa, B. Rodmacq, and B. Dieny, Enhancement of perpendicular magnetic anisotropy through reduction of Co-Pt interdiffusion in (Co/Pt) multilayers, Applied Physics Letters **100**, 23 (2012).

[72] O. Donzelli, . D. Palmeri, . L. Musa, . F. Casoli, . F. Albertini, . L. Pareti, . G. Turilli, D. Palmeri, L. Musa, F. Casoli, . F. Albertini, L. Pareti, and G. Turilli, Perpendicular magnetic anisotropy and stripe domains in ultrathin Co/Au sputtered multilayers, Journal of Applied Physics **93**, 9908 (2003).

[73] B. M. Lairson, J. Perez, and C. Baldwin, Application of Pd/Co multilayers for perpendicular magnetic recording, Applied Physics Letters **64**, 2891 (1994).

[74] P. F. Carcia, Perpendicular magnetic anisotropy in Pd/Co and Pt/Co thin-film layered structures, Journal of Applied Physics **63**, 5066 (1998).

[75] N. Nakajima, T. Koide, T. Shidara, H. Miyauchi, H. Fukutani, A. Fujimori, K. Iio, T. Katayama, M. Nývlt, and Y. Suzuki, Perpendicular Magnetic Anisotropy Caused by Interfacial Hybridization via Enhanced Orbital Moment in <span class, Physical Review Letters **81**, 5229 (1998).

[76] B. Tudu and A. Tiwari, Recent Developments in Perpendicular Magnetic Anisotropy Thin Films for Data Storage Applications, Vacuum **146**, 329 (2017).

[77] M. A. Ruderman and C. Kittel, Indirect Exchange Coupling of Nuclear Magnetic Moments by Conduction Electrons, Physical Review **96**, 99 (1954).

[78] T. Kasuya, A Theory of Metallic Ferro- and Antiferromagnetism on Zener's Model, Progress of Theoretical Physics **16**, 45 (1956).

[79] K. Yosida, Magnetic Properties of Cu-Mn Alloys, Physical Review **106**, 893 (1957).

[80] W. Peng, O. Keitel, R. H. Victora, E. Koparal, and J. H. Judy, Co/Pt superlattices with ultra-thin Ta seed layer on NiFe underlayer for double-layer perpendicular magnetic recording media, IEEE Transactions on Magnetics **36**, 2390 (2000).

[81] W. Hu, R. J. Wilson, A. Koh, A. Fu, A. Z. Faranesh, C. M. Earhart, S. J. Osterfeld, S. J. Han, L. Xu, S. Guccione, R. Sinclair, and S. X. Wang, High-moment antiferromagnetic nanoparticles with tunable magnetic properties, Advanced Materials **20**, 1479 (2008).

[82] A. Fu, W. Hu, L. Xu, R. J. Wilson, H. Yu, S. J. Osterfeld, S. S. Gambhir, and S. X. Wang, Protein-functionalized synthetic antiferromagnetic nanoparticles for biomolecule detection and magnetic manipulation, Angewandte Chemie - International Edition **48**, 1620 (2009).

[83] M. Zhang, X. Xie, M. Tang, C. S. Criddle, Y. Cui, and S. X. Wang, Magnetically ultraresponsive nanoscavengers for next-generation water purification systems, Nature Communications **4**, 1866 (2013).

[84] T. Vemulkar, R. Mansell, D. C. Petit, R. P. Cowburn, and M. S. Lesniak, The effect of underlayers on the reversal of perpendicularly magnetized multilayer thin films for magnetic micro- and nanoparticles, Journal of Applied Physics **121**, 10.1063/1.4974300 (2017).

[85] T. Vemulkar, E. N. Welbourne, R. Mansell, D. C. Petit, and R. P. Cowburn, The mechanical response in a fluid of synthetic antiferromagnetic and ferrimagnetic microdiscs with perpendicular magnetic anisotropy, Applied Physics Letters **110**, 10.1063/1.4974211 (2017).

[86] E. N. Welbourne, T. Vemulkar, D. C. M. C. Petit, and R. P. Cowburn, Weakly coupled synthetic antiferromagnetic nanodisks with perpendicular magnetic anisotropy for lab-on-chip devices, Applied Physics Letters **119**, 102401 (2021).

[87] U. Tamer, Y. Gündoğdu, I. H. Boyaci, and K. Pekmez, Synthesis of magnetic core-shell Fe3O4-Au nanoparticle for biomolecule immobilization and detection, Journal of Nanoparticle Research **12**, 1187 (2010).

[88] T. Thomson, G. Hu, and B. D. Terris, Intrinsic distribution of magnetic anisotropy in thin films probed by patterned nanostructures, Physical Review Letters **96**, 1 (2006).

[89] T. Uhlig and J. Zweck, Recording of single-particle hysteresis loops with differential phase contrast microscopy, Ultramicroscopy **99**, 137 (2004).

[90] E. Snoeck, C. Gatel, L. M. Lacroix, T. Blon, S. Lachaize, J. Carrey, M. Respaud, and B. Chaudret, Magnetic configurations of 30 nm iron nanocubes studied by electron holography, Nano Letters **8**, 4293 (2008).

[91] I. Petousis, E. Homburg, R. Derks, and A. Dietzel, Transient behaviour of magnetic micro-bead chains rotating in a fluid by external fields, Lab on a Chip **7**, 1746 (2007).

[92] S. Melle and J. E. Martin, Chain model of a magnetorheological suspension in a rotating field, The Journal of Chemical Physics **118**, 9875 (2003).

[93] J. Dieckhoff, D. Eberbeck, M. Schilling, and F. Ludwig, Magnetic-field dependence of Brownian and Néel relaxation times, Journal of Applied Physics **119**, 10.1063/1.4940724/142688 (2016).

[94] F. J. den Broeder, W. Hoving, and P. J. Bloemen, Magnetic anisotropy of multilayers, Journal of Magnetism and Magnetic Materials **93**, 562 (1991).

[95] K. Wang, M. C. Wu, S. Lepadatu, J. S. Claydon, C. H. Marrows, and S. J. Bending, Optimization of Co/Pt multilayers for applications of current-driven domain wall propagation, Journal of Applied Physics **110**, 83913 (2011).

[96] M. Kisielewski, A. Maziewski, M. Tekielak, J. Ferré, S. Lemerle, V. Mathet, and C. Chappert, Magnetic anisotropy and magnetization reversal processes in Pt/Co/Pt films, Journal of Magnetism and Magnetic Materials **260**, 231 (2003).

[97] R. Lavrijsen, A. Feránndez-Pacheco, D. Petit, R. Mansell, J. H. Lee, and R. P. Cowburn, Tuning the interlayer exchange coupling between single perpendicularly magnetized CoFeB layers, Applied Physics Letters **100**, 10.1063/1.3682103 (2012).

[98] M. L. M. Lalieu, *Femtomagnetism meets spintronics and magnonics*, Ph.D. thesis (2019).

[99] R. Ernst, Towards New Magnetic Nanoparticles, Master thesis (2018).

[100] Z. Jing, W. Yin-Jun, and H. Xiu-Feng, Dependence of Interlayer AF Coupling on Ferromagnetic Layer Thickness in [Pt/Co]5/Ru/[Co/Pt]5 Multilayers, **26**, 37302 (2009).

[101] B. Dieny, J. P. Gavigan, and J. P. Rebouillat, Magnetisation processes, hysteresis and finite-size effects in model multilayer systems of cubic or uniaxial anisotropy with antiferromagnetic coupling between adjacent ferromagnetic layers, Journal of Physics: Condensed Matter **2**, 159 (1990).

[102] G. Hu, T. Thomson, C. T. Rettner, S. Raoux, and B. D. Terris, Magnetization reversal in CoPd nanostructures and films, Journal of Applied Physics **97**, 1 (2005).

[103] G. Hu, T. Thomson, C. T. Rettner, and B. D. Terris, Rotation and wall propagation in multidomain Co/Pd islands, IEEE Transactions on Magnetics **41**, 3589 (2005).

[104] J. T. McKinney, Kinetic effects in coercivity measurements, IEEE Transactions on Magnetics **17**, 3020 (1981).

[105] J. M. Shaw, S. E. Russek, T. Thomson, M. J. Donahue, B. D. Terris, O. Hellwig, E. Dobisz, and M. L. Schneider, Reversal mechanisms in perpendicularly magnetized nanostructures, Physical Review B - Condensed Matter and Materials Physics **78**, 1 (2008).

[106] Marcus Antonius Verschuuren, *Substrate Conformal Imprint Lithography for Nanophotonics*, Ph.D. thesis (2010).

[107] M. M. Decré, R. Schneider, D. Burdinski, J. Schellekens, M. Saalmink, and R. Dona, Wave printing (I): Towards large-area, multilayer microcontact printing, Materials Research Society Symposium Proceedings **EXS**, 59 (2004).

[108] J. Schellekens, D. Burdinski, M. Saalmink, M. Beenhakkers, G. Gelinck, and M. M. Deeré, Wave printing (II): Polymer MISFETs using microcontact printing, Materials Research Society Symposium Proceedings **EXS**, 21 (2004).

[109] E. Delamarche, H. Schmid, B. Michel, and H. Biebuyck, Stability of molded polydimethylsiloxane microstructures, Advanced Materials **9**, 741 (1997).

[110] Y. Y. Huang, W. Zhou, K. J. Hsia, E. Menard, J. U. Park, J. A. Rogers, and A. G. Alleyne, Stamp collapse in soft lithography, Langmuir **21**, 8058 (2005).

[111] H. Schmid and B. Michel, Siloxane polymers for high-resolution, high-accuracy soft lithography, Macromolecules **33**, 3042 (2000).

[112] V. K. Parashar, A. Sayah, E. Cuche, C. Depeursinge, and M. A. M. Gijs, Diffractive optical elements in titanium oxide for MOEMS applications, in *TRANSDUCERS '03. 12th International Conference on Solid-State Sensors, Actuators and Microsystems. Digest of Technical Papers (Cat. No.03TH8664)*, Vol. 2 (2003) pp. 1482–1485 vol.2.

[113] C. Marzolin, S. P. Smith, M. Prentiss, and G. M. Whitesides, Fabrication of glass microstructures by micro-molding of sol-gel precursors, Advanced Materials **10**, 571 (1998).

[114] M. J. Madou, *Fundamentals of Microfabrication* (1997).

[115] M. E. Walsh, Y. Hao, C. A. Ross, and H. I. Smith, Optimization of a lithographic and ion beam etching process for nanostructuring magnetoresistive thin film stacks, Journal of Vacuum Science & Technology B: Microelectronics and Nanometer Structures Processing, Measurement, and Phenomena **18**, 3539 (2000).

[116] Y. S. Song, S. J. Park, T. W. Kim, and C. W. Cung, Influence of wet chemical cleaning on properties of magnetic tunnel junction stack for magnetic RAM, Electrochemical and Solid-State Letters **7**, 64 (2004).

[117] M. T. Moneck, J. G. Zhu, X. Che, Y. Tang, H. J. Lee, S. Zhang, K. S. Moon, and N. Takahashi, Fabrication of flyable perpendicular discrete track media, IEEE Transactions on Magnetics **43**, 2127 (2007).

[118] S. W. Chun, D. Kim, J. Kwon, B. Kim, S. Choi, and S. B. Lee, Multi-step ion beam etching of sub-30 nm magnetic tunnel junctions for reducing leakage and MgO barrier damage, Journal of Applied Physics **111**, 10 (2012).

[119] P. Ho, J. E. Johannes, R. J. Buss, and E. Meeks, Modeling the plasma chemistry of C2F6 and CHF3 etching of silicon dioxide, with comparisons to etch rate and diagnostic data, Journal of Vacuum Science & Technology A: Vacuum, Surfaces, and Films **19**, 2344 (2001).

[120] J. K. LL.D., XLIII. On rotation of the plane of polarization by reflection from the pole of a magnet, The London, Edinburgh, and Dublin Philosophical Magazine and Journal of Science **3**, 321 (1877).

[121] K. Uchiyama, A. Hibara, H. Kimura, T. Sawada, and T. Kitamori, Thermal lens microscope, Japanese Journal of Applied Physics, Part 1: Regular Papers and Short Notes and Review Papers **39**, 5316 (2000).

[122] S. Adhikari, P. Spaeth, A. Kar, M. D. Baaske, S. Khatua, and M. Orrit, Photothermal Microscopy: Imaging the Optical Absorption of Single Nanoparticles and Single Molecules, ACS Nano **14**, 16414 (2020).

[123] P. Spaeth, S. Adhikari, M. D. Baaske, S. Pud, J. Ton, and M. Orrit, Photothermal Circular Dichroism of Single Nanoparticles Rejecting Linear Dichroism by Dual Modulation, ACS Nano **15**, 16277 (2021).

[124] P. Spaeth, S. Adhikari, K. Lahabi, M. D. Baaske, Y. Wang, and M. Orrit, Imaging the Magnetization of Single Magnetite Nanoparticle Clusters via Photothermal Circular Dichroism, Nano Letters 10.1021/acs.nanolett.2c00178 (2022).

[125] S. Markus, *Photothermal Single Particle Detection in Theory & Experiments*, Ph.D. thesis (2013).

[126] R. L. Fagaly, Superconducting quantum interference device instruments and applications, Review of Scientific Instruments **77**, 101101 (2006).

[127] J. Li, P. Van Nieuwkerk, M. A. Verschuuren, B. Koopmans, and R. Lavrijsen, Substrate conformal imprint fabrication process of synthetic antiferromagnetic nanoplatelets, Applied Physics Letters **121**, 182407 (2022), arXiv:2206.15320 .

[128] Y. Gao, A. van Reenen, M. Hulsen, A. De Jong, M. Prins, and J. Den Toonder, Chaotic fluid mixing by alternating microparticle topologies to enhance biochemical reactions, Microfluidics and nanofluidics **16**, 265 (2014).

[129] H. Chiriac, E. Radu, M. Țibu, G. Stoian, G. Ababei, L. Lăbușcă, D. D. Herea, and N. Lupu, Fe-Cr-Nb-B ferromagnetic particles with shape anisotropy for cancer cell destruction by magneto-mechanical actuation, Scientific Reports **8**, 2 (2018).

[130] U. M. Engelmann, A. A. Roeth, D. Eberbeck, E. M. Buhl, U. P. Neumann, T. Schmitz-Rode, and I. Slabu, Combining bulk temperature and nanoheating enables advanced magnetic fluid hyperthermia efficacy on pancreatic tumor cells, Scientific reports **8**, 1 (2018).

[131] J. Dobson, Remote control of cellular behaviour with magnetic nanoparticles, Nature Nanotechnology 2008 3:3 **3**, 139 (2008).

[132] R. M. Erb, J. J. Martin, R. Soheilian, C. Pan, and J. R. Barber, Actuating Soft Matter with Magnetic Torque, Advanced Functional Materials **26**, 3859 (2016).

[133] E. A. Rozhkova, V. Novosad, D.-H. Kim, J. Pearson, R. Divan, T. Rajh, and S. D. Bader, Ferromagnetic microdisks as carriers for biomedical applications, Journal of Applied Physics **105**, 07B306 (2009).

[134] D.-H. Kim, E. A. Rozhkova, I. V. Ulasov, S. D. Bader, T. Rajh, M. S. Lesniak, and V. Novosad, Biofunctionalized magnetic-vortex microdiscs for targeted cancer-cell destruction, Nature Materials 2009 9:2 **9**, 165 (2009).

[135] A. I. Martínez-Banderas, A. Aires, F. J. Teran, J. E. Perez, J. F. Cadenas, N. Alsharif, T. Ravasi, A. L. Cortajarena, and J. Kosel, Functionalized magnetic nanowires for chemical and magneto-mechanical induction of cancer cell death, Scientific Reports 2016 6:1 **6**, 1 (2016).

[136] W. Hu, M. Zhang, R. J. Wilson, A. L. Koh, J. S. Wi, M. Tang, R. Sinclair, and S. X. Wang, Fabrication of planar, layered nanoparticles using tri-layer resist templates, Nanotechnology **22**, 10.1088/0957-4484/22/18/185302 (2011).

[137] P. Tiberto, G. Barrera, F. Celegato, G. Conta, M. Coïsson, F. Vinai, and F. Albertini, Ni80Fe20 nanodisks by nanosphere lithography for biomedical applications, Journal of Applied Physics **117**, 10.1063/1.4913278 (2015).

[138] M. Goiriena-Goikoetxea, A. García-Arribas, M. Rouco, A. V. Svalov, and J. M. Barandiaran, High-yield fabrication of 60 nm Permalloy nanodiscs in well-defined magnetic vortex state for biomedical applications, Nanotechnology **27**, 0 (2016).

[139] M. A. Verschuuren, M. Megens, Y. Ni, H. van Sprang, and A. Polman, Large area nanoimprint by substrate conformal imprint lithography (SCIL), Advanced Optical Technologies **6**, 243 (2017).

[140] J. Di, X. Gao, Y. Du, H. Zhang, J. Gao, and A. Zheng, Size, shape, charge and "stealthy" surface: Carrier properties affect the drug circulation time in vivo, Asian journal of pharmaceutical sciences **16**, 444 (2021).

[141] S. Adhikari, J. Li, Y. Wang, L. Ruijs, J. Liu, B. Koopmans, M. Orrit, and R. Lavrijsen, Optical Monitoring of the Magnetization Switching of Single Synthetic-Antiferromagnetic Nanoplatelets with Perpendicular Magnetic Anisotropy, ACS Photonics **10**, 1512 (2023).

[142] J. Pommier, P. Meyer, G. Pénissard, J. Ferré, P. Bruno, and D. Renard, Magnetization reversal in ultrathin ferromagnetic films with perpendicular anistropy: Domain observations, Physical Review Letters **65**, 2054 (1990).

[143] M. Baumgartner, K. Garello, J. Mendil, C. O. Avci, E. Grimaldi, C. Murer, J. Feng, M. Gabureac, C. Stamm, Y. Acremann, S. Finizio, S. Wintz, J. Raabe, and P. Gambardella, Spatially and time-resolved magnetization dynamics driven by spin-orbit torques, Nature Nanotechnology **12**, 980 (2017).

[144] M. Buchner, K. Höfler, B. Henne, V. Ney, and A. Ney, Tutorial: Basic principles, limits of detection, and pitfalls of highly sensitive SQUID magnetometry for nanomagnetism and spintronics, Journal of Applied Physics **124**, 10.1063/1.5045299 (2018).

[145] O. Kazakova, R. Puttock, C. Barton, H. Corte-León, M. Jaafar, V. Neu, and A. Asenjo, Frontiers of magnetic force microscopy, Journal of Applied Physics **125**, 10.1063/1.5050712 (2019).

[146] A. Balan, P. M. Derlet, A. F. Rodríguez, J. Bansmann, R. Yanes, U. Nowak, A. Kleibert, and F. Nolting, Direct observation of magnetic metastability in individual iron nanoparticles, Physical Review Letters **112**, 10.1103/PhysRevLett.112.107201 (2014).

[147] B. Han, X. Gao, J. Lv, and Z. Tang, Magnetic Circular Dichroism in Nanomaterials: New Opportunity in Understanding and Modulation of Excitonic and Plasmonic Resonances, Advanced Materials **32**, 10.1002/adma.201801491 (2020).

[148] W. Wernsdorfer, K. Hasselbach, D. Mailly, B. Barbara, A. Benoit, L. Thomas, and G. Suran, Magnetization of single magnetic particles, Journal of Magnetism and Magnetic Materials **140-144**, 389 (1995).

[149] C. Thirion, W. Wernsdorfer, and D. Mailly, Switching of magnetization by nonlinear resonance studied in single nanoparticles (2003).

[150] S. Adhikari, Y. Wang, P. Spaeth, F. Scalerandi, W. Albrecht, J. Liu, and M. Orrit, Magnetization Switching of Single Magnetite Nanoparticles Monitored Optically, arXiv preprint **arXiv:2207** (2022), arXiv:2207.07866 .

[151] P. Spaeth, S. Adhikari, L. Le, T. Jollans, S. Pud, W. Albrecht, T. Bauer, M. Caldarola, L. Kuipers, and M. Orrit, Circular Dichroism Measurement of Single Metal Nanoparticles Using Photothermal Imaging, Nano Letters **19**, 8934 (2019).

[152] F. Ece Demirer, R. Lavrijsen, and B. Koopmans, An investigation of the interface and bulk contributions to the magneto-optic activity in Co/Pt multi-layered thin films, Journal of Applied Physics **129**, 163904 (2021).

[153] D. B. Gopman, D. Bedau, S. Mangin, C. H. Lambert, E. E. Fullerton, J. A. Katine, and A. D. Kent, Asymmetric switching behavior in perpendicularly magnetized spin-valve nanopillars due to the polarizer dipole field, Applied Physics Letters **100**, 062404 (2012).

[154] D. T. Quach, T. D. Chu, T. S. Nguyen, T. T. P. Doan, X. T. Nguyen, K. M. Lee, J. R. Jeong, N. Kim, H. J. Shin, and D. H. Kim, Microscopic origin of asymmetric magnetization reversal of Co/Pt multilayers with perpendicular magnetic anisotropy, Current Applied Physics **20**, 1026 (2020).

[155] M. Lavanant, P. Vallobra, S. Petit Watelot, V. Lomakin, A. D. Kent, J. Sun, and S. Mangin, Asymmetric Magnetization Switching in Perpendicular Mag-

netic Tunnel Junctions: Role of the Synthetic Antiferromagnet's Fringe Field, Physical Review Applied **11**, 34058 (2019).

[156] M. Forrester and F. Kusmartsev, The nano-mechanics and magnetic properties of high moment synthetic antiferromagnetic particles, Physica Status Solidi (A) Applications and Materials Science **211**, 884 (2014).

[157] T. G. Kang, M. A. Hulsen, P. D. Anderson, J. M. Den Toonder, and H. E. Meijer, Chaotic mixing induced by a magnetic chain in a rotating magnetic field, Physical Review E - Statistical, Nonlinear, and Soft Matter Physics **76**, 10.1103/PhysRevE.76.066303 (2007).

[158] C. Liu, T. Stakenborg, S. Peeters, and L. Lagae, Cell manipulation with magnetic particles toward microfluidic cytometry, Journal of Applied Physics **105**, 102014 (2009).

[159] J. Jamet, S. Lemerle, P. Meyer, J. Ferré, B. Bartenlian, N. Bardou, C. Chappert, and P. Veillet, Dynamics of the magnetization reversal in Au/Co/Au micrometer-size dot arrays, Physical Review B - Condensed Matter and Materials Physics **57**, 14320 (1998).

[160] R. Dittrich, G. Hu, T. Schrefl, T. Thomson, D. Suess, B. D. Terris, and J. Fidler, Angular dependence of the switching field in patterned magnetic elements, in *Journal of Applied Physics*, Vol. 97 (American Institute of PhysicsAIP, 2005) p. 10J705.

[161] T. Thomson, G. Hu, and B. D. Terris, Intrinsic distribution of magnetic anisotropy in thin films probed by patterned nanostructures, Physical Review Letters **96**, 10.1103/PhysRevLett.96.257204 (2006).

[162] J. M. Shaw, W. H. Rippard, S. E. Russek, T. Reith, and C. M. Falco, Origins of switching field distributions in perpendicular magnetic nanodot arrays, Journal of Applied Physics **101**, 10.1063/1.2431399 (2007).

[163] B. Pfau, C. M. Günther, E. Guehrs, T. Hauet, H. Yang, L. Vinh, X. Xu, D. Yaney, R. Rick, S. Eisebitt, and O. Hellwig, Origin of magnetic switching field distribution in bit patterned media based on pre-patterned substrates, Applied Physics Letters **99**, 62502 (2011).

[164] R. Lavrijsen, A. Feránndez-Pacheco, D. Petit, R. Mansell, J. H. Lee, and R. P. Cowburn, Tuning the interlayer exchange coupling between single perpendicularly magnetized CoFeB layers, Applied Physics Letters **100**, 052411 (2012).

[165] M. S. Pierce, J. E. Davies, J. J. Turner, K. Chesnel, E. E. Fullerton, J. Nam, R. Hailstone, S. D. Kevan, J. B. Kortright, K. Liu, L. B. Sorensen, B. R. York, and O. Hellwig, Influence of structural disorder on magnetic domain formation in perpendicular anisotropy thin films, Physical Review B - Condensed Matter and Materials Physics **87**, 184428 (2013), 1301.1737 .

[166] J. A. Thornton, Influence of Apparatus Geometry and Deposition Conditions on the Structure and Topography of Thick Sputtered Coatings., J Vac Sci Technol **11**, 666 (1974).

[167] C. M. Günther, F. Radu, A. Menzel, S. Eisebitt, W. F. Schlotter, R. Rick, J. Lüning, and O. Hellwig, Steplike versus continuous domain propagation in Co/Pd multilayer films, Applied Physics Letters **93**, 72505 (2008).

[168] C. T. Rettner, S. Anders, J. E. Baglin, T. Thomson, and B. D. Terris, Characterization of the magnetic modification of Co/Pt multilayer films by He+, Ar+, and Ga+ ion irradiation, Applied Physics Letters **80**, 279 (2002).

[169] T. Hauet, O. Hellwig, S. H. Park, C. Beigń, E. Dobisz, B. D. Terris, and D. Ravelosona, Influence of ion irradiation on switching field and switching field distribution in arrays of Co/Pd-based bit pattern media, Applied Physics Letters **98**, 10.1063/1.3581896 (2011).

[170] D. Stanescu, D. Ravelosona, V. Mathet, C. Chappert, Y. Samson, C. Beigń, N. Vernier, J. Ferŕ, J. Gierak, E. Bouhris, and E. E. Fullerton, Tailoring magnetism in CoNi films with perpendicular anisotropy by ion irradiation, Journal of Applied Physics **103**, 10.1063/1.2838228 (2008).

[171] A. Berger, Y. Xu, B. Lengsfield, Y. Ikeda, and E. E. Fullerton, ΔH(M, ΔM) method for the determination of intrinsic switching field distributions in perpendicular media, IEEE Transactions on Magnetics **41**, 3178 (2005).

[172] Y. Kitade, H. Komoriya, and T. Maruyama, Patterned media fabricated by lithography and argon-ion milling, IEEE Transactions on Magnetics **40**, 2516 (2004).

[173] J. M. Shaw, H. T. Nembach, T. J. Silva, S. E. Russek, R. Geiss, C. Jones, N. Clark, T. Leo, and D. J. Smith, Effect of microstructure on magnetic properties and anisotropy distributions in Co/Pd thin films and nanostructures, Physical Review B - Condensed Matter and Materials Physics **80**, 10.1103/PhysRevB.80.184419 (2009).

[174] J. W. Lau, R. D. McMichael, S. H. Chung, J. O. Rantschler, V. Parekh, and D. Litvinov, Microstructural origin of switching field distribution in patterned CoPd multilayer nanodots, Applied Physics Letters **92**, 12506 (2008).

[175] H. Tanaka, S. Takayama, M. Hasegawa, T. Fukunaga, U. Mizutani, A. Fujita, and K. Fukamichi, Electronic structure and magnetism of amorphous Co1-xBx alloys, Physical Review B **47**, 2671 (1993).

[176] P. V. Paluskar, R. Lavrijsen, M. Sicot, J. T. Kohlhepp, H. J. Swagten, and B. Koopmans, Correlation between magnetism and spin-dependent transport in CoFeB alloys, Physical Review Letters **102**, 10.1103/PhysRevLett.102.016602 (2009), arXiv:0812.0679 .

[177] J. S. Kim, G. Kim, J. Jung, K. Jung, J. Cho, W. Y. Kim, and C. Y. You, Control of crystallization and magnetic properties of CoFeB by boron concentration, Scientific Reports **12**, 1 (2022).

[178] R. Lavrijsen, G. Malinowski, J. H. Franken, J. T. Kohlhepp, H. J. Swagten, B. Koopmans, M. Czapkiewicz, and T. Stobiecki, Reduced domain wall pinning in ultrathin Pt/Co100−xBx/Pt with perpendicular magnetic anisotropy, Applied Physics Letters **96**, 022501 (2010).

[179] I. Tagawa and Y. Nakamura, Relationship between high density recording performance and particle coercivity distribution, IEEE Transactions on Magnetics **27**, 4975 (1991).

[180] C. Eyrich, A. Zamani, W. Huttema, M. Arora, D. Harrison, F. Rashidi, D. Broun, B. Heinrich, O. Mryasov, M. Ahlberg, O. Karis, P. E. Jönsson, M. From, X. Zhu, and E. Girt, Effects of substitution on the exchange stiffness and magnetization of Co films, Physical Review B - Condensed Matter and Materials Physics **90**, 235408 (2014).

[181] C. Moreau-Luchaire, C. Moutafis, N. Reyren, J. Sampaio, C. A. Vaz, N. Van Horne, K. Bouzehouane, K. Garcia, C. Deranlot, P. Warnicke, P. Wohlhüter, J. M. George, M. Weigand, J. Raabe, V. Cros, and A. Fert, Additive interfacial chiral interaction in multilayers for stabilization of small individual skyrmions at room temperature, Nature Nanotechnology 2016 11:5 **11**, 444 (2016).

[182] C. B. Eyrich, *Exchange stiffness in thin-film cobalt alloys*, Ph.D. thesis (2012).

[183] G. Malinowski, K. C. Kuiper, R. Lavrijsen, H. J. Swagten, and B. Koopmans, Magnetization dynamics and Gilbert damping in ultrathin Co48 Fe32 B20 films with out-of-plane anisotropy, Applied Physics Letters **94**, 102501 (2009).

[184] N. Pamme, Magnetism and microfluidics, Lab on a Chip **6**, 24 (2006).

[185] T. M. Squires and S. R. Quake, Microfluidics: Fluid physics at the nanoliter scale, Reviews of Modern Physics **77**, 977 (2005).

[186] M. A. Gijs, Magnetic bead handling on-chip: new opportunities for analytical applications, Microfluidics and nanofluidics **1**, 22 (2004).

[187] S. L. Biswal and A. P. Gast, Rotational dynamics of semiflexible paramagnetic particle chains, Physical Review E - Statistical Physics, Plasmas, Fluids, and Related Interdisciplinary Topics **69**, 9 (2004).

[188] E. Climent, M. R. Maxey, and G. E. Karniadakis, Dynamics of Self-Assembled Chaining in Magnetorheological Fluids, Langmuir **20**, 507 (2004).

[189] X. Fan and A. Walther, 1d colloidal chains: recent progress from formation to emergent properties and applications, Chemical Society Reviews **51**, 4023 (2022).

[190] S. Melle, G. G. Fuller, and M. A. Rubio, Structure and dynamics of magnetorheological fluids in rotating magnetic fields, Physical Review E - Statistical Physics, Plasmas, Fluids, and Related Interdisciplinary Topics **61**, 4111 (2000).

[191] J. H. Cheng, C. R. Li, and C. Y. Chen, Motion synchronicity of a micromagnetic-particle chain in a rotating field, AIP Advances **12**, 035222 (2022).

[192] S. Melle, O. G. Calderón, M. A. Rubio, and G. G. Fuller, Rotational dynamics in dipolar colloidal suspensions: Video microscopy experiments and simulations results, Journal of Non-Newtonian Fluid Mechanics **102**, 135 (2002).

[193] S. Melle, O. G. Calderón, G. G. Fuller, and M. A. Rubio, Polarizable particle aggregation under rotating magnetic fields using scattering dichroism, Journal of Colloid and Interface Science **247**, 200 (2002).

[194] S. Melle, O. G. Calderón, M. A. Rubio, and G. G. Fuller, Microstructure evolution in magnetorheological suspensions governed by Mason number, Physical Review E - Statistical Physics, Plasmas, Fluids, and Related Interdisciplinary Topics **68**, 10.1103/PhysRevE.68.041503 (2003).

[195] R. Calhoun, A. Yadav, P. Phelan, A. Vuppu, A. Garcia, and M. Hayes, Paramagnetic particles and mixing in micro-scale flows, Lab on a Chip **6**, 247 (2006).

[196] D. Leith, Drag on nonspherical objects, Aerosol Science and Technology **6**, 153 (1987).

[197] L. Leyssens, B. Vinck, C. Van Der Straeten, F. Wuyts, and L. Maes, Cobalt toxicity in humans—a review of the potential sources and systemic health effects (2017).

[198] R. G. Nuzzo, B. R. Zegarski, and L. H. DuBois, *Journal of the American Chemical Society*, Tech. Rep. 3 (1987).

[199] S. Leulmi, X. Chauchet, M. Morcrette, G. Ortiz, H. Joisten, P. Sabon, T. Livache, Y. Hou, M. Carrière, S. Lequien, and B. Dieny, Triggering the apopto-

sis of targeted human renal cancer cells by the vibration of anisotropic magnetic particles attached to the cell membrane, Nanoscale **7**, 15904 (2015).

[200] W. H. Meiklejohn and C. P. Bean, New magnetic anisotropy (1956).

[201] M. L. Lalieu, R. Lavrijsen, and B. Koopmans, Integrating all-optical switching with spintronics, Nature communications **10**, 110 (2019).

[202] H. Joisten, T. Courcier, P. Balint, P. Sabon, J. Faure-Vincent, S. Auffret, and B. Dieny, Self-polarization phenomenon and control of dispersion of synthetic antiferromagnetic nanoparticles for biological applications, Applied Physics Letters **97**, 253112 (2010).

[203] A. Moyano, E. Serrano-Pertierra, M. Salvador, J. C. Martínez-García, M. Rivas, and M. C. Blanco-López, Magnetic lateral flow immunoassays (2020).

[204] M. Salvador, J. C. Martínez-García, M. P. Fernández-García, M. C. Blanco-López, and M. Rivas, Biological and Medical Applications of Magnetic Nanoparticles, Magnetic Measurement Techniques for Materials Characterization , 771 (2021).

[205] X. Meng, H. Zhang, J. Song, X. Fan, L. Sun, and H. Xie, Broad modulus range nanomechanical mapping by magnetic-drive soft probes, Nature communications **8**, 1944 (2017).

[206] B. Gross, D. P. Weber, D. Rüffer, A. Buchter, F. Heimbach, A. Fontcuberta I Morral, D. Grundler, and M. Poggio, Dynamic cantilever magnetometry of individual CoFeB nanotubes, Physical Review B **93**, 10.1103/PhysRevB.93.064409 (2016), 1512.00621 .

[207] L. Ruijs, Towards mechanical torque characterization of synthetic antiferromagnetic nanoplatelets with perpendicular magnetic anisotropy, Master thesis (2022).

[208] M. Scheepers, A. Romijn, L. Van Ijzendoorn, and M. Prins, Rate of dimer formation in stable colloidal solutions quantified using an attractive interparticle force, Langmuir **35**, 10533 (2019).

[209] W. Poon, Y.-N. Zhang, B. Ouyang, B. R. Kingston, J. L. Wu, S. Wilhelm, and W. C. Chan, Elimination pathways of nanoparticles, ACS nano **13**, 5785 (2019).

[210] V. Y. Prinz, V. Seleznev, A. Gutakovsky, A. Chehovskiy, V. Preobrazhenskii, M. Putyato, and T. Gavrilova, Free-standing and overgrown ingaas/gaas nanotubes, nanohelices and their arrays, Physica E: Low-dimensional Systems and Nanostructures **6**, 828 (2000).

[211] Q. D. Inc., *Application Note 1500-015*.

[212] B. E. Saleh and M. C. Teich, *Fundamentals of photonics* (john Wiley & sons, 2019).

[213] E. D. Palik, *Handbook of optical constants of solids*, Vol. 3 (Academic press, 1998).